Report Title: Optimization of the Cathode Long-Term Stability in Molten

Carbonate Fuel Cells: Experimental Study and Mathematical Modeling

Type of Report: Final Report

Reporting Period Start Date: October 1, 1999

Reporting Period End Date: September 30, 2002

Principal Author(s): Hector Colonmer, Prabhu Ganesan, Nalini Subramanian, Dr.

Bala Haran, Dr. Ralph E. White and Dr. Branko N. Popov

Date Report was Issued: September, 2002

Name and Address of Submitting Organization:

Dr. Ralph E. White, Project Manager
Department of Chemical Engineering
University of South Carolina
Columbia, South Carolina 29208

DISCLAIMER

ABSTRACT

This project focused on addressing the two main problems associated with state of art Molten Carbonate Fuel Cells, namely loss of cathode active material and stainless steel current collector deterioration due to corrosion. We followed a dual approach where in the first case we developed novel materials to replace the cathode and current collector currently used in molten carbonate fuel cells. In the second case we improved the performance of conventional cathode and current collectors through surface modification. States of art NiO cathode in MCFC undergo dissolution in the cathode melt thereby limiting the lifetime of the cell. To prevent this we deposited cobalt using an electroless deposition process. We also coated perovskite ($La_{0.8}Sr_{0.2}CoO_3$) in NiO thorough a sol-gel process. The electrochemical oxidation behavior of Co and perovskites coated electrodes is similar to that of the bare NiO cathode. Co and perovskite coatings on the surface decrease the dissolution of Ni into the melt and thereby stabilize the cathode. Both, cobalt and provskites coated nickel oxide, show a higher polarization compared to that of nickel oxide, which could be due to the reduced surface area. Cobalt substituted lithium nickel oxide ($LiNi_{0.8}Co_{0.2}O_2$) and lithium cobalt oxide were also studied. $LiNi_xCo_{1-x}O_2$ was synthesized by solid-state reaction procedure using lithium nitrate, nickel hydroxide and cobalt oxalate precursor. $LiNi_xCo_{1-x}O_2$ showed smaller dissolution of nickel than state of art nickel oxide cathode. The performance was comparable to that of nickel oxide.

The corrosion of the current collector in the cathode side was also studied. The corrosion characteristics of both SS304 and SS304 coated with Co-Ni alloy were studied. This study confirms that surface modification of SS304 leads to the formation of complex scales with better barrier properties and better electronic conductivity at $650^{o}C$.

A three phase homogeneous model was developed to simulate the performance of the molten carbonate fuel cell cathode and the complete fuel cell. The homogeneous model is based on volume averaging of different variables in the three phases over a small volume element. This approach can be used to model porous electrodes as it represents the real system much better than the conventional agglomerate model. Using the homogeneous model the polarization characteristics of the MCFC cathode and fuel cell were studied under different operating conditions. Both the cathode and the full cell model give good fits to the experimental data.

TABLE OF CONTENTS

LIST OF GRAPHICAL MATERIALS

6

overpotential.

LIST OF TABLES

INTRODUCTION

The Molten Carbonate Fuel cell (MCFC), operating at a temperature of 650°C, has been under intensive development for the last few decades as a second-generation fuel cell [1,2]. Significant advances have been done in addressing design issues resulting in the development of prototype MCFC power generators. However, several hurdles remain before commercialization of molten carbonate fuel cells can be realized. The primary challenge remains in the proper selection of materials for the cathode and current collector. Current state-of-art [3] relies on NiO cathodes fabricated from Ni powder. However, during cell operation, nickel oxide dissolves in the electrolyte [4] and does not satisfy long-term stability criteria [5]. Nickel oxide reacts with CO_2 present in the electrolyte according to an acidic dissolution mechanism,

$$NiO + CO_2 \rightarrow Ni^{2+} + CO_3^{2-}$$
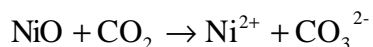
The dissolved nickel remains in equilibrium with the NiO cathode. Simultaneously, the Ni^{2+} cation diffuses to the anode side of the electrolyte and is then reduced in the hydrogen atmosphere to metallic nickel. The diffusion of Ni^{2+} cation fuels more dissolution of nickel from the cathode. Continued deposition of Ni in the anode region eventually leads to a short circuit between the anode and cathode. The dissolution is accelerated under higher CO_2 partial pressure and results in lowering the operating life of the cell. Apart from this, cathode dissolution results in loss of active material and in decrease of the active surface area available for the oxygen reduction reaction (cathodic reaction) leading to degradation in fuel cell performance.

Current state-of-art on solving the Ni dissolution problem is focused on varying the molten salt constituents [6,7] or using alternate cathode materials [8-10]. More basic molten carbonate melts such as Li/Na carbonate eutectic have been used to decrease the Ni dissolution rate in the melt [6,7]. Alkaline earth metal salts based on Ba or Sr have also been used as additives to increase the basicity of the melt. However, using more basic molten carbonate melts only partially solves the problem, since these melts decrease the NiO dissolution rate by 10 to 15% only [6,7].

The other approach to counter the nickel dissolution problem is to either modify NiO or to identify alternate cathode materials, which have longer life in the melt. Alternate electrodes should have good electronic conductivity, chemical stability and proper microstructure for use as MCFC cathodes. $LiFeO_2$ and $LiCoO_2$ offered initial promise as replacement material for NiO

cathodes [8-10]. However, the exchange current density for oxygen reduction reaction on $LiFeO_2$ is about two orders of magnitude lower than that on NiO. Thus, the slow kinetics for oxygen reduction limits the possibilities for further improvement of cathodes based on this material. $LiCoO_2$ is more stable than NiO in alkaline environment [8]. However, $LiCoO_2$ is less electronically conductive than NiO and is more expensive than NiO. Other choices for cathode materials have failed because of their low electronic conductivity or poor oxygen reduction kinetics. This being the case, surface modification of NiO with more resistant materials and doping $LiNiO_2$ with different amounts of cobalt using a solid state route are being considered as more viable alternatives. The objective of this part of the study is to evaluate the performance of cobalt coated nickel cathodes, cobalt coated nickel powder cathodes, $La_{0.8}Sr_{0.2}CoO_3$ coated nickel cathode and $LiNi_kCo_{1-x}O_2$ as cathode materials in molten carbonate fuel cells. A variety of electrochemical and physical characterization techniques have been used to study the performance of these mixed oxides.

As mentioned before, current collector corrosion is one of the primary challenges preventing the commercialization of MCFC. Austenitic stainless steels like 310S, 316 or 316L are typically used for construction of cathode and anode current collectors and bipolar separator plates [11-15]. The steel components are subjected to a large polarization when they are used in the cathode side owing to the potential in which oxygen reduction reaction occurs. This polarization leads to the oxidation of stainless steel components and to the dissolution of some of the alloy components through the porous corrosion scales.

The corrosion behavior of stainless steel components in molten carbonate conditions has been studied extensively during the past decade. Attempts were made to increase the corrosion resistance of these components by altering the alloy composition [11,12,16-19] or by using surface modification techniques [20,21].

The corrosion resistance of stainless steels and nickel-base alloys in aqueous solutions can often be increased by addition of chromium or aluminum [22-24]. Chromium protects the base metal from corrosion by forming an oxide layer at the surface. Chromium is also considered to be an important alloying metal for steels in MCFC applications. Chromium containing stainless steel however, leads to the induced loss of electrolyte. Previous studies done to characterize the corrosion behavior of chromium in MCFC conditions have shown formation of several lithium chromium oxides by reaction with the electrolyte [22]. This corrosion process

also results in increased ohmic loss due to formation of scales on the steel. Also, aluminum addition has a positive effect on corrosion resistance [23,24]. However, corrosion scales formed on aluminum containing alloys show low conductivity leading to a significant ohmic polarization loss.

Surface modification of the current collectors by suitable coatings, (electroless plating, electro cladding etc.) is an alternate approach for solving the corrosion problem. Surface modification or alloying alters the composition and complexity of the corrosion scales, which prevents further corrosion and outward diffusion of the alloy components. The coating materials that are currently studied fall into three categories namely (i) metals and alloys, (ii) ceramics composed of non-metals and (iii) ceramics composed of metals and non-metals including mixed oxides. Most of the current research on corrosion protective coatings is focused on metals and alloys because of the conductivity demand. Nickel electro cladding is popularly used as a surface modification technique to reduce corrosion on the anode side of the bipolar plate. However, the corrosion performance of most of the metals is not satisfactory on the cathode side. Ceramic coatings have good corrosion resistance properties, but they have a covalent character with a poor electronic conductivity. Mixed oxides are stable in molten carbonate (e.g. Li doped NiO, $LiCoO_2$, $LiFeO_2$ etc.). This is evident from the fact that these oxides are corrosion products in molten carbonates. Therefore, oxide materials can be used as coating to impart barrier properties and corrosion resistance in molten carbonate environment.

Nickel containing scales exhibit higher conductivity due to the presence of trivalent nickel ions, which introduce vacancies in the lattice of the scale [25]. Therefore nickel based coating can lead to superior conductivity and good protection provided that it is alloyed properly with corrosion resistant elements. Cobalt has a lower solubility in molten carbonate [26]. Electroless plating of Ni-Co gives rise to deposition of uniform layers of amorphous nanostructured material, which would result in better protection of the substrate. The objective of this work is therefore to synthesize electroless Co-Ni over SS 304 substrate and to characterize the deposit in MCFC cathode conditions. We expect to form a layer of lithiated Co-Ni oxides, which would improve the corrosion resistance and also increase the electronic conductivity. The corrosion characteristics of both SS304 and Co-Ni-SS304 were studied using a variety of electrochemical and surface characterization techniques. Flame atomic absorption spectroscopy was used to analyze the dissolved metal concentrations in molten carbonate.

Several theoretical models have been derived for the molten carbonate fuel cathode [27-37]. First principles based theoretical models for MCFC cathode can be divided into the thin film model [27] and the agglomerate model [28]. Wilemski [27] assumed that the MCFC cathode could be described as a cylindrical pore covered with a thin film of electrolyte. Gases flowing through the pore dissolve at the surface of the film and diffuse to the surface of the pore and react there. While the model gives good agreement with experimental data, it requires knowledge of the pore diameter, length and film thickness. Further, the entire description of the electrode is limited and cannot be used for cathode design analysis or two-dimensional simulations. The more common and popular approach for describing the MCFC cathode is the agglomerate model proposed by Yuh and Selman [28]. In this approach, the electrode is assumed to consist of cylindrical agglomerates completely flooded with electrolyte. Gaseous species move through straight cylindrical channels of macropores. Figure 1 presents a schematic of the agglomerate model as applied to the MCFC cathode. As shown in the figure, the macropore is continuous and extends from the current collector to the aluminate matrix. Adjacent to these macropores are microporous agglomerates covered with a film of electrolyte. Both the macropores and micropores remain segregated and the electrochemical reaction proceeds both on the film (exterior to the agglomerate) and also in the micropores (interior of the agglomerate). Yu and Selman [28] do not consider the varying degree of electrolyte fill in the cathode. Using this model, the polarization characteristics of both the cathode and anode have been analyzed. Further, this approach has also been applied to determine the reaction kinetic parameters through impedance analysis. The performance of the MCFC cathode has been analyzed extensively using the agglomerate model by Prins-Jansen *et al* [29]. Kunz *et al.* [30] used the agglomerate approach but assumed that the reaction proceeded only on the interior surface of the agglomerate but not on the surface of the film. Further, they incorporated the varying electrolyte fill in the cathode by correlating the porosimetry data to the agglomerate diameter. Fontes *et al.* [31] modified Selman's agglomerate model [28] to account for the electrolyte fill and compared these results to that of Kunz *et al.* [30]. They accounted for increase in the amount of electrolyte by the uniform growth of the electrolyte film or the decrease of the effective surface area for reaction. They found that a partially drowned agglomerate model with consideration of reaction on the exterior agglomerate surface provided a more realistic description of the cathode as compared to

the homogeneous agglomerate model. Christensen and Livbjerg [32] who considered the agglomerate as a one-dimensional slab instead of a cylinder also used a similar approach.

The principal deficiency of the agglomerate model, apart from the simplified pore structure assumed, is the lack of measured values for film thickness and agglomerate radius. Both these parameters cannot be estimated appropriately. The agglomerate radius can be estimated from post-test SEM micrographs. However, this radius is not the same along the whole length of the electrode. Further, as discussed by Prins Jansen *et al.* [29] attempts to estimate the thickness of the film vary by two orders of magnitude. Also, using the agglomerate model it is not possible to determine potential/current variations in directions perpendicular to the depth of the electrode. A pseudo-2D model was used by Fontes *et al.* [33] to determine the effect of different design parameters on the performance of the MCFC cathode. In this approach the local reaction rate was solved separately using the agglomerate approach. This was input as a source function in solving for the potential/current variations in two dimensions. This approach does not convey the true physical picture and is still limited due to the de-coupling of the potential from the reaction rate and the use of the agglomerate radius.

The above problems associated with the agglomerate model can be avoided if we take the alternate approach, namely the volume averaging technique used for porous media as done by Prins-Jansen *et al* [34] and De Vidts [38,39]. As compared to the agglomerate model where macropores and micropores remain as separate entities, in this approach the pores in the electrode exist in a single continuum. Further, all three phases co-exist within the porous electrode and reaction proceeds everywhere at the solid/melt interface. Using the volume averaging technique, Prins-Jansen *et al* [34] developed an impedance model for extracting the reaction and transport parameters from experimental data. Model simulations were fitted to experimental data within a certain confidence interval. They found that the diffusion coefficient of O_2 and CO_2 is three orders of magnitude larger than that estimated from the agglomerate model. Other parameters were of the same magnitude as reported by Yuh and Selman [28]. The model developed by Prins-Jansen *et al.* [34] combines both the electrolyte and gas phases into a single entity during volume averaging. The gas and liquid phase mass transport were not considered separately. In this study we adopt the volume averaging technique as outlined by De Vidts and White [38] for three phase reactions in porous electrodes. Using this approach, volume averaged concentrations of both gaseous and liquid phase reactants are obtained separately. The

goal of this study was to use the volume averaging technique for studying the polarization characteristics of the MCFC cathode, which has not been done before. The effect of different design parameters on the electrode performance has also been analyzed. The model considers the potential and current variation in both liquid and solid phases. Further concentration variations in the liquid and gaseous phases are considered separately. Using this approach electrolyte filling can be incorporated at ease in addition to eliminating the problems associated with the agglomerate concept. Also different reaction mechanisms can be studied and homogeneity can be assumed safely. Researchers interested in improving MCFC performance need to focus on cell components that have scope for yielding the maximum decrease in cell polarization. A full cell model would prove useful in analyzing the performance of MCFC in detail and in determining voltage losses in different regions of the cell. Previous modeling work in MCFC was focused on studying the performance of individual electrodes under different gas compositions and temperature. Yuh and Selman [28] modeled the performance of the MCFC cathode and anode and determined the dependencies of the electrode kinetic parameters on inlet gas composition. Other approaches to MCFC modeling have followed a similar methodology to date and no extensive full cell modeling has been done. Machielse [40] used a simple algebraic model to describe the performance of molten carbonate fuel cell. The model does not consider any changes in reactant concentrations across the MCFC electrodes. A similar approach was used by Standaert *et al.* [41] to analyze the performance of the MCFC. They used two different forms of the Nernst equation to determine the cell potential. The first approximation considered the local current density to be constant (zero order approximation). The second took into account the nonhomogeneity of the current density by assuming the local current density as a linear function of the distance (first order approximation). Both these approximations are valid only under limited cell operating conditions. A comprehensive full cell model is necessary in explaining the fuel cell performance. The objective of this last study is to understand the molten carbonate fuel cell performance through theoretical modeling. To accomplish this we first derive model equations using a three phase homogeneous model based on volume averaging. Next, the model equations are solved through finite element analysis and the polarization drops in different regions in the cell are determined. Finally, we analyze the cell performance and study the effect of different electrode variables on cell polarization. The maximum power that can be obtained is also determined for different cell thickness.

EXECUTIVE SUMMARY

This project focused on addressing the two main problems associated with state of art Molten Carbonate Fuel Cells, namely loss of cathode active material and stainless steel current collector deterioration due to corrosion. We followed a dual approach where in the first case we developed novel materials to replace the cathode and current collector currently used in molten carbonate fuel cells. In the second case we improved the performance of conventional cathode and current collectors through surface modification. States of art NiO cathode in MCFC undergo dissolution in the cathode melt thereby limiting the lifetime of the cell. To prevent this we deposited cobalt using an electroless deposition process. We also coated perovskite ($La_{0.8}Sr_{0.2}CoO_3$) in NiO thorough a sol-gel process. The electrochemical oxidation behavior of Co and perovskites coated electrodes is similar to that of the bare NiO cathode. Co and perovskite coatings on the surface decrease the dissolution of Ni into the melt and thereby stabilize the cathode. Both, cobalt and provskites coated nickel oxide, show a higher polarization compared to that of nickel oxide, which could be due to the reduced surface area. Cobalt substituted lithium nickel oxide ($LiNi_{0.8}Co_{0.2}O_2$) and lithium cobalt oxide were also studied. $LiNi_kCo_{1-x}O_2$ was synthesized by solid-state reaction procedure using lithium nitrate, nickel hydroxide and cobalt oxalate precursor. XRD analysis of sintered $LiNi_kCo_{1-x}O_2$ indicated that lithium evaporation occurs during heating. The lithium loss decreases with an increase of the cobalt content in the mixed oxides. The stability studies showed that dissolution of nickel into the molten carbonate melt is smaller in case of $LiNi_kCo_{1-x}O_2$ cathodes compared to the dissolution values reported in literature for state-of-the-art NiO. Pore volume analysis of the sintered electrode indicated a mean pore size of 3 μm and a porosity of 40%. EIS studies done on $LiNi_{0.8}Co_{0.2}O_2$ cathodes under different gas conditions indicated that the rate of the cathodic discharge reaction depends on the O_2 and the CO_2 partial pressures. The polarization performance was comparable to that of nickel oxide.

Apart from studies on improving the cathode performance, the corrosion of the current collector in the cathode side was also studied. The corrosion characteristics of both SS304 and SS304 coated with Co-Ni alloy were studied. Immersion tests performed on SS304 and Co-Ni encapsulated SS304 indicated more chromium dissolution in case of SS304 than for Co-Ni encapsulated SS304. SEM and EDAX analysis of the posttest SS304 indicated a loss of Cr from the surface. XRD patterns of the corrosion scales showed the presence of lithium ferrite along with $LiFe_5O_8$ in the case of SS304 and mixed lithium-cobalt-nickel-iron oxides in the case of Co-Ni encapsulated SS304. Conductivity of the corrosion scale was higher in the case of Co-Ni encapsulated SS304 when compared to SS304. This study confirms that surface modification of SS304 leads to the formation of complex scales with better barrier properties and better electronic conductivity at 650°C.

A three phase homogeneous model based on volume averaging was developed to simulate the performance of the molten carbonate fuel cell cathode and the complete fuel cell. The homogeneous model is based on volume averaging of different variables in the three phases over a small volume element. This approach can be used to model porous electrodes as it represents the real system much better than the conventional agglomerate model. Using the homogeneous model the polarization characteristics of the MCFC cathode and fuel cell were studied under different operating conditions. The effect of different parameters such as the exchange current density, electrolyte conductivity, cathode thickness, and the diffusion

coefficient on the performance of cathode was analyzed. The diffusion coefficients, electrolyte conductivity and the exchange current density are all affected by changes in temperature. All of them have an Arrhenius form of dependency on temperature. The activation energy and the frequency factor for each of these parameters have been estimated by fitting the model to experimental data of $LiNiCoO_2$ at different temperatures. Using these fitted parameters the performance of NiO and $LiCoO_2$ cathodes has been studied. Exchange current density for different materials was obtained by fitting the model to the experimental polarization data. Hence, apart from qualitative analysis of the cathode behavior, the model can be used to extract critical thermodynamic, kinetic and transport parameters from polarization data. The full cell model was used to analyze the contribution of each of the cell components to losses in cell potential. It was seen that ohmic losses in the cell dominated the cell polarization at low current densities. With increasing applied current, polarization losses in the cathode increased and became comparable to the ohmic losses in the separator. Finally, the power density of the cell was determined as a function of various parameters.

EXPERIMENTAL

The following section contains the description of the preparation of the cathodes materials, $LiNi_kCo_{1-x}O_2$ cathode and cobalt coated nickel cathode, and the current collector material, cobalt-nickel encapsulation of SS304. Following this preparation, a description of the electrochemical and characterization techniques used to study the samples is presented. The development of the model equations is also described here. A schematic of the MCFC cell based on the agglomerate model is given in Figure 1. The cell used for the experimental work and it's schematic are shown in Figure 2 and Figure 3 respectively.

Development of Surface Modified Electrodes

Cobalt coated nickel cathode

Tape casting: - Porous nickel cathode was made by a tape casting and sintering process. Nickel (Aldrich company) particles were ground and sieved to obtain uniform particles of size 3-5 μm. The tape casting slurry was prepared by ball milling nickel powder in water with suitable binder (PVA) and plasticizer (glycerol). The ball milling was done in two steps. At the first step, 50 g of nickel powder were added to 5 g of PVA (PVA liquid 15 wt.%) and 1 g of defoamer (Airdefoam™ 60, Air Products). The ingredients were mixed thoroughly with 15 g of water and the slurry was ball milled for 3 hr in order to break the weak agglomerates. Next, 9 g of glycerol was added to the above suspension and the resulting slurry was ball milled for an additional 3 hr. The slurry was then slightly warmed (50° C) and degassed using a ROTOVAP$^®$ evaporator. The slurry was cooled and then cast using a doctor blade assembly over a glass plate coated with silicone oil. The drying was performed slowly at room temperature for about 48 hours. The cast plate nickel tape is then stripped off gently from the glass plate and stored.

Sintering: - Sintering of the tape casted electrodes influences the cathode pore structure and thereby affects its electrochemical performance. TGA was done to determine the optimum heat treatment schedule for sintering. A typical TGA curve for green nickel tape is shown in Figure 4. The as cast Ni tape was pre-heated at 120°C for 12 hours in order to remove all the crystalline water in the tape. TGA analysis was done by heating the sample from 100°C to 650°C at a rate of 10°C/min. A steep reduction in weight (15 wt%) is seen on heating the sample to 200°C due to the removal of the binder. A secondary weight loss (5 wt%) is noticed between 300°C to

400°C due to the removal of plasticizer. The removal of all volatile and decomposable organic matter is completed below 400°C. On heating the sample above 400°C oxidation of nickel surface takes place. The total weight loss varies between 15 to 20wt.% depending upon the binder and plasticizer contents in the green tapes. Since, Ni is oxidized beyond 400° C, it is critical to heat the sample in a reducing atmosphere to prevent oxidation during sintering. Further, the rate of heating should be very slow initially to ensure complete burn out of binder and plasticizer. Based on the above TGA analysis, the following heating pattern was used - for sintering the electrodes: (i) green tapes which were cut out to specific area (10 cm x 10 cm) were initially heated from room temperature - to 130°C at a rate of 1°C/min in nitrogen atmosphere, (ii) in the second step the temperature was held at 130°C for 10 hours, (iii) next, the temperature was raised to 230°C at a rate of 1°C/min in nitrogen atmosphere, (iv) the temperature was held at 230°C for 2 hours, (v) next, the temperature was raised to 400°C at 1°C/min in nitrogen atmosphere, (vi) next the temperature was maintained at 400°C for 2 hours, (vii) next, the temperature was raised to 800°C at 1°C/min in hydrogen atmosphere, (viii) next, the temperature was held at 800°C for 1 hour and (ix) finally, the sample was cooled to room temperature using a cooling rate of 1°C/min in hydrogen atmosphere.

Cobalt Coating: - Cobalt encapsulation on nickel tapes was carried out with moderate stirring in 20 g/l cobalt sulfate, 20 g/l sodium hypophosphite, 50 g/l sodium citrate and 40 g/l ammonium chloride. In addition to these constituents, NH_4OH was added periodically during deposition to maintain the pH between 8.5 and 9.5. The pH frequently dropped below 9 during deposition indicating that cobalt deposition was proceeding. The deposition was stopped once the pH remained constant, indicating the absence of cobalt in the solution. The cobalt encapsulated nickel tape was rinsed with deionized water, dried at 65°C for 4 hours and later sintered at 800°C in air for 2 hours. This was done to remove all decomposable material, which could have been incorporated into the Ni laminate during Co deposition.

Cobalt coated nickel powder electrodes

Electrodes Preparation:- Nickel (Aldrich company) particles were ground and sieved to obtain uniform particles of size 3-5 μm. Then cobalt encapsulation on nickel particles was performed. The cobalt encapsulation process followed was the same described in the previous section. After

encapsulation, the same procedure of tape casting and sintering as in the previous section was performed.

Lanthanum strontium cobalt oxide coated nickel oxide electrode

$La_{0.8}Sr_{0.2}CoO_3$ Coating:- Nickel oxide electrodes were prepared following the tape casting and sintering procedure previously described. $La_{0.8}Sr_{0.2}CoO_3$ precursor gel was prepared as follows. Initially stoichiometric amounts of lanthanum acetate (5.488g), strontium acetate (0.8588g) and cobalt acetate (4.9814g) were dissolved in DI water with constant stirring. Then, citric acid (8.4056g), a complexing agent dissolved in DI water was added followed by the addition of ethylene glycol (2.4828g). The pH of the solution was maintained between 8 and 9. The solution was heated for 10 h at 80° C using a hot plate with constant stirring until it turned into a viscous gel. Nickel electrodes of desired size were cut and dipped in the gel and dried in air for 1 h and then dried in vacuum for 5 hours at 90 ^{o}C. The dipping was repeated several times to have a uniform coating. After drying, the electrodes were heat treated at different temperatures varying from 300° to 900° C.

Development of Novel Electrode Material

Cobalt doped Lithium Nickel Oxide

Material synthesis: - Cobalt doped lithium nickel oxides were prepared using solid-state synthesis procedure. Stoichiometric amounts of lithium nitrate ($LiNO_3$), nickel hydroxide ($Ni(OH)_2$) and cobalt oxalate ($CoC_2O_4.2H_2O$) obtained from Aldrich chemical company were used as the starting precursors for the solid-state synthesis. The compounds were mixed thoroughly and were heated in the presence of helium (regular grade, National Welders) first at 250°C for about 5 hours followed by heating at 630°C for 2 days. All the temperature ramps were maintained at 1°C/min. After the helium treatment, the samples were heated in oxygen atmosphere at 800°C for 20 hours. Following this, the samples were finally heated in an autoclave at 500 psi O_2 pressure at 700°C for 20 hours. Figure 5 shows the scanning electron micrographs of synthesized $LiNi_kCo_{1-x}O_2$. As shown in Fig. 5, a significant increase of $LiNi_kCo_{1-x}O_2$ particle size is observed with an increase of cobalt doping from x= 0.1 to x=0.2

Sintering: - A typical TGA curve for green $LiNi_xCo_{1-x}O_2$ tape is shown in Figure 6. The cast $LiNi_xCo_{1-x}O_2$ tape was pre-heated at 150°C for 12 hours in order to remove all the solvent in the tape. TGA analysis was done by heating the sample from 100°C to 650°C at a rate of 10°C/min. A steep reduction in weight (12 wt%) is seen on heating the sample between 200 and 400°C due to the removal of the binder and plasticizer. The removal of all volatile and decomposable organic matter is completed below 400°C. The total weight loss varies between 13 to 15wt.% depending upon the binder and plasticizer contents in the green tapes. Figure 7 shows the scanning electron micrographs of $LiNi_{0.8}Co_{0.2}O_2$ tapes sintered at 750°C, 800°C, 850°C and 900°C. Tapes sintered at 800°C showed better pore structure. Based on the above TGA and SEM analysis, the following heating pattern was used - for sintering the electrodes: (i) green tapes which were cut out to specific area (10 cm x 10 cm) were initially heated from room temperature to 150°C at a rate of 1°C/min in air, (ii) in the second step the temperature was held at 150°C for 10 hours, (iii) next, the temperature was raised to 400°C at a rate of 1°C/min in air, (iv) next, the temperature was held at 400°C for 3 hours, (v) next, the temperature was raised to 800°C at 1°C/min in air, (vi) next, the temperature was held at 800°C for 1 hour and (vii) finally, the sample was cooled to room temperature using a cooling rate of 1°C/min.

Current Collector

Nickel-Cobalt coating:- Electrodes of area 1 cm^2 were made from a perforated stainless steel 304 (Perforated Metals Inc.), with a void area of 45%. The electrodes were cleaned with alkali and washed in distilled water before the characterization studies in order to be free of any contaminants. Co-Ni encapsulation on SS304 electrodes was carried out using a procedure developed in our laboratories [26]. Cobalt and Nickel encapsulation was carried out with moderate stirring in a solution at 90°C containing 30 g/L cobalt chloride, 30 g/L nickel chloride, 100 g/L sodium citrate, and 50 g/L ammonium chloride. In addition to these constituents, NH_4OH and NaOH were added periodically during deposition to maintain the pH between 8.5 and 9.5. The pH frequently dropped below 9 during deposition indicating that cobalt and nickel deposition was proceeding. The deposition was stopped once the pH remained constant, indicating the absence of cobalt and nickel in the solution. The Co-Ni encapsulated SS304 was rinsed with deionized water, dried at 65°C for 4 hours.

Electrodes Characterization

Oxidation Studies:- In-situ oxidation of bare and surface modified SS 304 electrodes were studied using a three-electrode set-up. Square electrodes (1 cm x 1 cm) cut from bare and surface modified SS304 were spot welded with a gold wire and were used as working electrodes. Gold was used as a counter electrode while $Au/(2CO_2+1O_2)$ served as a reference electrode. The reference gas flow rate was maintained at 10 cc/min. Oxidant gas with a composition of 30% CO_2 and 70% air (National Welders) was directly purged into the $(Li_{0.62}K_{0.38})_2CO_3$ eutectic melt through an alumina tube. The open circuit potential studies were performed   using an EG&G PAR model 273A potentiostat interfaced with a computer. The oxidation behavior was also studied by using cyclic voltammetry method.

Pot cell studies: - In order to determine the solubility of the protective coatings and the new electrode materials in molten carbonate, pot tests were carried out under cathode gas conditions. Pellet electrodes of 2.5 cm diameter were cut out from sintered cathodes and current collector. They were weighed and carefully dropped inside an alumina crucible containing 100 g of molten carbonate $(Li_2CO_3/K_2CO_3=62/38)$ at 650°C. Cathode gas (30% CO_2/70% air) was bubbled through the carbonate melt using alumina tubes. About 0.2 g of molten carbonate was taken from the melt approximately every 6 hours upto 200 hours using an alumina rod. The molten carbonate sample was dissolved in 10% dilute acetic acid. Atomic absorption spectroscopy was used to analyze the concentration of dissolved nickel and cobalt.

Electrochemical and Material Characterization: - Half-cell performance studies were done in a 3-cm^2-lab cell shown in Figures 2 and 3. $LiNi_{0.8}Co_{0.2}O_2$, cobalt coated nickel electrode and cobalt-nickel coated SS304 were used both as the working and counter electrodes. $(Li_{0.62}K_{0.38})_2CO_3$ eutectic embedded in a $LiAlO_2$ matrix was used as the electrolyte. Polarization studies were done using an oxidant gas composition of 70% air and 30% CO_2. An oxygen reference electrode $(Au/CO_2/O_2)$ connected to the electrolyte tile with a salt bridge $(50\%(Li_{0.62}K_{0.38})_2CO_3 + 50\%LiAlO_2)$ were used to monitor the polarization of the cathode. Electrochemical impedance spectroscopic studies were performed using a Model 1255 Schlumberger Frequency Analyzer. The electrode was stable during the experiments and its open circuit potential changed less than 1 mV. The impedance data generally covered a frequency range of 1 mHz to 100kHz. A sinusoidal ac voltage signal varying by $\pm$ 5 mV was applied in all cases. X-ray diffraction (XRD) was used to study the crystal structure of the

samples. Mercury porosimeter was used to characterize the pore-volume distribution of the sintered cathodes. Scanning electron microscope (SEM) was used to study the microstructure of the electrodes from 3 cm^2 cells. Energy dispersive spectroscopy (EDAX) was employed to investigate the composition of the electrodes in the presence of cathode gas conditions.

Cathode Model
Development of Theoretical Model

In the molten carbonate fuel cell, oxygen and CO_2 combine at the cathode to form carbonate ions. At the anode hydrogen combines with the carbonate ions from the cathode to form CO_2 and water. The net reaction results in the formation of water with no harmful side reactions. The system of interest to us is the cathode where reduction of oxygen occurs. In order to overcome the difficulties associated with the agglomerate approach, we start by considering a cross-section of the porous electrode as shown in Fig. 8. No difference is made between the macropores and micropores while deriving the model equations. The primary reaction in the MCFC cathode is oxygen reduction, which is given by:

$$\tfrac{1}{2}O_2 + CO_2 + 2e^- \rightarrow CO_3^{2-} \tag{1}$$

The above reaction occurs at the interface between the NiO particle and the electrolyte. We neglect any changes in the concentration of the carbonate ions and assume that the concentration of the electrolyte does not change. Further, we assume that the system is at steady state and neglect any changes in cathode due to corrosion. Finally, we neglect changes in temperature in the cathode. Based on these assumptions we next derive the volume-averaged equations describing transport and reaction in the MCFC cathode.

Concepts and Definitions of Volume Averaging:

In this section, equations are derived for a porous electrode consisting of three phases: solid, liquid and gas. Following De Vidts [38,39] we consider a small elemental volume V. This volume should be small compared to the overall dimensions of the porous electrode. But it should be large enough to contain all three phases (see Figure 8). Also it should result in meaningful local average properties. This volume is so chosen that adding pores around this volume does not result in a change in the local average properties. We avoid the bimodal pore distribution where we consider macropores to be filled with the gas and micropores to be occupied by the electrolyte. Rather pores of all sizes are filled with both the electrolyte and the

gas, which is more realistic. Some basic definitions of volume averaging have to be presented before understanding the development of the model equations.

Superficial volume average $\overline{y}$ and the intrinsic volume average $\langle y \rangle$ are defined as

$$\overline{y}^{(i)} \equiv \frac{1}{V} \int_{V_{(i)}} y \, dV \tag{2}$$

$$\langle y \rangle^{(i)} \equiv \frac{1}{V_{(i)}} \int_{V_{(i)}} y \, dV \tag{3}$$

Here the superscript i represents the phase. The superficial and intrinsic volume averages are related by the porosity.

$$\overline{y}^{(i)} = e^{(i)} \langle y \rangle^{(i)} \tag{4}$$

Whenever volume averages of the gradients and the divergence appear they should be replaced by the gradients and divergence of the volume averages as below. These are referred to as the theorem of the local volume average of the gradient and the divergence [43,44].

$$\overline{\nabla y}^{(l)} = \nabla \overline{y}^{(l)} + \frac{1}{V} \int_{S_{lg}} y^{(l)} n_{(lg)} dS + \frac{1}{V} \int_{S_{ls}} y^{(l)} n_{(ls)} dS \tag{5}$$

$$\overline{\nabla \cdot y}^{(l)} = \nabla \cdot \overline{y}^{(l)} + \frac{1}{V} \int_{S_{lg}} y^{(l)} \cdot n_{(lg)} dS + \frac{1}{V} \int_{S_{ls}} y^{(l)} \cdot n_{(ls)} dS \tag{6}$$

Mass transport equations:

Mass transport occurs in the liquid and gas phases. Both oxygen and carbon dioxide gas are fed to the MCFC cathode through the current collector. Both O_2 and CO_2 diffuse through the macropores in the cathode and are transferred by diffusion in the melt to the surface of the NiO particles. The material balance in the liquid and gas phases for any species i is given by

$$\frac{\partial c_i^{(l)}}{\partial t} + \nabla \cdot N_i^{(l)} = 0 \qquad i = CO_2, O_2 \tag{7}$$

$$\frac{\partial c_i^{(g)}}{\partial t} + \nabla \cdot N_i^{(g)} = 0 \tag{8}$$

There are no bulk reactions. All reactions are assumed to take place at the electrolyte-electrode interface. This is denoted by the normal vector $n_{(ls)}$ in Fig. 8. Gas diffuses into the electrolyte at

the normal interface $n_{(gl)}$ and reacts at the interface of the electrolyte with the solid catalyst particles, $n_{(ls)}$. Hence the homogeneous reaction rate is neglected. Fick's law gives molar flux in the liquid and gas phases.

$$N_i^{(l)} = -D_i^{(l)} \nabla c_i^{(l)} + c_i^{(l)} v^{\diamond} \tag{9}$$

Binary diffusion is assumed in the gas phase. For a binary system $j_{(A)}$, defined as the mass flux relative to the mass average velocity, is given by [39]

$$j_{(A)} = -\frac{c^2}{r} M_{(A)} M_{(B)} D_{(AB)} \nabla x_{(A)} \tag{10}$$

where A refers to O_2 and B refers to CO_2.

The relation between $J_{(A)}^{\diamond}$ (molar flux relative to molar average velocity), $j_{(A)}^{\diamond}$ (mass flux relative to molar average velocity) and $j_{(A)}$ for a binary system is given by

$$J_{(A)}^{\diamond} = \frac{j_{(A)}^{\diamond}}{M_{(A)}} \tag{11}$$

$$j_{(A)}^{\diamond} = \frac{M}{M_{(B)}} j_{(A)} \tag{12}$$

The relation between $N_{(A)}$ (molar flux with respect to a fixed frame of reference) and $J_{(A)}^{\diamond}$

$$J_{(A)}^{\diamond} = N_{(A)} - c_{(A)} v^{\diamond} \tag{13}$$

When convection is neglected

$$N_{(A)} = J_{(A)}^{\diamond} \tag{14}$$

Hence

$$N_{(A)} = -c D_{(AB)} \nabla x_{(A)} \tag{15}$$

$$x_{(A)} = \frac{c_{(A)}}{c} \tag{16}$$

$$N_{(A)} = \frac{c_{(A)}}{c} D_{(AB)} \nabla c - D_{(AB)} \nabla c_{(A)} \tag{17}$$

In general for a binary gas the flux is given by,

$$N_i^{(g)} = -D_i^{(g)}\nabla c_i^{(g)} + D_i^{(g)}\left(\frac{c_i^{(g)}}{c^{(g)}}\right)\nabla c^g \tag{18}$$

Using the definitions of volume averaging we obtain the volume averaged flux in both phases as,

$$\overline{N}_i^{(l)} = -D_i^{(l)}\left(\boldsymbol{e}^{(l)}\right)^{b-1}\nabla\left(\boldsymbol{e}^{(l)}\left\langle c_i\right\rangle^{(l)}\right) \tag{19}$$

$$\overline{N}_i^{(g)} = -D_i^{(g)}\left(\boldsymbol{e}^{(g)}\right)^{b-1}\nabla\left(\boldsymbol{e}^{(g)}\left\langle c_i\right\rangle^{(g)}\right) + D_i^{(g)}\left(\boldsymbol{e}^{(g)}\right)^{b-1}\frac{\left\langle c_i\right\rangle^{(g)}}{\left\langle c\right\rangle^{(g)}}\nabla\left(\boldsymbol{e}^{(g)}\left\langle c\right\rangle^{(g)}\right) \tag{20}$$

Volume averaging Eqns. 7 and 8 and substituting the above definitions in Eqns. 19 and 20 gives the following volume averaged mass balance equations,

$$\frac{\partial \overline{c}_i^{(l)}}{\partial t} + \nabla\cdot\overline{N}_i^{(l)} + \overline{F}_i^{(\text{lg})} - \overline{R}_i^{ls} = 0 \tag{21}$$

$$\frac{\partial \overline{c}_i^{(g)}}{\partial t} + \nabla\cdot\overline{N}_i^{(g)} - \overline{F}_i^{(\text{lg})} - \overline{R}_i^{gs} = 0 \tag{22}$$

where $\overline{F}_i^{(\text{lg})}, \overline{R}_i^{ls}$ and $\overline{R}_i^{gs}$ are all terms derived from jump balance analysis which has been discussed in detail by De Vidts and White [38]. $\overline{F}_i^{(\text{lg})}$ is the flux of species i from the liquid to the gas phase, $\overline{R}_i^{ls}$ the rate of heterogeneous reaction at the liquid solid interface and $\overline{R}_i^{gs}$ at the gas solid interface.

$$\overline{F}_i^{(\text{lg})} = a^{(\text{lg})}r_i^{(\text{lg})} \tag{23}$$

$$r_i^{(\text{lg})} = k_i^{(\text{lg})}\left(\frac{\left\langle c_i\right\rangle^{(l)}}{K_{e,i}} - \left\langle c_i\right\rangle^{(g)}\right) \tag{24}$$

where for any species i, k_i is the mass transfer coefficient and $K_{e,i}$ is the distribution coefficient. Rate of production of species i at the solid liquid interface is expressed in terms of the local current density. Butler-Volmer kinetics is assumed for the reaction at the electrode electrolyte interface.

$$\overline{R}_i^{(ls)} = -\sum_k \frac{s_{ik} a^{(sl)}}{n_k F} < j_k >^{(sl)} \tag{25}$$

$$\langle j_k \rangle^{(sl)} = i_0 \left\{ \left[\left(\frac{\langle c_{CO_2} \rangle^{(l)}}{\langle c^*_{CO_2} \rangle^{(l)}} \right)^{p_1} \left(\frac{\langle c_{O_2} \rangle^{(l)}}{\langle c^*_{O_2} \rangle^{(l)}} \right)^{p_2} \exp\left(\frac{a_a F f}{RT} \right) - \left(\frac{\langle c_{CO_2} \rangle^{(l)}}{\langle c^*_{CO_2} \rangle^{(l)}} \right)^{q_1} \left(\frac{\langle c_{O_2} \rangle^{(l)}}{\langle c^*_{O_2} \rangle^{(l)}} \right)^{q_2} \exp\left(\frac{-a_c F f}{RT} \right) \right] \right\}$$

(26)

Here $< j_k >^{(sl)}$ [16] is the local current density at the solid liquid interface and i_0 and i_0^0 are the concentration dependent and concentration independent exchange current densities respectively [45]. The anodic and cathodic reaction orders p_1, p_2 and q_1, q_2 have values of –2, 0, -1, 1/2 respectively.

$$i_0 = i_0^0 \left(p^*_{CO_2} \right)^{r_1} \left(p^*_{O_2} \right)^{r_2}$$

(27)

where r_1 and r_2 have a value of –1.25 and 0.375 respectively for the peroxide mechanism. These values will be different for other mechanisms [29]. At the gas-solid interface there is no reaction. Hence,

$$\overline{R}_i^{(gs)} = 0$$

(28)

Charge transfer equations:

Since we neglect any changes in the concentration of CO_3^{2-}, the effect of migration need not be considered. Hence, Ohms' law is valid in both the solid and liquid phases.

$$i^{(l)} = -k \nabla f^{(l)}$$

(29)

$$i^{(s)} = -s \nabla f^{(s)}$$

(30)

Volume averaging the current in the solid and liquid phases results in the following equations.

$$\overline{i}^{(l)} = -k \left(e^{(l)} \right)^{d-1} \nabla \left(e^{(l)} \langle f \rangle^{(l)} \right)$$

(31)

$$\overline{i}^{(s)} = -s \left(e^{(s)} \right)^{d-1} \nabla \left(e^{(s)} \langle f \rangle^{(s)} \right)$$

(32)

The condition of electroneutrality applies everywhere within the electrode. This means that the net sum of the solution and solid phase currents should be constant.

$$\nabla \cdot (\overline{i}^{(l)} + \overline{i}^{(s)}) = 0$$

(33)

Further, any current leaving the solid phase has to enter the liquid phase through the electrochemical reaction. Applying a balance on the solution phase current gives,

$$\nabla \cdot \bar{i}^{(l)} = a^{(sl)} \langle j_k \rangle^{(sl)} \tag{34}$$

In the above equation the gradient in the solution phase current is proportional to the reaction rate at the solid-liquid interface. Substituting Eq. 34 into Eq. 33 we have,

$$\nabla \cdot \bar{i}^{(s)} = -a^{(sl)} \langle j_k \rangle^{(sl)} \tag{35}$$

Next, we define the overpotential as $\langle f \rangle = \langle f \rangle^{(s)} - \langle f \rangle^{(l)}$. Combining Eqns. 31 – 35 and using the definition for overpotential results in,

$$\frac{\partial^2 \langle f \rangle}{\partial x^2} = a^{(sl)} \langle j_k \rangle^{(sl)} \left(\frac{1}{s \left(e^{(s)} \right)^d} + \frac{1}{k \left(e^{(l)} \right)^d} \right) \tag{36}$$

Governing equations:

Combining the above set of equation, assuming steady state, and introducing the dimensionless variables we arrive at the following governing model equations.

$$\frac{\partial}{\partial x^*} \cdot \left[D_i^{(l)} \left(e^{(l)} \right)^{b-1} \frac{\partial}{\partial x^*} \left(e^{(l)} \right) u_i^{(l)} \right] - \frac{a^{(lg)} k_i^{(lg)} L^2}{K_{e,i}} \left(u_i^{(l)} - u_i^{(g)} \right) - \frac{s_{ik} a^{(sl)} L^2}{n_k F \langle c \rangle_i^{(l)*}} < j_k >^{(sl)} = 0$$

$$\tag{37}$$

$$D_i^{(g)} \frac{\partial}{\partial x^*} \cdot \left[\left(e^{(g)} \right)^{b-1} \frac{\partial}{\partial x^*} \left(e^{(g)} u_i^{(g)} \right) \right]$$

$$-D_i^{(g)} \frac{\partial}{\partial x^*} \cdot \left[\left(e^{(g)} \right)^{b-1} \frac{u_i^{(g)}}{\langle c \rangle_{CO_2}^{(g)*} u_{CO_2}^{(g)} + \langle c \rangle_{O_2}^{(g)*} u_{O_2}^{(g)}} \frac{\partial}{\partial x^*} \left(e^{(g)} \left(\langle c \rangle_{CO_2}^{(g)*} u_{CO_2}^{(g)} + \langle c \rangle_{O_2}^{(g)*} u_{O_2}^{(g)} \right) \right) \right]$$

$$+ L^2 a^{(lg)} k_i^{(lg)} \left(u_i^{(l)} - u_i^{(g)} \right) = 0$$

$$\tag{38}$$

$$\frac{\partial^2 F \langle f \rangle / RT}{\partial x^{*2}} = a^{(sl)} L^2 \langle j_k \rangle^{(sl)} \left(\frac{1}{s \left(e^{(s)} \right)^d} + \frac{1}{k \left(e^{(l)} \right)^d} \right) \frac{F}{RT} \tag{39}$$

The following dimensionless variables have been used in arriving at these equations.

$$u_i^{(l)} = \frac{\langle c \rangle_i^{(l)}}{\langle c \rangle_i^{(l)*}}, u_i^{(g)} = \frac{\langle c \rangle_i^{(g)}}{\langle c \rangle_i^{(g)*}}$$

Since we consider the transport of O_2 and CO_2 in the liquid and gas phases, we have five governing equations - four transport equations (Eq. 37 and 38) and one equation for the polarization (Eq. 39). We assume the problem is one-dimensional and neglect any changes in planes perpendicular to the x axis.

Boundary conditions:

Since, the gases are fed at the current collector side of the cathode, in the gas phase the concentrations are equal to the inlet concentration. In the solution phase, the concentrations are given by Henry's law. At the electrolyte tile (matrix) side the flux of all species is equal to zero. Also all the current is carried by the ions at the matrix end and by electrons at the current collector end. Based on these conditions the boundary condition at the current collector is given by,

$$\langle c_i \rangle^{(l)} = \langle c_i \rangle^{(l)*}, \langle c_i \rangle^{(g)} = \langle c_i \rangle^{(g)*}, \frac{\partial \langle f \rangle}{\partial x} = -\frac{I}{s \left(e^{(s)} \right)^d} \qquad \text{at} \quad x = 0 \qquad (40)$$

At the matrix (x=L),

$$\frac{\partial \langle c_i \rangle^{(l)}}{\partial x} = 0,$$

$$\left(e^{(g)} \right)^{b-1} \left(\frac{\partial}{\partial x} \left(e^{(g)} \langle c_i \rangle^{(g)} \right) + \left\langle \frac{c_i^{(g)}}{c^{(g)}} \right\rangle \frac{\partial}{\partial x} \left(e^{(g)} \langle c \rangle^{(g)} \right) \right) = 0, \qquad (41)$$

$$\frac{\partial \langle f \rangle}{\partial x} = \frac{I}{k \left(e^{(l)} \right)^d}$$

Expressing them in terms of the dimensionless variables

$$u_i^{(l)} = 1, u_i^{(g)} = 1, \frac{\partial F \langle f \rangle / RT}{\partial x^*} = -\frac{IL}{s \left(e^{(s)} \right)^d} \frac{F}{RT} \qquad \text{at} \quad x^* = 0 \qquad (42)$$

$$\frac{\partial u_i^{(l)}}{\partial x^*} = 0,$$

$$\left(e^{(g)}\right)^{b-1} \left(\begin{array}{l} \dfrac{\partial}{\partial x^*}\left(e^{(g)} u_i^{(g)}\right) + \\[1em] \left\langle \dfrac{u_i^{(g)}}{\langle c\rangle_{CO_2}^{(g)*} u_{CO_2}^{(g)} + \langle c\rangle_{O_2}^{(g)*} u_{O_2}^{(g)}} \right\rangle \dfrac{\partial}{\partial x^*}\left(e^{(g)}\left(\langle c\rangle_{CO_2}^{(g)*} u_{CO_2}^{(g)} + \langle c\rangle_{O_2}^{(g)*} u_{O_2}^{(g)}\right)\right) \end{array} \right) = 0,$$

$$\frac{\partial F\langle f\rangle / RT}{\partial x} = \frac{IL}{k\left(e^{(l)}\right)^d} \frac{F}{RT} \qquad \text{at} \quad x^* = 1$$

(43)

Based on these equations the following dimensionless groups can be written

$$d = a^{(sl)} L^2 i_0 \left(\frac{1}{s\left(e^{(s)}\right)^d} + \frac{1}{k\left(e^{(l)}\right)^d} \right) \frac{F}{RT} \tag{44}$$

$$g_1 = \frac{IL}{s\left(e^{(s)}\right)^d} \frac{F}{RT} \tag{45}$$

$$g_2 = \frac{IL}{k\left(e^{(l)}\right)^d} \frac{F}{RT} \tag{46}$$

List of Parameters

The parameters used in the model are given in Table I. Gas phase diffusion coefficients were estimated using the Fuller correlation [46]. It can also be estimated using the Chapman-Enskong equation. According to the Fuller correlation

$$D = \frac{10^{-3} T^{1.75} \left(1/M_{CO_2} + 1/M_{O_2}\right)^{1/2}}{p\left[\left(V_{CO_2}\right)^{1/3} + \left(V_{O_2}\right)^{1/3}\right]^2} \tag{47}$$

The diffusion volumes have been listed by Cussler [46] as $V_{CO_2} = 26.9$ and $V_{O_2} = 16.6$. At 923 K and 1 atm the binary diffusion coefficient has been estimated as 1.16 cm^2/s.

Electrochemical half-cells (3 cm^2) were assembled using two identical LiNiCoO$_2$ cathodes in an alumina housing. The electrodes were prepared by tape casting followed by sintering at around 900° C. The two electrodes were separated by a LiAlO$_2$ matrix impregnated with a eutectic mixture of 62:38 mol% Li$_2$CO$_3$ and K$_2$CO$_3$. Gold wire inserted in an alumina tube

31

served as a reference electrode in 33:66 O_2:CO_2 atmosphere. The working temperature of 650° C was reached in a programmed manner in about 50 hrs. Gas mixture comprising N_2, O_2 and CO_2 was passed at both working and the counter electrodes. The polarization is measured for different applied currents using the current interrupt technique and is corrected to get the IR-free polarization.

Full Cell Model
Development of Theoretical Model

A schematic of the molten carbonate fuel cell modeled is shown in Fig. 9. CO_2 and O_2 enter the cathode, where CO_2 is reduced to CO_3^{2-}. H_2 enters the anode (along with a little amount of CO_2 to improve wetting of the electrode by the electrolyte) where CO_3^{2-} is oxidized to give back CO_2. Our full cell model extends the volume averaging approach we had used for the MCFC cathode to the anode and matrix regions.

De Vidts [39] presents a detailed development of model equations for porous electrodes based on volume averaging, which has been adopted here. In this study we just present the governing equations along with the boundary conditions in each of the cathode, anode and the matrix and their interfaces. Since the potential and the concentration vary significantly along the thickness of the fuel cell a one dimensional model is assumed. Further, we do not consider corrosion of the cathode and current collectors and assume that the system is under steady state.

Equations at the current collector cathode interface (x = 0):

CO_2 and O_2 enter at the cathode side. The concentrations are equal to the inlet concentrations and the current is carried entirely by the electrons.

$$u_i^{(l)} = 1, u_i^{(g)} = 1, \boldsymbol{s}\left(\boldsymbol{e}_c^{(s)}\right)^d \frac{\partial \langle \boldsymbol{j} \rangle^{(s)}}{\partial x} = -\mathrm{I}, \boldsymbol{k}\left(\boldsymbol{e}_c^{(l)}\right)^d \frac{\partial \langle \boldsymbol{j} \rangle^{(l)}}{\partial x} = 0 \text{ where } \mathrm{i} = CO_2, O_2 \qquad (48)$$

Equations within the cathode region (from x = 0 to x = x$_1$):

$$\frac{\partial}{\partial x} \cdot \left[D_{i,c}^{(l)}\left(\boldsymbol{e}_c^{(l)}\right)^{b-1} \frac{\partial}{\partial x}\left(\boldsymbol{e}_c^{(l)}\right) u_{i,k}^{(l)} \right] - \frac{a^{(\mathrm{lg})} k_{i,c}^{(\mathrm{lg})}}{K_{e,i,c}}\left(u_i^{(l)} - u_i^{(g)}\right) - \frac{s_{ic} a^{(sl)}}{n_c F \langle c \rangle_{i,c}^{(l)*}} < j_c >^{(sl)} = 0$$

$$(49)$$

$$D_{i,k}^{(g)} \frac{\partial}{\partial x} \cdot \left[\left(e_c^{(g)} \right)^{b-1} \frac{\partial}{\partial x} \left(e_c^{(g)} u_{i,c}^{(g)} \right) \right]$$

$$-D_{i,k}^{(g)} \frac{\partial}{\partial x} \cdot \left[\left(e_c^{(g)} \right)^{b-1} \frac{u_i^{(g)}}{\langle c_{CO_2} \rangle^{(g)*} u_{CO_2}^{(g)} + \langle c_{O_2} \rangle^{(g)*} u_{O_2}^{(g)}} \frac{\partial}{\partial x^*} \left(e_c^{(g)} \left(\langle c_{CO_2} \rangle^{(g)*} u_{CO_2}^{(g)} + \langle c_{O_2} \rangle^{(g)*} u_{O_2}^{(g)} \right) \right) \right]$$

$$+ a^{(lg)} k_{i,c}^{(lg)} \left(u_{i,c}^{(l)} - u_{i,c}^{(g)} \right) = 0$$

(50)

The following dimensionless variables have been used in arriving at these equations.

$$u_{i,k}^{(l)} = \frac{\langle c \rangle_{i,k}^{(l)}}{\langle c \rangle_{i,k}^{(l)*}}, u_i^{(g)} = \frac{\langle c \rangle_{i,k}^{(g)}}{\langle c \rangle_{i,k}^{(g)*}}$$

where, $i = CO_2, O_2$ and $< j_c >^{(sl)}$ is the local current density at the solid liquid interface in the cathode given by the Butler Volmer expression.

$$\langle j_c \rangle^{(sl)} = (i_0)_c \left\{ \begin{array}{c} \left[\left(\frac{\langle c_{CO_2} \rangle^{(l)}}{\langle c_{CO_2}^* \rangle^{(l)}} \right)^{p_{1c}} \left(\frac{\langle c_{O_2} \rangle^{(l)}}{\langle c_{O_2}^* \rangle^{(l)}} \right)^{p_{2c}} \exp \left(\frac{a_{a,c} F \left(\langle f \rangle^{(s)} - \langle f \rangle^{(l)} - E_{eqc} \right)}{RT} \right) \right] \\ - \left(\frac{\langle c_{CO_2} \rangle^{(l)}}{\langle c_{CO_2}^* \rangle^{(l)}} \right)^{q_{1c}} \left(\frac{\langle c_{O_2} \rangle^{(l)}}{\langle c_{O_2}^* \rangle^{(l)}} \right)^{q_{2c}} \exp \left(\frac{-a_{c,c} F \left(\langle f \rangle^{(s)} - \langle f \rangle^{(l)} - E_{eqc} \right)}{RT} \right) \end{array} \right\}$$

(51)

$$(i_0)_c = i_{0,c}^0 \left(p_{CO_2}^* \right)^{r_{1,c}} \left(p_{O_2}^* \right)^{r_{2,c}}$$

(52)

$(i_0)_c$ and $i_{0,c}^0$ are the concentration dependent and concentration independent exchange current densities respectively. The anodic and cathodic reaction orders $p_{1,c}$, $p_{2,c}$ and $q_{1,c}$, $q_{2,c}$ have values of –2, 0, -1, 1/2 respectively. The reaction orders $r_{1,c}$ and $r_{2,c}$ have a value of –1.25 and 0.375 respectively for the peroxide mechanism [45]. These values will be different for other mechanisms. The charge balance gives the following equations for solid and liquid phase potentials.

$$\frac{\partial^2 \langle f \rangle^{(s)}}{\partial x^2} = \frac{a_c^{(sl)}}{s \left(e_c^{(s)} \right)^d} \langle j_c \rangle^{(sl)}$$

(53)

$$\frac{\partial^2 \langle f \rangle^{(l)}}{\partial x^2} = -\frac{a_c^{(sl)}}{k \left(e_c^{(s)} \right)^d} \langle j_c \rangle^{(sl)}$$

(54)

Equations at the cathode matrix interface (x=x₁):

In the matrix there are no species other than the electrolyte present due to the assumption of zero gas crossover. This is a valid assumption since the allowable gas leakage is below 2% to avoid cell failure. So the flux of all species is zero at the cathode-matrix interface. The liquid phase current is equal to the total current since the current is entirely carried by the ions.

$$\frac{\partial u_i^{(l)}}{\partial x} = 0,$$

$$\left(e_c^{(g)}\right)^{b-1} \left(\begin{array}{l} \frac{\partial}{\partial x}\left(e_c^{(g)} u_i^{(g)}\right) + \\ \left\langle \frac{u_i^{(g)}}{\langle c\rangle_{CO_2}^{(g)*} u_{CO_2}^{(g)} + \langle c\rangle_{O_2}^{(g)*} u_{O_2}^{(g)}} \right\rangle \frac{\partial}{\partial x}\left(e_c^{(g)}\left(\langle c\rangle_{CO_2}^{(g)*} u_{CO_2}^{(g)} + \langle c\rangle_{O_2}^{(g)*} u_{O_2}^{(g)}\right)\right) \end{array}\right) = 0,$$

$$k\left(e_c^{(l)}\right)^d \frac{\partial \langle j\rangle^{(l)}}{\partial x}\Big|_{x=x_1^-} = k\left(e^{(l)}\right)^d \frac{\partial \langle j\rangle^{(l)}}{\partial x}\Big|_{x=x_1^+}$$

(55)

where again $i = CO_2, O_2$.

Equations within the matrix (from x=x₁ to x=x₂):

There are no mass transport equations necessary in the matrix due to the assumption that there are is no crossover from one electrode to the other. There is no solid phase potential and the gradient in the liquid phase potential remains constant (i.e. the liquid phase current is equal to the total current). Hence

$$k\left(e_s^{(l)}\right)^{d_s} \frac{\partial^2 \langle f\rangle^{(l)}}{\partial x^2} = 0$$

(56)

The correction used for the conductivity, d_s is different from the correction d used in the electrodes, which will be explained later.

Equations at the matrix anode interface (x=x₂):

The flux of all species is zero at the matrix-anode interface due to the assumption of no gas crossover. The liquid phase current is equal to the total current similar to the cathode-matrix interface.

$$\frac{\partial u_i^{(l)}}{\partial x} = 0,$$

$$\left(e_a^{(g)}\right)^{b-1} \left(\begin{array}{c} \dfrac{\partial}{\partial x}\left(e_a^{(g)} u_i^{(g)}\right) + \\[2mm] \left\langle \dfrac{u_i^{(g)}}{\langle c\rangle_{CO_2}^{(g)*} u_{CO_2}^{(g)} + \langle c\rangle_{H_2}^{(g)*} u_{H_2}^{(g)}} \right\rangle \dfrac{\partial}{\partial x}\left(e_a^{(g)}\left(\langle c\rangle_{CO_2}^{(g)*} u_{CO_2}^{(g)} + \langle c\rangle_{H_2}^{(g)*} u_{H_2}^{(g)}\right)\right) \end{array} \right) = 0,$$

$$k\left(e^{(l)}\right)^d \frac{\partial \langle j\rangle}{\partial x}\Big|_{x=x_2^-} = k\left(e_a^{(l)}\right)^d \frac{\partial \langle j\rangle}{\partial x}\Big|_{x=x_2^+}$$

(57)

where $i = CO_2, H_2$

Equations within the anode (from $x = x_2$ to $x = L$):

$$\frac{\partial}{\partial x}\cdot\left[D_{i,a}^{(l)}\left(e_a^{(l)}\right)^{b-1}\frac{\partial}{\partial x}\left(e_a^{(l)}\right)u_{i,k}^{(l)}\right] - \frac{a^{(lg)}k_{i,a}^{(lg)}}{K_{e,i,a}}\left(u_i^{(l)} - u_i^{(g)}\right) - \frac{s_{i,a}a^{(sl)}}{n_a F\langle c\rangle_{i,a}^{(l)*}} < j_k >^{(sl)} = 0$$

(58)

$$D_{i,a}^{(g)}\frac{\partial}{\partial x}\cdot\left[\left(e_a^{(g)}\right)^{b-1}\frac{\partial}{\partial x}\left(e_a^{(g)} u_i^{(g)}\right)\right]$$

$$-D_{i,a}^{(g)}\frac{\partial}{\partial x}\cdot\left[\left(e_a^{(g)}\right)^{b-1}\frac{u_i^{(g)}}{\langle c_{CO_2}\rangle^{(g)*} u_{CO_2}^{(g)} + \langle c_{H_2}\rangle^{(g)*} u_{H_2}^{(g)}}\frac{\partial}{\partial x^*}\left(e_a^{(g)}\left(\langle c_{CO_2}\rangle^{(g)*} u_{CO_2}^{(g)} + \langle c_{H_2}\rangle^{(g)*} u_{H_2}^{(g)}\right)\right)\right]$$

$$+ a^{(lg)}k_{i,a}^{(lg)}\left(u_{i,a}^{(l)} - u_{i,a}^{(g)}\right) = 0$$

(59)

where $i = CO_2, H_2$ and $< j_a >^{(sl)}$ is the local current density at the solid liquid interface in the anode given by

$$\langle j_a\rangle^{(sl)} = (i_0)_a \left\{ \begin{array}{l} \left[\left(\dfrac{\langle c_{CO_2}\rangle^{(l)}}{\langle c_{CO_2}^*\rangle^{(l)}}\right)^{p_{1,a}}\left(\dfrac{\langle c_{H_2}\rangle^{(l)}}{\langle c_{H_2}^*\rangle^{(l)}}\right)^{p_{2,a}}\exp\left(\dfrac{a_{a,a}F\left(\langle f\rangle^{(s)} - \langle f\rangle^{(l)} - E_{eq,a}\right)}{RT}\right)\right] - \\[4mm] \left[\left(\dfrac{\langle c_{CO_2}\rangle^{(l)}}{\langle c_{CO_2}^*\rangle^{(l)}}\right)^{q_{1,a}}\left(\dfrac{\langle c_{H_2}\rangle^{(l)}}{\langle c_{H_2}^*\rangle^{(l)}}\right)^{q_{2,a}}\exp\left(\dfrac{-a_{c,a}F\left(\langle f\rangle^{(s)} - \langle f\rangle^{(l)} - E_{eq,a}\right)}{RT}\right)\right] \end{array} \right\}$$

(60)

$$(i_0)_a = i_{0,a}^0 \left(p_{CO_2}\right)^{r_{1,a}}\left(p_{H_2}\right)^{r_{2,a}}$$

(61)

In the anode the mechanism adopted by Lu and Selman is considered [47]. For this mechanism $p_{1,a}$, $p_{2,a}$ and $q_{1,a}$, $q_{2,a}$ have values of 0, 1/2, 1, -1/2 respectively. $r_{1,a}$ and $r_{2,a}$ have a value of 0.25 each. The governing equations for solid and liquid phase potentials are similar to the cathode.

$$\frac{\partial^2 \langle \boldsymbol{f} \rangle^{(s)}}{\partial x^2} = \frac{a_c^{(sl)}}{\boldsymbol{s}\left(\boldsymbol{e}_a^{(s)}\right)^d} \langle j_a \rangle^{(sl)} \tag{62}$$

$$\frac{\partial^2 \langle \boldsymbol{f} \rangle^{(l)}}{\partial x^2} = -\frac{a_c^{(sl)}}{\boldsymbol{k}\left(\boldsymbol{e}_a^{(s)}\right)^d} \langle j_a \rangle^{(sl)} \tag{63}$$

Equations at the anode current collector interface (x=L):

CO_2 and H_2 enter at the anode. The concentrations are equal to the inlet concentrations and the current is carried entirely by the electrons similar to the cathode-current collector interface

$$u_i^{(l)} = 1, u_i^{(g)} = 1, \boldsymbol{s}\left(\boldsymbol{e}_a^{(s)}\right)^d \frac{\partial \langle \boldsymbol{j} \rangle^{(s)}}{\partial x} = -\text{I}, \boldsymbol{k}\left(\boldsymbol{e}_a^{(l)}\right)^d \frac{\partial \langle \boldsymbol{j} \rangle^{(l)}}{\partial x} = 0 \tag{64}$$

where again i=CO_2, H_2

RESULTS AND DISCUSSION

Surface Modified Electrodes

Cobalt coated nickel cathode

Scanning Electron Micrograph: - Figure 10 shows the SEM images of Ni and cobalt encapsulated nickel electrodes prepared by the above sintering procedure. Cobalt microencapsulation leads to the formation of amorphous layers of cobalt over the entire microstructure of nickel tape. On heating the sample to 800°C, the volatile substances included during the cobalt microencapsulation process decomposed giving rise to a porous Co-Ni composite electrode. The primary particle size according to Figure 10 for nickel electrodes was in the range of 0.5 – 4 µm. Subsequent to Co encapsulation and sintering in air, the particles tend to agglomerate together. Detailed pore volume distribution analysis needs to be carried out to comment on the actual porosity and pore size distribution. The morphological difference between nickel and cobalt-encapsulated nickel can be attributed to the cobalt deposited over the nickel surface and the additional sintering done on the sample.

Vicker's hardness test: - The MCFC cathodes are typically nickel tapes prepared by either tape casting or loose powder sintering process followed by sintered in hydrogen atmosphere so as to keep it from oxidizing. The nickel tape is then *in-situ* oxidized in the molten carbonate under cathode gas conditions to form NiO. *In-situ* oxidizing is believed to be beneficial in terms of improved hardness and the pore structure of the substrate. Cobalt encapsulated cathodes were prepared using *ex-situ* oxidation and therefore have to be characterized for hardness. A Vickers hardness indenter (Figure 11) was used to indent the cobalt encapsulated and bare nickel tapes with a diamond tip. The physical deformation that happened during the indendation process was observed under a microscope and the dimensions of the depression was marked. Vickers harness number (*VHN*) [48] is calculated based on the observations made on the indent using the formula

$$VHN = \frac{2P}{d^2}\sin(\frac{a}{2})$$

where - d is the diagonal length left by the diamond shaped pyramid indenter. The angle between the phases of the pyramid is $\alpha=136°$. P is the load used in kilograms and the units of d are in millimeters. VHN was calculated for the Ni sintered under H_2 atmosphere (9.646 x 10^8 kg/mm^2) and cobalt coated nickel sintered in air cathodes (1.678 x 10^9 kg/mm^2). Cobalt coated nickel cathode shows a higher VHN value than for nickel cathode indicating that the Co coating improves the hardness of the Ni tapes.

Stability tests: - The short-term stability of cobalt encapsulated and bare nickel in molten carbonate eutectic were determined using pot tests. Atomic absorption (AA) was used to analyze the dissolved nickel and cobalt in the melt. Figure 12 shows the results of AA analysis on the amount of dissolved nickel and cobalt in the carbonate melt as a function of time. As shown in the plot, the rate of dissolution of Ni^{2+} was significantly higher in case of bare nickel when compared to that of cobalt microencapsulated nickel. Solubility of cobalt was about one order of magnitude smaller than that of nickel. The results indicate that cobalt is more resistive to the molten carbonate environment. The amount of nickel and cobalt cation in the carbonate melt increases with time and saturates after about 100 hours. Similar results have been obtained in the literature for the solubility of Ni^{2+} and Co^{2+} ions in the carbonate melt [49-53]. The results indicated that cobalt coating increases the barrier properties of the cathode and thereby decreases the dissolution of nickel in the melt.

Thermal oxidation behavior: - In order to study the performance of the sintered electrodes under cathode gas conditions, TGA was done on the sintered nickel and cobalt encapsulated nickel tapes. The temperature was increased from 100°C to 650°C at a rate of 10°C/min under cathode gas atmosphere (30% CO_2+70% air). The temperature was then maintained at 650°C for a period of two hours. Figure 13 shows the results of TGA analysis obtained for nickel tapes in the presence and absence of molten carbonate. The percentage increase in weight while heating the sample was plotted against the experiment time. The time interval between 0 and 55 minutes corresponds to a temperature rise from 100°C to 650°C at a heating rate of 10°C/min. The time interval after 55 min corresponds to the period where the temperature was maintained constant at 650°C. As shown in Fig. 13a, the weight of nickel sample in the absence of molten carbonate starts to increase after 40 min corresponding to a temperature of 400°C and stabilizes after about

2 hours at 650°C. On the other hand, the oxidation of nickel was rapid in case of nickel sample placed with molten carbonate salt in the presence of cathode gas. It appears that O_2 permeation and reaction with inner nickel particles is enhanced in the presence of molten carbonate. The weight increase in both the cases was about 27%, which suggests the complete conversion of Ni to NiO.

Oxidation of cobalt-coated nickel was very slow in the absence of molten carbonate and the oxidation continued even after two hours after reaching 650°C as shown in Figure 13b. Theoretical weight increase for the conversion of Ni and Co to their oxides (NiO/CoO) based on stochiometric calculation is around 27%. In the presence of molten carbonate, weight of the cobalt encapsulated substrate continued to increase due to oxidation and stabilized shortly after reaching 650°C. The percentage increase in weight was around 22 %. However, the actual weight increase is much lower in the absence of the carbonate melt (60 % lower than with the presence of molten carbonate). This slow oxidation of cobalt encapsulated nickel specimen is obviously due to the presence of cobalt, which is thermodynamically more stable.

Electrochemical oxidation behavior: - To understand the influence of cobalt encapsulation on nickel electrode from an electrochemical point of view, the open-circuit potentials of both samples were monitored as a function of time during the *in-situ* oxidation process. Cobalt coated sample which was sintered in air was used for this study. The oxidation was carried out in a three-electrode half-cell described in the experimental section. Oxidant gas composition of 67% CO_2 and 33% O_2 was bubbled at a constant rate of 60 cm^3/min through an alumina tube during the *in-situ* oxidation process. Figure 14 compares the OCP behavior of bare and cobalt encapsulated nickel electrodes as a function of immersion time.

In both cases, three different potential plateaus are observed which can be attributed to the following reactions [53,54]

$$Ni + CO_3^{2-} \rightarrow NiO + CO_2 + 2e^- \qquad \text{-0.80 V}$$

$$2Ni + 3CO_3^{2-} \rightarrow Ni_2CO_3 + 3CO_2 + 2e^- \qquad \text{-0.43 V}$$

$$Ni + CO_3^{2-} \rightarrow NiCO_3 + 2e^- \qquad \text{-0.25 V}$$
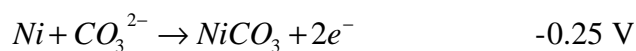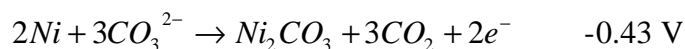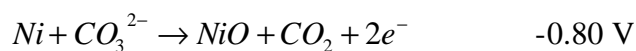
The first plateau in case of nickel oxidation is due to the formation of porous nickel oxide on the surface of the nickel matrix. Next, bulk nickel is oxidized to NiO at approximately –0.6 V.

The second plateau at –0.44 V has been attributed to the surface oxidation of Ni(II) oxide to trivalent nickel.

The redox processes that occur during the *in-situ* oxidation of cobalt correspond to: [54,55].

$$Co + CO_3^{2-} \rightarrow CoO + CO_2 + 2e^- \qquad \text{-0.85 V}$$

$$2Co + 4CO_3^{2-} \rightarrow Co_3O_4 + 4CO_2 + 8e^- \qquad \text{-0.68 V}$$

$$Co + CO_3^{2-} \rightarrow CoCO_3 + 2e^- \qquad \text{-0.35 V}$$
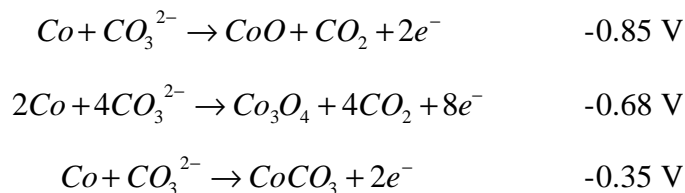
In the case of Co coated Ni, one can expect a solid solution of Co and Ni to be formed whose OCP is a mixed potential corresponding to oxidation of both Co and Ni.

Polarization studies: -Polarization studies were carried out in a three electrode 3 cm^2 lab scale cell containing nickel/cobalt encapsulated nickel electrodes both as the working and counter electrodes. Gold (oxygen reduction) served as a reference electrode. The electrodes were separated by a LiAlO$_2$ ceramic tile containing Li/K carbonate melt (62-38mol%). The cell is connected to a gold/oxygen reference electrode through a salt bridge. The polarization characteristics of NiO and Co-NiO cathodes were obtained by varying the current load. Figure 15 (a and b) compares the cathode polarization during the galvanodynamic scan for the two cathode materials as a function of different operating temperatures. The current was scanned at 1 mA/sec and the curves have been corrected for IR loss based on R$_\Omega$ calculated from impedance measurements (not shown).

The i-η characteristics (Fig. 15a and 15b) of both NiO and Co coated NiO are similar to each other indicating the charge transfer at lower overpotentials and in the case of Co coated NiO a complex mass transfer and charge transfer limited process at higher overpotentials. Increasing the temperature has larger influence on the polarization in case of NiO (Fig. 15a). The observed overpotentials η decrease with increasing the temperature indicating a decrease of both the polarization and diffusion overpotentials (for the case of the cobalt coated NiO) with an increase of temperature. Similar results were observed in literature [56,57].

As shown in Fig. 15 b similar results were also observed in case of Co encapsulated NiO. On increasing the temperature, there is a significant change in the overpotential characteristics of Co-NiO. The observed small decrease of the overpotential when compared

with the NiO overpotential probably results from a small decrease of surface area of the encapsulated active material. .

Reaction rate orders were obtained by performing a regression analysis of the exchange current density data obtained from i-V plots under low current load (i $\leq$ 10 mA/cm^2). Figure 16 shows the i-V plots obtained for the case of Co-NiO under different gas conditions. Similar studies were carried out at different temperatures and for NiO under similar conditions. The slope of the linear part of i-V curve was used to calculate the apparent exchange density based on the expression $i_o = \dfrac{RT}{nFR_{ct}}$ where, R is the universal gas constant, T is the cell temperature, F is the Faraday's constant and R_{ct} is the slope of the i-V response. Exchange current density was estimated as a function of gas composition for Co-NiO electrode from i-V plots obtained at low overpotentials. Figures 17a and 17b show a plot of exchange current density as a function of O_2 and CO_2 partial pressures, respectively. The slope of log(i_o) dependence with log(pO_2) is positive indicating a positive reaction order for O_2. While in the case of log(i_o) dependence vs. log(pCO_2), a negative slope is observed indicating a negative reaction order for CO_2. The range of values of exchange current density calculated for Co-NiO varied from 14.2 to 16.1 mA/cm^2. The apparent exchange current density calculated using the same method for the case of NiO varied between 29–31 mA/cm^2. The exchange current density data offers qualitative evidence for the observed difference in polarization performance in case of Co encapsulated and bare NiO because the i-V plots used to analyze the system may contain mass transfer limitations even at low current loads. Thus, exchange current density data offer only a qualitative evidence for the observed difference in polarization performance in case of Co encapsulated and bare NiO. The log plots shown in Figures 17a and 17b were not perfectly linear implying the presence of more than one reaction mechanism. For this reason, we have not attempted to identify the observed kinetics with any particular mechanism.

Electrochemical Impedance Spectroscopy (EIS) studies: - In order to understand further the kinetics of oxygen reduction on Co-NiO, impedance measurements were carried out at different gas compositions. EIS analysis was carried out at equilibrium potential (open circuit) on the NiO and Co-NiO electrodes. Figure 18 shows the impedance analysis of NiO electrode at different temperatures at a particular gas composition. The impedance response at any given temperature

is characterized by the presence of high frequency loop and an extension at low frequencies. The high frequency plot has been associated with the charge transfer processes while the low frequency loop to a slow process (mass transfer or slow homogeneous reactions). The impedance response shown in Fig. 18 is similar in appearance to the ones obtained by Yuh *et al*. [56,57] under similar conditions. As shown in Figure 18, the cell temperature has a marked effect on the ac impedance. Increasing the temperature, a drastic decrease is observed in Fig. 18 of charge transfer resistance, which in agreement with the results obtained from polarization studies.

Figures 19a and 19b show the impedance response of Co-NiO electrode as a function of different gas compositions at two different temperatures. The impedance responses appear differently in case of Co-NiO when compared to those of NiO. The two distinct loops occurring at high and low frequencies in the case of NiO appear to be merged with each other in case of Co-NiO. The effect of temperature clearly shows that the observed depressed semi circle loop includes both the charge transfer and mass transfer phenomenon. At higher temperature, the total impedance as acquired from the Nyquist plots decreases suggesting that the observed effect could well be assumed as a combination of mass transfer and charge transfer. From Figures 19a and 17b, it can also be seen that the effect of partial pressure of O_2 and CO_2 are antagonistic to each other. The magnitude of the impedance loop decreased on increasing the O_2 partial pressure. This clearly indicates a positive reaction order for oxygen and is similar to the response seen for NiO [57]. In case of CO_2, the impedance value increased with an increase in CO_2 partial pressures implying that the reaction order of CO_2 must be negative. Yuh *et al.* [57] obtained similar results for NiO in terms of O_2 and CO_2 dependence on impedance responses.

Post test characterization: - EDAX analysis was carried out to characterize the cobalt content in the cobalt encapsulated cathodes after 72 hours and 300 hours of polarization. EDAX patterns were identical in both cases. The concentration calculations based on the intensity peaks show that the cobalt and nickel concentration remain the same. The rate of dissolution was comparatively lower in case of Co-NiO when compared to that of NiO as shown in Figure 12. X-ray diffraction (XRD) studies were carried out on posttest Ni and Co-NiO cathode samples to identify the changes due to interaction in molten carbonate. Figure 20 shows the XRD pattern of nickel and cobalt coated nickel cathodes treated in molten carbonate under cathode gas conditions for a period of 300 hours. XRD pattern of Ni tape is characterized by peaks

corresponding to NiO, while that of Co-NiO shows a different pattern due to the presence of mixed oxides.

Cobalt coated nickel powder electrodes

Scanning Electron Micrograph: - Figure 21 shows the SEM images if cobalt encapsulated nickel powder electrodes prepared by the above sintering procedure. The primary particle size according to Figure 21 for nickel electrodes was in the range of 0.5 – 4 µm. Detailed pore volume distribution analysis needs to be carried out to comment on the actual porosity and pore size distribution. The morphological difference between nickel and cobalt-encapsulated nickel can be attributed to the cobalt deposited over the nickel surface.

Stability tests: - The short-term stability of cobalt encapsulated nickel powder and bare nickel in molten carbonate eutectic were determined using pot tests. Atomic absorption spectroscopy (AA) was used to analyze the dissolved nickel in the melt. Figure 22 shows the results of AA analysis on the amount of dissolved nickel in the carbonate melt as a function of time. As shown in the plot, the rate of dissolution of Ni^{2+} was significantly higher in case of bare nickel when compared to that of cobalt microencapsulated nickel powder. The amount of nickel in the carbonate melt increases with time and stays stable at 11 x 10^{-6} Ni mole fraction after about 100 hours. Similar results have been obtained in the literature for the solubility of Ni^{2+} and Co^{2+} ions in the carbonate melt [49-53]. The results indicated that 4 wt% cobalt coating increases the barrier properties of the cathode and thereby decreases the dissolution of nickel in the melt.

*Polarization studies: -*Polarization studies were carried out in a three electrode 3 cm^2 lab scale cell containing cobalt encapsulated nickel powder electrodes both as the working and counter electrodes. Gold (oxygen reduction) served as a reference electrode. The electrodes were separated by a LiAlO$_2$ ceramic tile containing Li/K carbonate melt (62-38mol%). The cell is connected to a gold/oxygen reference electrode through a salt bridge. The polarization characteristics Co-NiO cathode was obtained by varying the current load. Figure 23 compares the cathode polarization during the galvanodynamic scan for the cathode material at 650 ºC. The current was scanned at 1 mA/sec and the curves have been corrected for IR loss based on R$_\Omega$ calculated from impedance measurements (not shown). As can be observed from the plot, the

electrode polarization at 160 mA/cm^2 shows an overpotential of 90 mV, similar to the observed with cobalt coated nickel cathodes.

Electrochemical Impedance Spectroscopy (EIS) studies: - In order to understand further the kinetics of oxygen reduction on Co coated nickel powder, impedance measurements were carried out at different gas compositions. EIS analysis was carried out at equilibrium potential The impedance response at any given temperature is characterized by the presence of high frequency loop and an extension at low frequencies. The high frequency plot has been associated with the charge transfer processes while the low frequency loop to a slow process (mass transfer or slow homogeneous reactions). The impedance response shown in Fig. 24 is similar in appearance to the ones obtained by Yuh *et al*. [56,57] under similar conditions.

The magnitude of the impedance loop decreased on increasing the O_2 partial pressure. This clearly indicates a positive reaction order for oxygen and is similar to the response seen for NiO [57]. In case of CO_2, the impedance value increased with an increase in CO_2 partial pressures implying that the reaction order of CO_2 must be negative. Yuh *et al.* [57] obtained similar results for NiO in terms of O_2 and CO_2 dependence on impedance responses.

Lanthanum strontium cobalt oxide coated nickel oxide electrode

Scanning Electron Micrograph: - Figure 25 shows the SEM images of Ni and LSC coated nickel electrodes prepared by the above said procedure. The primary particle size according to Figure 25 for nickel electrodes was in the range of 1.00 – 6.80 µm. Subsequent to LSC coating and sintering in air, the particles tend to agglomerate together. The LSC coated NiO had a good pore structure. However, detailed pore volume distribution analysis needs to be carried out to comment on the actual porosity and pore size distribution. The morphological difference between nickel and LSC coated nickel can be attributed to the LSC coating on nickel surface followed by sintering. No change is observed in the surface morphology of LSC coated NiO and LSC-NiO after immersion in molten carbonate for 200 hours.

X-Ray diffraction analysis: Figures 26 and 27 show the XRD pattern obtained on the LSC coated samples. Figure 26 shows the XRD patterns of $La_{0.8}Sr_{0.2}CoO_3$ powders obtained from the gel after heat treatment in different temperatures ranging between 300 ^{o}C and 900 ^{o}C. It is clearly

seen that the compound formation starts only at 500 ^{o}C and crystalline product could be obtained at 900 ^{o}C. The $La_{0.8}Sr_{0.2}CoO_3$ formation onto the nickel electrodes was confirmed by matching the individual peaks. Figure 27 shows the XRD pattern of LSC coated NiO sintered at 900° C. Individual peaks correspond to $La_{0.8}Sr_{0.}2CoO_3$ and NiO are marked in the figure.

Stability tests: - The short-term stability of LSC-NiO and bare nickel in molten carbonate eutectic were determined using pot tests. Atomic absorption spectroscopy (AAS) was used to analyze the dissolved nickel and cobalt in the melt. From AAS we obtain the nickel ppm present in the solution of molten carbonate. Figure 28 shows the results of AA analysis on the amount of dissolved nickel and cobalt in the carbonate melt as a function of time. As shown in the plot, the solubility of Ni^{2+} from bare nickel was higher when compared to that of LSC-NiO. The results indicate that LSC coating increases the stability of conventional NiO cathode molten carbonate environment. The amount of nickel increases with time and saturates after about 100 hours. Similar results have been obtained in the literature for the solubility of Ni^{2+} ions in the carbonate melt [42,49-50]. Short-term stability test result shows that $La_{0.8}Sr_{0.2}CoO_3$ coating could prevent the nickel dissolution in the molten alkali carbonate melt.

Polarization studies: -Polarization studies were carried out in a three electrode 3 cm^2 lab scale cell containing nickel/cobalt encapsulated nickel electrodes both as the working and counter electrodes and with gold (oxygen reduction) reference electrode. The electrodes were separated by a $LiAlO_2$ ceramic tile containing Li/K carbonate melt (62-38). The cells are connected to a gold/oxygen reference electrode through a salt bridge. The working electrode potential is monitored with respect to the reference electrode. The polarization characteristics of NiO and LSC-NiO cathodes were obtained by varying the current load. Figures 29a and Figure 29b compare the cathode polarization during the galvanodynamic scan for the two cathode materials as a function of different operating temperatures. The current was scanned at 1 mA/sec and the curves have been corrected for IR loss based on R? calculated from impedance measurements (not shown).

Electrochemical Impedance Spectroscopy (EIS) studies: - In order to understand further the kinetics of oxygen reduction on LSC-NiO, impedance measurements were carried out at

different gas compositions. EIS analysis was carried out at equilibrium potential (open circuit) on the LSC-NiO electrodes. Figure 30 (a, b, c and d) shows the impedance response of LSC-NiO electrode as a function of different gas compositions at different temperatures. The impedance responses appear differently in case of LSC-NiO when compared to those of NiO. The two distinct loops occurring at high and low frequencies in the case of NiO appear to be merged with each other in case of LSC-NiO. The effect of temperature clearly shows that the observed depressed semi circle loop includes both the charge transfer and mass transfer phenomenon. At higher temperature, the total impedance as acquired from the Nyquist plots decreases suggesting that the observed effect could well be assumed as a combination of mass transfer and charge transfer. From Figures 30a and 30b, it can also be seen that the effect of partial pressure of O_2 and CO_2 are antagonistic to each other. The magnitude of the impedance loop decreased on increasing the O_2 partial pressure. This clearly indicates a positive reaction order for oxygen and is similar to the response seen for NiO [57]. In case of CO_2, the impedance value increased with an increase in CO_2 partial pressures implying that the reaction order of CO_2 must be negative. A mass transfer limitation phenomenon was observed when no CO_2 was passed to the working electrode. The same effect was observed by Yuh and Selman with 2 % CO_2 [68]. Yuh *et al.* [57] obtained similar results for NiO in terms of O_2 and CO_2 dependence on impedance responses.

New Electrode Material

Cobalt doped Lithium Nickel Oxide

X-ray diffraction studies: - Figure 31 shows a typical powder X-ray diffraction patterns of pristine $LiCoO_2$ and $LiNi_xCo_{1-x}O_2$ solid solutions. These patterns reveal that all these materials are single phase with the α-$NaFeO_2$ structure, space group R3*m*. The transition metal ions are in turn surrounded by six oxygen atoms. Infinite layers of $Ni_xCo_{1-x}O_2$ were formed through edge sharing of the $(Ni_xCo_{1-x}O_6)$ octahedras, with the intercalating lithium ions located between the layers. All of the diffraction lines of $LiNi_xCo_{1-x}O_2$ can be indexed with a hexagonal lattice. Analytical results were obtained from the XRD data using the lines (0, 0, 3) and (1, 0, 4). As the Ni^{3+} ions at the 3(a) sites of the $LiNiO_2$ lattice are partially replaced by Co^{3+} ions, the unit cell dimensions, a and c, in a hexagonal setting become smaller. The lattice constants were a =

2.876 $\overset{\circ}{A}$ and c = 14.183 $\overset{\circ}{A}$ for LiNi$_{0.9}$Co$_{0.1}$O$_2$; a = 2.871 $\overset{\circ}{A}$ and c = 14.176 $\overset{\circ}{A}$ for LiNi$_{0.8}$Co$_{0.2}$O$_2$; a = 2.865 $\overset{\circ}{A}$ and c = 14.170 $\overset{\circ}{A}$ for LiNi$_{0.7}$Co$_{0.3}$O$_2$ and a = 2.816 $\overset{\circ}{A}$ and c = 14.046 $\overset{\circ}{A}$ for LiCoO$_2$. This decrease in lattice constants is due to the difference in size between trivalent cobalt and trivalent nickel ions ($r_{Ni}^{3+} = 0.56 \overset{\circ}{A}$, $r_{Co}^{3+} = 0.53 \overset{\circ}{A}$) [58]. These results strongly suggest that LiNi$_x$Co$_{1-x}$O$_2$ is in a homogenous phase, i.e. Ni^{3+} and Co^{3+} are homogenously located at the octahedral 3(a) sites in a cubic phased oxygen array.

Figure 32 compares the XRD patterns of LiNi$_x$Co$_{1-x}$O$_2$ sintered at 800°C for a period of 24 h in the presence of air. The XRD patterns indicate that the (0, 0, 3) line characteristic of the lithium content decrease for the case of LiNi$_{0.9}$Co$_{0.1}$O$_2$. As the cobalt content increases in the LiNi$_x$Co$_{1-x}$O$_2$ (x = 0.2, 0.3, 1), the lithium evaporation on heating also decreases. Perez *et al.* [59] carried out a similar experiment wherein they treated different Li(NiCo) mixed oxides in molten carbonate at 650°C under air and observed a decrease in lithium content in the oxides. Figure 33 shows the XRD patterns of LiNi$_{0.8}$Co$_{0.2}$O$_2$ heat treated at different temperatures for a period of 24 h. It is seen that the LiNi$_{0.8}$Co$_{0.2}$O$_2$ is quite stable upto sintering temperatures of 800°C in terms of lithium content. Heating LiNi$_{0.8}$Co$_{0.2}$O$_2$ to 1100°C leads to significant lithium loss, which is seen, from the different XRD pattern obtained. Also, XRD pattern obtained from LiNi$_{0.8}$Co$_{0.2}$O$_2$ samples heat treated in molten carbonate for 500 hours under air at 650°C shows no significant structural change when compared to pristine oxide. This results show that LiNi$_x$Co$_{1-x}$O$_2$ (x = 0.2, 0.3) may exhibit the structural integrity needed of a MCFC cathode to sustain long-term operation.

Stability tests: - The short-term stability of LiNi$_x$Co$_{1-x}$O$_2$ (x = 0.1, 0.2, 0.3) in molten carbonate eutectic was determined using pot tests. Atomic absorption (AA) was used to analyze the dissolved nickel in the melt. Figure 34 shows the results of AA analysis on the amount of dissolved nickel in the carbonate melt as a function of time. The results indicate that cobalt doping increases the resistivity of the oxide to the molten carbonate environment. The amount of nickel cation in the carbonate melt increases with time and saturates after about 100 hours. The dissolution rate obtained for LiNi$_x$Co$_{1-x}$O$_2$ is about one half of the dissolution of state-of-the-art nickel oxide reported in literature [49-53]. Based on these results and the XRD data, it was decided to carry out further studies on LiNi$_{0.8}$Co$_{0.2}$O$_2$. These compounds exhibit enough stability

at operating temperatures and also the rate of dissolution of nickel is lower when compared to state-of-the-art cathodes.

Pore volume distribution: - The electrode structure is one of the principal factors determining cell performance in MCFCs. The electrode reaction takes place mainly near the meniscus (three phase boundary), where mass transport resistance is least for gas diffusing through the liquid to the reaction surface. Alternatively an electrolyte film may cover the pore wall through which the gas diffuses to the electrode. Flooding of the electrode is usually deleterious to the performance of cathodes. Cathode porosity is adjusted in order to ensure proper electrolyte distribution. Small pores retain electrolyte by capillary pressure, while large pores are gas-filled, even though their walls may be fully or partly wetted by thin liquid films. Figure 35 shows the pore volume distribution of sintered $LiNi_{0.8}Co_{0.2}O_2$ cathodes. The pore size distribution shows three kinds of pores ranging from micropores of less than 1 μm size to macropores of size greater than 10 μm. Majority of the pores lay in the intermediate class of particle size around 2~3 μm. The porosity of the sintered $LiNi_{0.8}Co_{0.2}O_2$ cathode was 38.5311%. This value is lower when compared to the porosity of *in-situ* sintered state-of-the-art NiO cathode (porosity~50-55%) [60]. This low porosity in case of $LiNi_{0.8}Co_{0.2}O_2$ cathode can cause higher polarization during testing of these electrodes. However, porosity can be enhanced by the addition of pore formers during tapecasting and by careful optimization of sintering conditions.

Polarization studies: -Polarization studies were carried out in a three electrode 3 cm^2 lab scale cell containing $LiNi_{0.8}Co_{0.2}O_2$ electrodes both as the working and counter electrodes Gold (oxygen reduction) served as a reference electrode. The electrodes were separated by a $LiAlO_2$ ceramic tile containing Li/K carbonate melt (62-38mol%). The cell is connected to a gold/oxygen reference electrode through a salt bridge. The polarization characteristics of $LiNi_{0.8}Co_{0.2}O_2$ cathodes were obtained by varying the current load. Figure 36 compares the cathode polarization during the galvanodynamic scan for the $LiNi_{0.8}Co_{0.2}O_2$ electrode at different operating temperatures. The current was scanned at 1 mA/sec and the curves have been corrected for IR loss based on R_Ω calculated from impedance measurements (not shown).

The i-η characteristics of $LiNi_{0.8}Co_{0.2}O_2$ cathodes obtained at different temperatures are similar to each other. Increasing the temperature has a significant influence on the polarization

48

in case of $LiNi_{0.8}Co_{0.2}O_2$. The observed overpotentials η decrease with increasing the temperature indicating a decrease of both the polarization and diffusion overpotentials with an increase of temperature. The voltage polarization decreased from 140 mV at 160 mA/cm^2 in case of 650°C to 65 mV/cm^2 at 750°C as shown in Fig 36. Similar results were observed in literature in case of NiO electrodes [42,56,57]. Our earlier study showed a voltage polarization of 55 mV for NiO and 95 mV for Co encapsulated nickel electrodes for an applied current of 160 mA/cm^2. Fig. 37 shows the effect of temperature on cathode polarization of NiO and Co encapsulated NiO. This difference in the performance of $LiNi_{0.8}Co_{0.2}O_2$ and NiO cathodes can be attributed to the poor porosity (~45%) of the $LiNi_{0.8}Co_{0.2}O_2$ cathodes.

The performance of the $LiNi_{0.8}Co_{0.2}O_2$ electrodes was evaluated from the exchange current density data obtained from i-V plots under low current load (i ≤ 10 mA/cm^2). The slope of the linear part of i-V curve was used to calculate the apparent exchange density based on the expression $i_o = \dfrac{RT}{nFR_{ct}}$ where, R is the universal gas constant, T is the cell temperature, F is the Faraday's constant and R_{ct} is the slope of the i-V response. The range of values of exchange current density calculated for $LiNi_{0.8}Co_{0.2}O_2$ cathodes varied from 25.1 to 26.1 mA/cm^2 during various stages of operation. The apparent exchange current density calculated using the same method for the case of NiO in one of our earlier studies varied between 29–31 mA/cm^2 [42]. The low exchange current density observed could again be due to the lower porosity in case of $LiNi_{0.8}Co_{0.2}O_2$ cathodes.

Electrochemical Impedance Spectroscopy (EIS) studies: - In order to understand the kinetics of oxygen reduction on $LiNi_{0.8}Co_{0.2}O_2$, impedance measurements were carried out at different gas compositions. EIS analysis was carried out at open circuit on the $LiNi_{0.8}Co_{0.2}O_2$ electrodes. Figure 38 shows the impedance analysis of NiO and $LiCoO_2$ electrodes at different temperatures at a particular gas composition. The impedance response at any given temperature is characterized by the presence of high frequency loop and an extension at low frequencies. The high frequency plot has been associated with the charge transfer processes while the low frequency loop to a slow process (mass transfer or slow homogeneous reactions). The impedance response shown in Fig. 39 (a, b, c, d, e and f) is similar in appearance to the ones obtained by Yuh *et al*. [56,57] under similar conditions for NiO cathodes. As shown in Figure 38, the cell

temperature has a marked effect on the ac impedance. Increasing the temperature, a drastic decrease of charge transfer resistance is seen, which in agreement with the results obtained from polarization studies.

From Figures 39 (a, b, c, d, e and f), it can also be seen that the effect of partial pressure of O_2 and CO_2 are in opposite to each other. The magnitude of the impedance loop decreased on increasing the O_2 partial pressure. This clearly indicates a positive reaction order for oxygen and is similar to the response seen for NiO [57]. In case of CO_2, the impedance value increased with an increase in CO_2 partial pressures implying that the reaction order of CO_2 must be negative. Yuh *et al.* [57] obtained similar results for NiO in terms of O_2 and CO_2 dependence on impedance responses. This shows that oxygen reduction kinetics in $LiNi_{0.8}Co_{0.2}O_2$ follows a similar mechanism as in that of NiO. Hence $LiNi_{0.8}Co_{0.2}O_2$ can be used as a cathode material for MCFC applications.

Current Collector Studies

Stability tests: - Stability of the coatings was determined by immersion tests and morphological and compositional analysis of the molten carbonate melt, SS samples, and the $LiAlO_2$ separators. Stainless steel forms complex corrosion products [20,25]. The composition of these corrosion products depends on the constituents and surface composition of the steel. Most of the corrosion products such as $LiCrO_2$ and NiO are not stable in the molten carbonate and dissolve in the melt. Therefore it was of interest to analyze the melt and to estimate the concentration of the dissolved current collector (SS304) constituent elements.

Atomic absorption spectroscopy: - The short-term stability of the corrosion products formed in case of SS304 and Co-Ni encapsulated SS304 in molten carbonate eutectic were determined using immersion tests. Atomic absorption spectroscopy (AAS) was used to analyze the dissolved chromium and nickel in the melt. Figure 40 shows the results of AAS analysis for the dissolved chromium and nickel in the carbonate melt as a function of time. The amount of material lost is given by the weight of Ni/Cr in the melt normalized to the surface area of the sample ($1cm^2$). As shown in Figure 40, the concentration of chromium in the melt was about three times higher in case of bare SS304 when compared to that of Co-Ni encapsulated SS304. Molar concentration of nickel was also significantly higher for the case of bare SS304 when compared to the surface

modified SS304. The amount of nickel and chromium in the carbonate melt increases with time and saturates to a stable value. The content stabilizes for both substrates after 100 hours of operation. The nickel content for SS304 stabilizes after 250 hours. In contrast, nickel from Co-Ni-SS304 stabilizes after 75 hours of operation. Coloring of the molten carbonate melt due to chromium dissolution was observed at the end of the experiment. The coloring was more intense in case of SS304 when compared to that of Ni-Co-encapsulated SS304.

SEM and EDAX analysis: - SEM and EDAX was used to study the morphology and compositional changes of bare and surface modified SS304 when exposed in molten carbonate melts at $650^{o}C$ for 500 hours under cathode gas conditions. Compositional and morphological analysis of fresh SS304 and Co-Ni encapsulated SS304 were also done for comparison.

Figure 41 shows scanning electron micrographs of fresh and posttest SS304 and Co-Ni encapsulated SS304 samples. Electroless deposition leads to formation of particles of Co-Ni on top of the SS304. In the case of post-test SS304, cubic crystals are uniformly distributed throughout the surface, while in the case of Co-Ni encapsulated SS304; the corrosion scale is more undefined and complex. EDAX analysis on the corrosion scale of SS304 showed high Fe content on the surface. According to literature SS304 forms a corrosion layer under cathode conditions consisting of $LiFe_5O_8$ [20].

EDAX analysis indicated that SS304 has a high initial Cr content (18 wt.%), which decreases with interaction in molten carbonate under cathode gas conditions. This is due to the dissolution of chromium into the electrolyte through oxidation and disintegration. EDAX analysis carried out on the corrosion scales of the surface modified SS304 indicates a high Co and Ni content in the scale. The cobalt and nickel contents did not change appreciably during the cell operation indicating a very stable coating. EDAX analysis on the separator matrix shows the presence of Cr. High concentration of Cr was found for the case of bare SS with a value of 6.5 wt.%. In the case of Co-Ni coated SS the amount of Cr is 0.24 wt.%. Figure 42 shows the digital pictures of the matrix after testing.

X-ray diffraction analysis were carried out on the corrosion scales formed on the stainless steel samples in order characterize the corrosion products that are formed during the interaction of steel with the molten carbonate under cathode gas conditions. Figure 43 shows the X-ray patterns obtained in case of post-test SS304 and Co-Ni encapsulated SS304. The diffraction

pattern differed significantly in case of SS304 and Co-Ni-SS304 suggesting the presence of different compounds on the surface. The irregularity of the surface of the corrosion scale leads to greater disturbances in the X-ray pattern. In case of SS304, the surface was mostly covered with mixed iron oxides such as $LiFeO_2$ and $LiFe_5O_8$. In case of Co-Ni encapsulated SS304, lithiated cobalt, nickel and iron oxides covered the surface. Lithiated Co, Ni, Fe oxides are corrosion products themselves and are quite stable under MCFC cathode conditions.

The corrosion products that are unstable in molten carbonate disintegrate and are included in the adjacent electrode material. This can sometimes alter the porosity of the material and lower the performance of the electrode. In our tests, the $LiAlO_2$ separator was placed in direct contact with the SS304 and Co-Ni encapsulated SS304 plates.

AAS studies showed the presence of chromium in the melt in case of SS304 and Co-Ni encapsulated SS304. The observed chromium in the melt probably is due to the disintegration of Cr based corrosion products formed during oxidation of SS304. The $LiAlO_2$ based separator was analyzed after the experiment was completed using SEM and EDAX in order to determine the morphological and compositional changes in the separator due to the corrosion reactions occurring on the adjacent current collector. Figure 44 shows the SEM micrographs of fresh and used (Post-test from SS304 and Co-Ni-SS304 containing $3cm^2$ cells) $LiAlO_2$ separators. The morphology of post-test $LiAlO_2$ does not differ significantly from fresh separator except for the apparent decrease in void area, which probably is caused by electrolyte filling. Spot analysis by EDAX showed high chromium content in these corrosion products. EDAX analysis on the complete $LiAlO_2$ separator shows an average chromium concentration of 6.5 wt.% in case of SS304. The amount of Cr present in the case of Co-Ni encapsulated SS304 was found to be 0.24 wt. %. The observed high chromium content in case of SS304 resulted due to unstable corrosion products on the surface of the current collector.

Corrosion studies under open circuit conditions: - Open circuit potential response of SS304 and Co-Ni encapsulated SS304 as a function of time in molten carbonate under cathode gas conditions is shown in Figure 45. The potential is referenced to a gold electrode with $2CO + O_2$ as a reference gas. As shown in Figure 45, the potential of bare and surface modified SS 304 changes with time to more positive values. The potential changes from –1 V to the potential of the oxygen reduction reaction. The observed potential change is a multi-step process resulting

from different oxidation reactions occurring at the surface. The open circuit profile traced in the case of surface modified SS 304 is shown to be different than that of bare SS 304 suggesting a distinctive nature of the corrosion scale in this system. Alloy surface composition strongly determines the nature of the potential change. The complexity of the passive layer formation strongly depends on the surface composition of the alloy.

In the potential range between −1.0 V to 0.0 V, iron is oxidized to FeO and $LiFeO_2$ to $LiFe_5O_8$, while chromium is oxidized to $LiCrO_2$ and Li_2CrO_4 . Chromium oxidizes and reacts with Li_2CO_3 from the electrolyte to form a layer of $LiCr_2O_4$ which dissolves slowly into the melt [22]. Nickel and cobalt are oxidized to lithiated NiO and lithiated CoO, respectively.

The formed initial layers are highly porous in nature and lead to a slow oxidation of underlying iron to iron oxides. This phenomenon causes the second potential shift observed in the open circuit potential plot of SS304 in Figure 45. After fifteen hours of exposure in the melt, the corrosion scale consists of outer porous lithium ferrite layer with inner layers containing dense chromium oxides that prevent the external diffusion of other metal ions thereby controlling the growth of external ferrite layer.

In case of Co-Ni encapsulated SS304, the corrosion scale is made of outer CoO-NiO layers which cover the lithium ferrite and chromium oxide inner layers. The presence of CoO-NiO layers due to their barrier properties contribute to the observed decrease in chromium dissolution rate from the underlying steel substrate.

Cyclic voltammetric studies: - Figure 46 shows CV's of SS304 and Co-Ni encapsulated SS304 obtained after 2 h of immersion in the Li/K carbonate melt purged with cathode gas. The curves were recorded at a scan rate of 10 mV/s. The potential was swept from −1.6 V to 0 V in the positive direction and back to −1.6 V. This region covers the oxidation and reduction processes that may occur in the MCFC under various operating conditions.

As shown in Fig. 46, in the case of SS304 shifting the potential in the positive direction results in a peak at approximately −1.2 V. Keijer *et al* [20] observed a similar peak in their study of SS304 under cathode gas and attributed the peak to the formation of FeO by oxidation of the surface Fe. As expected, this peak was absent in case of Co-Ni encapsulated SS304. At higher positive potentials, a rapid increase in current is seen. The observed current in this region is due

to the oxidation of FeO to $LiFeO_2$ [25], formation of $LiFe_5O_8$, and chromium oxidation [25,65]. Oxidation of chromium occurs at more positive potentials than –0.3 V.

$LiCrO_2$ formed on the surface at this potential is not stable as a corrosion layer and dissolves as chromate ions [22]. In the case of stainless steel and surface modified alloys, the oxide scale is more complex than that of pure chromium. The presence of these oxides on the surface decreases the dissolution of chromate ions due to their barrier properties. Thus, the amount of chromium dissolved in the melt is a clear indication of the integrity of the passive layer formed. Further increase in the potential leads to anodic decomposition of molten carbonate [20].

Increasing the potential in anodic direction, the current increases slowly in case of Co-Ni encapsulated SS304. The observed current is attributed to the oxidation of Ni to NiO. Similar results have been reported in the literature [25]. At anodic potentials higher than -0.3 V a peak appears which corresponds to oxidation to bivalent and trivalent nickel and cobalt ions. Vossen *et al* [25] studied the anodic properties of bare Ni in molten carbonate. By using XRD analysis, they reported the presence of trivalent nickel ions in the molten carbonate melt. With the formation of trivalent nickel ions, vacancies are introduced into the lattice, which subsequently improves the ionic conductivity of the scale. Our impedance data confirmed that Co-Ni encapsulated SS304 has better conductivity than the bare SS304 due to higher concentrations of nickel and cobalt in the oxide scales.

As shown in Fig. 46, polarizing the electrodes in the negative direction from 0V results in reducing the surface oxides. The observed increase in current for Co-Ni encapsulated SS304 corresponds to the reduction of trivalent nickel ions in the oxide scale. The reduction of chromate ions present in SS304 also proceeds at the same potential. Further increase of the potential in the cathodic direction to –0.9 V results to the reduction of α-$LiFe_5O_8$ to $LiFeO_2$ and then to FeO. Nickel oxide in Co-Ni encapsulated SS304 also reduces to metallic Ni at this potential.

Tafel polarization studies: - To quantify the redox reactions occurring on the surface of the current collector, Tafel curves were obtained at different temperatures in the presence and absence of the oxidant gas.

Tafel polarization studies were carried out in a three-electrode 3-cm^2-lab scale cell containing SS304 and Co-Ni-SS304 electrodes as working and counter electrodes. Gold (oxygen

54

reduction) served as a reference electrode. The electrodes were separated by a $LiAlO_2$ ceramic tile containing Li/K carbonate melt (62-38mol%). The cell was connected to a gold/oxygen reference electrode through a salt bridge. The potential was scanned at a rate of 25 mV/s. Figure 47 compares the Tafel polarization curves obtained for SS304 under different gas and temperature conditions. In the presence of cathode gas, the electrode potential was observed to be close to 0 V (vs. $Au/[2CO_2+1O_2]$) indicating that the potential is controlled by the oxygen reduction reaction. In the absence of gas, the potentials shift to – 0.25 V (vs. $Au/[2CO_2+1O_2]$), which is the mixed potential of the various metal oxides present on the steel substrate. In the presence of gas, the cathodic scan represents the oxygen reduction reaction occurring on the surface of the electrode. When the potential is scanned in the anodic direction, the current denotes the oxidation of the O^{2-} species along with the anodic decomposition of the carbonate electrolyte [20,25]. In the absence of gas, the cathodic reaction represents the mixed reaction between oxygen reduction reaction (coming from the reference gas) and the reduction of surface metal oxides. The high scan rate ensures minimum irreversible changes on the surface. During the anodic scan the oxidation of the O^{2-} species occurs along with the oxidation of metal to metal oxide.

Figure 48 shows the Tafel polarization curves obtained for Co-Ni encapsulated SS304 under similar conditions. In case of Co-Ni-SS304, both the cathodic and anodic currents were larger than the corresponding currents in case of SS304. This indicates that the oxygen reduction reaction, which contributes predominantly to the observed currents in the Tafel polarization curves, occurs at a faster rate on Co-Ni encapsulated SS304 substrate. This is to be expected, because Co-Ni encapsulated SS304 forms a CoO-NiO rich corrosion scale which has a higher exchange current density for the oxygen reduction reaction when compared to that of iron oxides, which is a corrosion scale on SS304.

Effect of corrosion scales on electrolyte management: - Electrolyte distribution significantly affects the performance characteristics of the electrodes. The tendency towards capillary equilibrium is utilized to control the electrolyte distribution of the fuel cell cathodes and anodes. Thus, formation of a porous corrosion scale on the bipolar plates can contribute to the disturbance of the electrolyte management scheme due to capillary action. Therefore, apart from the induced loss of electrolyte due to the interaction of chromium (from SS) with Li_2CO_3, the

porous corrosion scales can also be expected to compromise the electrolyte management thereby affecting the performance of the electrode. EDAX analysis carried out on the corrosion scales of SS304 and Co-Ni encapsulated SS304 samples taken from a MCFC cell showed the presence of potassium which may come only from the $Li_2CO_3+K_2CO_3$ electrolyte. This observation agrees with our argument that the porous corrosion scale would be wetted by the electrolyte. The extent of wetting could however be very small considering the small surface area of the corrosion scales. In this context, the advantage provided by the higher exchange current density of Co-Ni oxides on the Co-Ni-SS304 when compared to that of iron oxides in SS304 becomes quite significant.

Electrochemical Impedance Spectroscopy (EIS) studies: -In order to understand better the reactions occurring on SS304 and Co-Ni-SS304 under MCFC conditions, impedance measurements were carried out as a function of different gas compositions and temperatures. EIS analysis was carried out using the same electrochemical set up described in the Tafel polarization studies. EIS analysis was performed at open circuit on SS304 and Co-Ni-SS304 electrodes in the presence and absence of gas.

Figure 49 shows the impedance analysis of SS304 electrode at different temperatures and gas conditions. The impedance response at any given temperature is characterized by the presence of two arcs. The high frequency arc has a slope of 0.5 that could be representative of the conductivity of the porous electrode. The low frequency loop indicates a complex charge transfer and mass transfer controlled reactions occurring on the surface of the corrosion scale. The oxygen reduction reaction predominates at the electrode surface in the presence of oxidant. When the gas supply is discontinued, the oxygen reduction reaction still proceeds on the surface depending upon the availability of dissolved oxygen in the melt. However, the extent of this reaction is small owing to the decreased availability of oxygen, which in turn causes the potential to shift to that of the metal oxide value. The impedance begins to decrease gradually with time when the gas supply is discontinued before stabilizing after about 4 hours. The impedance response followed a similar trend at higher temperatures. However the magnitude of the polarization resistances for surface reactions decreased considerably. This can be expected due to the dependence of the activation energy of the reactions on the temperature. The conductivity of the porous scale is also seen to increase at higher temperatures.

Figure 50 shows the impedance response of Co-Ni-SS304 electrode as a function of different gas compositions at three different temperatures. The impedance responses are very similar to those obtained in case of SS304 except for the difference in the magnitude. Co-Ni encapsulation on SS304 leads to a formation of CoO-NiO rich corrosion scales on the surface of the surface modified current collector. CoO-NiO has a higher exchange current density for oxygen reduction reaction when compared to that of iron oxides. Therefore a smaller polarization resistance can be expected in case of Co-Ni encapsulated SS304 when compared to that of SS304. This explains the observed decrease in impedance in case of surface modified SS304 when compared to that of SS304. Temperature also has a similar influence as in the case of bare SS304 wherein the magnitude of polarization resistance decreases with increase of temperature.

Careful examination of these impedance curves suggests that the loops, which are observed in both cases for Co-Ni encapsulated SS304 and SS304, are either depressed semicircles or arcs of semicircles whose center is displaced from the real axis. The data can be compared with the impedance of a plausible electrical equivalent circuit by complex nonlinear least squares fitting (CNLS) to extract parameters (circuit elements) which can be related to physical processes which are believed likely to be present. Although we typically employ ideal resistors, capacitors and inductances in an equivalent circuit, actual real elements only approximate ideality over a limited frequency range. In this work, the impedance loops are present as depressed semicircles signifying deviation from ideality. To compensate for this deviation from reality, a distributed phase element was added to the equivalent circuit. Figure 51 shows the electrical equivalent circuit that was used to fit the experimental impedance data obtained for the case of SS304 and Co-Ni-SS304. The distributed element used in the equivalent circuit is a *Zarc-Cole* type wherein a constant phase element (CPE - signifies the semi-infinite non-uniform diffusion occurring in a porous electrode), is placed in parallel with an ideal resistor (reaction resistance). The *Zarc* produces a complex plane curve, which forms an arc of a circle with center, displaced from the real axis. Further details about the *Zarc-Cole* fitting and CPE can be obtained from literature [58].

The parameter conductivity of the porous electrode, R_1, and polarization resistance, R_2 (in presence of gas), which are extracted from the impedance response using the equivalent circuit model, is summarized for both Co-Ni-SS304 and SS304 in the next table.

	EIS Equivalent Circuit Fit	
Current Collector	Porous electrode Ohmic Resistance (Ω)	Polarization Resistance (Ω)
SS304	~5.3	120.68
Co-Ni-SS304	~1.3	22.86

The polarization resistance in the presence of oxidant is significantly lower in case of Co-Ni-SS304 (22.86 Ω) when compared to SS304 (120.68 Ω). This can be expected because of the poor kinetics for oxygen reduction on the iron oxide substrate when compared to CoO-NiO. The resistance R_l denoting the conductivity of the porous electrode obtained for SS304 at 650°C using the equivalent circuit model varied between 5.71 Ω and 5.29 Ω while it varied between 1.32 Ω and 1.28 Ω for the case of Co-NiO-SS304. This shows that the corrosion scale formed in case of Co-Ni-SS304 has a higher conductivity when compared to the corrosion scale formed on SS304. The polarization resistance R_2 and ohmic resistance R_l at 700°C and 750°C followed similar trend as the case of 650°C even though the magnitude was significantly lower at higher temperatures suggesting improved kinetics and better conductivity.

Cathode Model

The model equations are highly nonlinear and coupled in nature and hence cannot be solved analytically. The five governing equations (Eq. 37-39) with the appropriate boundary conditions (Eq. 40 and 41) have been solved simultaneously using Femlab 2.1 (a commercial software package based on finite element analysis) and also using Newman's Band(j). In studying the performance of the cathode, the main parameter of interest is the electrode polarization under different applied currents. The measured polarization is the difference in potential between the current collector $(\Phi_M)_o$ under load as compared to at open circuit $(\Phi_M)_{o,OCV}$. However, the model solves for the local overpotential f, which is the difference

between the solid phase and liquid phase potential. Lee *et al.* [35] present a relationship between this overpotential and the experimentally measured polarization loss (Φ_{Mo}-$\Phi_{Mo,OCV}$). The IR free polarization is given as,

$$\boldsymbol{f}_{IR-free} = \left(\Phi\right)_0 + \frac{1}{1+\boldsymbol{k}_{app}/\boldsymbol{s}_{app}}\left[\left(\Phi\right)_L - \left(\Phi\right)_0\right] \tag{65}$$

where $\boldsymbol{k}_{app}$ and $\boldsymbol{s}_{app}$ are the apparent conductivities modified by the porosity. $\left(\Phi\right)_L$ and $\left(\Phi\right)_0$ are the overpotentials at the matrix side and the current collector side of the electrode as defined by Lee *et al.* [35] Using the model we studied the effect of different parameters on the IR free polarization loss.

Effect of Conductivity:

Ohmic losses in the MCFC cathode can arise due to poor conductivity of either the electrode or the electrolyte. The electrolyte here is an eutectic mixture of Li_2CO_3-K_2CO_3 held in a lithium aluminate matrix. Electrolyte fills inside the porous cathode due to capillary forces. In general the conductivity of the electrode material is much larger than that of the electrolyte. The conductivity of the melt lies in the order of 10^{-2} S/cm while solid phase (electrode) conductivities are in the order of 10 S/cm. Figure 52 presents the polarization loss at various loads for different values of the electrolyte conductivity. The model simulations were run with a σ value of 13 S/cm. From Fig. 52 it can be seen that increase in κ decreases the polarization loss. At large values of κ (2.0 S/cm) a linear relationship is seen between the polarization loss and the applied load. With decreasing values of κ, the polarization loss increases exponentially with increasing applied current. For κ=2.0 X10^{-2} S/cm it can be seen that changing the applied current from 160 mA/cm^2 to 200 mA/cm^2 results in increasing the polarization loss by 15 mV. A similar change in current for κ=2.0 S/cm would increase the polarization loss only by 3 mV. While the model simulations show a significant effect of the electrolyte conductivity on electrode performance, in reality the choice of electrolyte is limited by other considerations. Stability at high temperatures, low dissolution of cathode material and current collector in the melt play a critical role in limiting the choice to a few eutectic mixtures. While the difference in conductivity between these different melts is not significant, the effective electrolyte conductivity depends strongly on the cathode design. The effective electrolyte conductivity is affected by the degree of electrolyte fill

in the cathode, which in turn is influenced by the number of macropores and micropores in the cathode. In order to study this we plot the local overpotential across the thickness of the electrode for different κ values. As seen from Fig. 53, the difference between the solid and liquid phase potentials increases with increase in distance from the current collector. With decreasing values of κ most of the polarization drop occurs close to the matrix.

Figure 54 and 55 present the change in reaction rate di_2/dx across the thickness of the electrode. The variable di_2/dx is a measure of the reaction rate or the current transferred per unit volume ($a^{(sl)}\langle j_k \rangle^{(sl)}$) and is given by Eq. 34. The reaction rate is plotted as a function of two different dimensionless parameters, γ_1 and γ_2 as defined by equations 45 and 46. The parameters γ_1 and γ_2 are a measure of the electrode and electrolyte resistivity respectively. As seen from Fig. 54 changes in γ_2 have a significant effect on the reaction rate di_2/dx. These simulations have been done after fixing the ohmic conductivity of the electrode, i.e. γ_1. With increase in γ_2 (high electrolyte resistance), the reaction rate remains close to zero in most part of the electrode. In general it is preferable to have an electrode with a uniform reaction rate distribution everywhere. The model simulations indicate that if γ_1 and γ_2 differ significantly (over 2 orders of magnitude) most of the reaction occurs within a zone close to the current collector and electrolyte matrix. The rest of the electrode does not take part in the reaction and this represents a loss of effective active material. Figure 55 presents the model results when the electrolyte conductivity (γ_2) is fixed and the electrode conductivity (γ_1) is varied. In both Fig. 54 and Fig. 55, it can be seen that when γ_1 and γ_2 are comparable to each other the reaction rate does not go to zero across the electrode. However, both low electrode and electrolytic conductivity lead to very poor reaction rate distribution across the electrode. For all cases, the reaction rate remains high close to the current collector and matrix. When the electrolytic and ohmic conductivities are equal to each other a symmetrical reaction rate distribution curve is obtained. This is similar to the analysis given by Newman [61] for porous electrodes. Although a uniform reaction distribution is the desirable scenario practical considerations limit us from achieving this. As mentioned before, in general solid phase conductivities are much larger than liquid phase conductivities. Hence, the actual electrode utilization is not 100% but much lower than that. Using this theoretical model it is possible to optimize the electrode thickness based on input electrode parameters.

Effect of Exchange Current Density:

We next study the effect of reaction kinetics on the electrode performance. Various mechanisms have been proposed for the cathode reaction in MCFC. While the exact nature of the reaction is under discussion, the rate of the reaction can be measured easily. Similar to electrode conductivity, the oxygen reduction rate varies significantly on different materials. The state-of-art cathode material in MCFC is NiO with a reported i_0^0 value of 0.81 mA/cm^2 [35]. Alternate materials such as LiCoO$_2$ (i_0^0 =0.5 mA/cm^2)[9] and LiFeO$_2$ (i_0^0 =0.1 mA/cm^2) [35] have been tested as cathodes since they exhibit lower corrosion rates in the melt. Figure 56 presents the polarization loss at different currents for various i_0^0 values. As seen from the plot, varying i_0 has a significant effect on the polarization loss. As i_0^0 decreases the overpotential increases as result of increased kinetic resistance as shown in Figure 57. Similar to κ at high values of i_0^0 the polarization loss increases linearly with increasing applied loads. However, at low values of i_0^0 the polarization loss increases asymptotically and reaches a plateau with increase in current. This is in contrast to Fig. 53 where decrease in kappa increases the potential drop exponentially. As i_0 decreases, the reaction rate also decreases. Due to slower reaction rate mass transfer becomes competitive with reaction kinetics. Hence increasing the current density does not translate into increased polarization loss. These results agree well with those reported earlier by Lee *et al.* [35] Figure 57 shows the overpotential profiles for different exchange current densities. The simulations were performed for an applied current of 160 mA/cm^2. The overpotential increases sharply near the matrix side of the electrode. It can also be seen that the large potential drop close to the electrolyte matrix increases with decrease in i_0^0. This directly translates to a large polarization drop across the electrode (see Fig. 56). In our simulations we assumed that a di_2/dx value lesser than 5% of the maximum reaction rate indicated a dead zone with no reaction. The percent utilization of the active material is calculated for different i_0^0 using this baseline (5% of the maximum reaction rate). Figure 58 shows the percent utilization of the electrode material as a function of the exchange current density. It can be clearly seen that as i_0 increases the utilization decreases indicating that only a small fraction of the electrode takes part in the reaction. Most of the reaction takes place in a small part of the electrode near the electrolyte tile. Figure 55 shows that materials with high i_0^0 values have low polarization drops. However, from Fig. 58 it can be

seen that increase in i_0^0 translates to poor utilization of active material. For small i_0^0 values the reaction rate is slow and hence this allows sufficient time for dissolved O_2 and CO_2 to reach the active solid interface and react. The slow reaction rate also allows the reaction to take place much deeper within the electrode as compared to at high reaction rates. Both these factors contribute to the higher utilization observed for low i_0^0 values.

Effect of diffusion coefficient:

The reactants in the gas phase diffuse from the gaseous macropore to the catalyst surface through the micropore, which has the electrolyte. Here we study the effect of mass transfer through the electrolytic phase. Figure 59 presents a comparison of the liquid phase carbon dioxide concentration across the electrode for different values of the diffusion coefficient. It can be seen that change in liquid phase diffusion coefficient significantly alters the concentration across the electrode. At very low values (10^{-4} cm^2/s) of $D_i^{(l)}$ the O_2 and CO_2 concentration close to the matrix drops to zero (not shown in figure). However, the diffusion coefficient for both dissolved oxygen and carbon dioxide in MCFC cathodes lies in the order of 10^{-3} – 10^{-2} cm^2/s. [34] From Fig.59 it can be seen that at this value of the diffusion coefficient no depletion of dissolved CO_2 occurs anywhere within the electrode. A linear concentration gradient exists across the thickness of the electrode for both O_2 and CO_2. The overpotential is almost uniform for large diffusion coefficients whereas for small diffusion coefficients the overpotential increases drastically very near the matrix region (not shown in figure). A similar effect is seen by varying both O_2 and CO_2 diffusion coefficients. Also, simulation results show that changing the diffusion coefficient by one order of magnitude results in an increase in polarization of only 20 mV. This effect is smaller than that seen for electrolyte conductivity and exchange current density. These results indicate that mass transfer in the liquid phase is not rate limiting for MCFC cathodes.

Effect of thickness of the electrode:

The resistance to mass transfer increases as the electrode thickness increases. Hence the polarization increases with the thickness as shown in Fig. 60. This agrees with the prediction by Prins-Jansen *et al* [29]. Their simulations considered changing the thickness keeping all other

parameters constant similar to what has been done here. As suggested by Prins-Jansen *et al.* [29] increasing the thickness has two conflicting effects, both the mass transfer resistance and the active surface area are being increased. The upward bending effect seen in Fig. 60 is due to the increase in the mass transfer resistance. Due to the competing effects of mass transfer and increase in surface area, the polarization loss should go through an optimum as the electrode thickness is increased. However, both in our model simulations and in Prins-Jansen *et al.* [29] we observe a monotonic dependency where polarization loss always increases with increase in thickness. This can be attributed to the assumption involved in the model simulation i.e. the active surface area does not change with increase in thickness.

Fontes *et al* [37] state that optimum electrode thickness is shifted towards thicker electrodes as the electrolyte conductivity increases. Increase in κ increases the utilization of the active material as shown in Fig. 53. Hence the thickness of the electrode can be increased with increased electrolyte conductivity to obtain similar performance. Figure 61 plots the CO_2 gas phase concentration across the electrode thickness. It can be seen that even under high utilization (40% - 60%) all the gas in the electrode is not consumed. For an electrode thickness of 0.6 mm close to 40% of the inlet gas is still available at the outlet**.** In MCFC stacks, it has been estimated that the utilization of the oxidant gases is around 40-50%. The change in gas phase concentration does not have a significant effect on the electrode performance at high gas flow rates. However, decrease in both oxygen and carbon dioxide flow rate will affect the performance of the cathode. The liquid phase reactant concentrations are directly dependent on the gas concentration in the macropore at that point. Low flow rates contribute to high utilization thereby leading to a decrease in gas phase concentration. This will decrease the amount of reactant available for taking part in the reduction reaction at the solid/liquid interface and hence increase the polarization loss as seen in Fig. 60.

Comparison of cathode model to experimental data

Figure 62 compares the model to our experimental data of $LiNiCoO_2$ at different temperatures. With increase in temperature the reaction rate as given by the exchange current density and the species transport rate as given by the diffusion coefficient increase. Further the electrolyte conductivity also increases. The gas phase diffusion coefficients at different temperatures can be calculated using the Fuller correlation [46]. The temperature dependency of

the liquid phase diffusion coefficients, electrolyte conductivity and the exchange current density were determined by fitting the model to the experimental data. In all cases an Arrhenius relationship to the temperature was obtained. The fitting results along with the R^2 term are given in Table II. The dependence is given by

$$x = a\exp\left(-\frac{b}{T}\right)$$

The parameters obtained from fitting the model data were used in the subsequent simulations. Our next goal was to compare the polarization behavior of the cathode under different gas compositions.

Our model predicts monotonic dependence of the polarization loss on both CO_2 and O_2 partial pressure. The exchange current density is concentration dependent and has negative reaction order dependence for CO_2 and positive order dependence for O_2. Increasing the concentration of CO_2 decreases the local current density and hence increases the polarization. The effect is the reverse for O_2. Similar results have been obtained by previous researchers also. This is shown in Fig.63, which gives the fit of our model to experimental data of $LiCoO_2$ at low overpotentials obtained by Lagergren and Simonsson [62] for different gas compositions. The model parameters remained the same as for $LiNiCoO_2$ (see Table II) except for the exchange current density, which was calculated as 5 mA/cm^2 at 650°C.

Figure 64 presents comparison of polarization profiles between three different cathode materials namely, NiO, $LiCoO_2$ and $LiNiCoO_2$. For all three cathode materials good agreement is seen between model simulations and experimental data. NiO is a p type semiconductor and has a lower conductivity than pure Ni. Li$^+$ ions coming from the electrolyte, diffuse into the NiO and increase its electronic conductivity. However, NiO has much larger exchange current density for oxygen reduction as compared to alternate cathode materials such as $LiNiCoO_2$ and CoO_2. Model simulations indicate that an electrode made of a material, which has the conductivity of NiO, and exchange current density of $LiCoO_2$ would suffer around 100% more polarization than the conventional NiO cathode. The exchange current density and electrode conductivity of the three materials obtained using the homogeneous model are given in Table III. These results show that the model can be used to extract critical thermodynamic, kinetic and transport parameters from polarization data.

Full Cell Model

There are eight unknowns, solution phase potential ($\langle j \rangle^{(l)}$), solid phase potential ($\langle j \rangle^{(s)}$), dimensionless concentration in the liquid and the gas phases for the three gas components ($u_i^{(g)}$ and $u_i^{(l)}$ respectively for species 'i', i = CO_2, O_2 or H_2). The set of governing equations and boundary conditions (48-64) are solved for these eight variables using FEMLAB 2.2 and the results are discussed in the following section. Model simulations were run with the set of parameters given in Table IV. The equilibrium potentials in the cathode, E_{eqc} and the anode, E_{eqa} are 0.0 and –1.02 volts respectively with respect to oxygen reduction on gold. Cell potential is calculated from the difference in solid phase potentials at x = 0 and x = L i.e. $V = \langle j \rangle^{(s)}|_0 - \langle j \rangle^{(s)}|_L$. Overall drop is determined by finding the deviation of the cell potential from equilibrium potential ($V_{eq} - V$). The drop in the cathode, separator and the anode are detemined as $E_{eqc} - \left(\langle f \rangle^{(s)}|_0 - \langle f \rangle^{(l)}|_{x_1} \right)$, $\langle f \rangle^{(l)}|_{x_1} - \langle f \rangle^{(l)}|_{x_2}$ and $E_{eqa} - \left(\langle f \rangle^{(l)}|_{x_2} - \langle f \rangle^{(s)}|_L \right)$ respectively. The cell potential determined using model simulations might be different from the experimental values due to resistance in current collectors. But the model is based on the assumption that the resistance in the current collectors is negligible.

Polarization drops across cell

A clear understanding of the significance of different cell components is necessary. Figure 65 shows the drop in the cathode, anode, electrolyte tile (matrix) along with the overall drop in potential for different applied current densities. It is obvious that the drop in the cathode and anode is smaller compared to the overall drop. The huge drop in the matrix is attributed to the ohmic loss in the electrolyte. This agrees with previous results [63] where 70% of the total cell potential is attributed to ohmic losses in the electrolyte. Also, as the current density increases the percentage drop in the matrix decreases and the losses in the matrix and rest of the fuel cell become comparable as shown in Fig. 66. The percentage increase in the cell potential drop with increasing current density is more in the electrodes than in the matrix (a higher exponential dependence of the potential drop on current density in the cathode than in the matrix). This can

be attributed to the concentration polarization in the cathode, which increases exponentially with increasing current density (the upward bending effect due to mass transfer limitations).

The drop in the matrix is seen clearly by plotting the liquid phase potentials in the cathode, matrix and the anode as shown in Fig. 67. It can be seen that there is a large jump in the liquid phase potential in the matrix and a considerable drop in the cathode. The drop in the anode remains almost the same. Also, as the applied current density increases this jump in the liquid phase potential increases both in the matrix and the cathode. Change in solid phase potential is negligible since the electronic conductivity is high. But the liquid phase potential changes significantly with current density. Since $\langle f \rangle^{(l)}$ increases and $\langle f \rangle^{(s)}$ remains the same, the overpotential increases ($\langle f \rangle^{(s)} - \langle f \rangle^{(l)}$) increases leading to a drop in cell potential.

Figure 68 shows the profile of potential drop for varying matrix thickness for different applied current densities. Potential drop increases with matrix thickness as well as current density. But as the current density increases the slope of potential drop vs. matrix thickness increases. Hence decreasing the matrix thickness will improve the performance of molten carbonate fuel cell. This has been observed by previous researchers [63]. They found that the voltage drop (ΔV_{ohm}) followed a trend with the thickness (i.e. $\Delta V_{ohm}=0.533t$). But there are practical constraints to it. We are very well aware of the dissolution of the cathode material in the electrolyte. If the matrix thickness is small then the Ni++ diffusion from the cathode to the anode is easier and the cell is shorted in a short span of time. This leads to a decrease in the life of the fuel cell. Hence a compromise must be made between the life of the fuel cell and the cell performance while choosing the matrix thickness.

Importance of concentration polarization

Figure 69 gives the cell potential for different applied current densities. There are two cases shown, case 1 with concentration effects and the case 2 assuming negligible concentration gradients. Case 1 is the result of the model that takes into account the concentration gradients in the gas and the liquid phase along with potential gradients and activation control. Case 2 presents the model simulations that take into account only the potential gradients and activation control and neglect concentration gradients both in the liquid phase and the solid phase. A small difference in the cell potentials is observed between the two different cases at low current

densities. As the current density increases this difference increases exponentially. At low current densities ohmic effects dominate and mass transfer effects are negligible. But as the current density increases there is mixed control (ohmic and mass transfer). The difference between the two models yields the concentration polarization (mainly in the cathode). Figure 70 shows the plot of concentration polarization for different current densities, which increases exponentially with increasing current densities. Concentration polarization is calculated by finding the difference in polarizations between the two cases. At low current densities the rate of the reaction is low and the reactant concentrations are very near to the inlet concentrations. But as the current density increases more of the reactants get consumed and the concentration decreases. Hence concentration polarization increases as the current density increases. Plotting overpotential vs. current density will show a linear curve for case 2 and an upward bending curve for case 1. This upward bending effect is due to mass transfer limitations and has been discussed in the simulations of the cathode model. The matrix thickness in this simulation was 0.1 cm. But changing the matrix thickness does not change the concentration polarization. This is because of the assumption that there is no gas crossover and hence there is no gas going into the matrix. Changes in the concentrations do not affect the drop in the matrix. Though the entire concentration polarization lies mainly in the cathode (and the anode to a smaller extent), its value is appreciable especially at high current densities. So to model the system accurately concentration gradients have to be taken into account. Figure 70 also shows the effect of electrolyte conductivity k on concentration polarization. It shows that the concentration polarization is small for high electrolyte conductivities. For lower values of k the mass transfer effects are significant.

Local current density

The local current density profiles are given in Fig. 71. The local current density remains almost the same throughout the cathode except near the matrix and the current collectors. This suggests that most of the reaction occurs at the current collector-cathode and cathode-matrix interface. When the applied current density is increased this non-uniformity in the local current density increases further more. The same is observed in the anode though here most of the reaction occurs at the matrix-anode interface. This suggests that we cannot use a constant local current density along the whole length of the electrode i.e. the zero order approximation given by

Standaert *et al*. [41]. Also the local current density cannot be assumed to vary linearly as can be seen clearly from Fig.71. So the first order approximation suggested by Standaert *et al*. [41] is also not true. In the cathode the cathodic part of the current density from Butler Volmer equation is high compared to the anodic part. Hence we observe a negative local current density. In the anode the anodic term is high leading to a positive local current density. This can be seen clearly in the simulation results. The electrolyte conductivity was kept at 2.0 S/cm during these simulations.

Effect of parameters

Since we know that most of the drop is in the matrix let us analyze the importance of electrode parameters on the electrode polarization: exchange current density and electrode conductivity. Different electrode materials have different exchange current densities; cathode materials: NiO - 50 mA/cm^2 [64], LiCoO2 - 5 mA/cm^2 [64], LiNiCoO^2 - 0.65 mA/cm^2 [64]; anode material: Ni - 110 mA/cm^2. Simulations were run for different exchange current densities of the cathode keeping all other parameters constant. The same was done in the anode. The results are shown in Fig. 72 and Fig. 73. Electrolyte conductivity k was kept at 0.02 S/cm in the simulations of these two figures. As can be seen from Fig. 72 the cell voltage increases sharply when the cathode exchange current density ($i_{0,c}^0$) is increased from 0.1 mA/cm^2 to 1 mA/cm^2 and increases again till $i_{0,c}^0$ is around 5 mA/cm^2. But above 5 mA/cm^2 increasing the $i_{0,c}^0$ does not affect the cell potential. This is the case for any applied current density although the cell potentials vary with the applied currents. The same is observed with the anode exchange current density $i_{0,a}^0$ as shown in Fig. 73. This is because at low values of $i_{0,c}^0$ the system is under kinetic limitations of the cathode. As $i_{0,c}^0$ increases cathode kinetics is no longer the limiting factor and other phenomena control the performance (mass transfer or ohmic or mixed control). The electrode conductivities show a similar behavior. Figure 74 shows the effect of cathode conductivity on cell potential. Below 1 S/cm any further decrease in the cathode conductivity decreases the cell potential drastically. The cell is already under limitations due to ohmic resistance in the electrolyte due to the low electrolyte conductivity of 0.02 S/cm. Any decrease in the cathode conductivity will add to ohmic limitations and result in a sudden decrease in the cell performance. But for cathode conductivity above 1 S/cm the increase in cell potential is

negligible. The state of art cathode materials have the following conductivities; NiO - 13 S/cm, $LiCoO_2$ – 1 S/cm, $LiNiCoO_2$ – 5 S/cm. This suggests that $LiCoO_2$ will suffer from huge ohmic limitations. Also these simulations suggest that for a particular anode material improving the cathode material does not affect the overall performance after an extent and vice versa. Figure 75 shows the effect of electrolyte conductivity on performance. The behavior is similar to electrode conductivity and exchange current density. The cell potential follows an asymptotic profile with increasing electrolyte conductivity at all applied currents. From 0.02 S/cm to 0.2 S/cm there is a wide difference in cell potentials. But from 0.2 S/cm to 1 S/cm the cell potential increases slightly. Thus trying to increase the electrolyte conductivity to 0.2 S/cm for a given set of cathode and anode materials will improve the performance of the full cell but there are practical limitations to increasing the electrolyte conductivity.

Comparison to experimental data

Fig.76 shows the results of the model simulation along with the experimental data of Soler *et al.* [65]. All the three curves fall closely. The parameters used in the cathode were taken from the previous paper [64] where the cathode data was fitted to the experimental data. The anode data was fitted separately before attempting to fit the full cell data. The cathode and anode parameters used in the model simulation are given in Table IV. In the cathode and anode the effective electrolyte conductivity is calculated using the Bruggeman formula. ($k_{eff} = ke^{1.5}$). We were not able to fit the data using such a relation in the matrix. An effective conductivity greater than the one estimated by the Bruggeman relation has to be used in the matrix to fit the model to the experimental data. Doyle *et al.* [66] report a similar dependence of the effective conductivity in the plasticized electrolyte in a Plastic lithium ion cell (where they report a conductivity lesser than that predicted by the Bruggeman relation) though the Bruggeman formula holds good in the cathode and the anode

In MCFC the cell potential varies linearly with the applied current density. This is observed both in the model simulations and the experimental data. This is expected because the activation polarization observed in low temperature fuel cells at low current densities vanishes in high temperature cells.

Power Density

Next we bok at how the power density changes with increasing load for different cell thickness as shown in Fig. 77. Power density is defined as the product of the applied current density and the voltage. We see that there is maximum power density around 200 mA/cm^2 for a cell thickness of 0.26 cm. At low current densities the power density increases as the current density increases. But above 200 mA/cm^2, increase in power due to increase in current density cannot compensate for the increase in polarization losses. Hence the curve goes through a maximum. Also it should be noted that in practice the point of maximum power density does not correspond to optimum power density, since at this point the internal heat generation is high and undesirable for fuel cell operation. Hence the fuel cell is operated at much lower power densities. When the thickness is decreased the maximum power density increases. This is attributed to the reduction in polarization due to reduced thickness. Thus reducing the thickness increases the optimum power density and enables operation at higher power densities.

CONCLUSIONS

Novel Cathodess:- Surface modification was used as to improve the performance of conventional Nickel Oxide cathodes used in molten carbonate fuel cells. Using this approach Co was coated on sintered tape Ni oxide cathodes. SEM analysis was used to show the morphological changes in the sintered tape due to Co coating. Cobalt coated electrodes have a lower solubility in the molten carbonate melt when compared to bare nickel electrodes under cathode gas conditions. The solubility decreased more than 50% due to micro encapsulation with cobalt. The oxidation behavior of cobalt-encapsulated electrode was very similar to that of bare Ni. However, thermal oxidation rate was much lower in case of cobalt-encapsulated electrode. The i-V characteristics and polarization behavior for Co encapsulated NiO is different from that of NiO. A small increase in polarization in case of Co-NiO was seen to be due to reduced exchange current density. Impedance spectroscopic studies do not indicate any change in mechanism in case of Co-NiO when compared to NiO.

Apart from Co coating of Ni oxide tapes, we also tried electroless plating of Co on Ni particles. SEM analysis showed no major changes in the nickel particle size. Subsequent to deposition electrodes were prepared from Co coated Ni powders by tape casting and sintering. Cobalt coated nickel powder electrodes have a lower solubility in the molten carbonate melt when compared to bare nickel electrodes in the presence of cathode gas conditions. The solubility decreased more than 50% due to micro encapsulation with cobalt. The oxidation behavior of cobalt-encapsulated electrode was very similar to that of cobalt coated NiO cathode. The i-V characteristics and polarization behavior for Co encapsulated NiO is different from that of NiO. A small increase in polarization in case of Co-NiO was seen to be due to reduced exchange current density. Impedance spectroscopic studies do not indicate any change in mechanism in case of Co-NiO when compared to NiO. This suggests that cobalt encapsulation of nickel particles can be regarded as an alternative to improve the performance of conventional nickel oxide cathodes in molten carbonate fuel cells.

Apart from Co, $La_{0.8}Sr_{0.2}CoO_3$ (LSC) was coated on the state-of-the-art nickel electrode by a sol-gel method. LSC coating followed by sintering yielded electrodes with good pore structure. No significant difference in particle size of the LSC-NiO electrodes was seen before and after immersion in molten carbonate for 200 hours. Short-term stability tests in molten

carbonate melt at 650 $^{\circ}$C showed that the coating is effective in bringing down the nickel dissolution. The impedance behavior of LSC-NiO in a half-cell is similar to that of conventional nickel oxide electrodes. Polarization studies showed 109 mV loss for an applied current of 160 mA/cm^2. However, extensive pore volume distribution studies need to be done to optimize the pore structure and porosity, which is expected to give minimum cathode polarization values.

Apart from surface modification of NiO, $LiNi_xCo_{1-x}O_2$ was studied as an alternate cathode material. It was synthesized by solid-state reaction from lithium nitrate, nickel hydroxide and cobalt oxalate precursors. Lithium loss occurred during sintering of these mixed oxides and this loss gradually decreased with the increase in cobalt content. $LiNi_xCo_{1-x}O_2$ show lower rate of dissolution in molten carbonate under cathode gas conditions when compared to that of NiO. The rate of dissolution decreased with increase in cobalt content. However, considering the economy of cobalt doping, and stability at higher temperatures, $LiNi_{0.8}Co_{0.2}O_2$ was chosen for further characterization studies. $LiNi_{0.8}Co_{0.2}O_2$ cathodes for MCFC were made by a tape casting and sintering process. SEM analysis on $LiNi_{0.8}Co_{0.2}O_2$ electrodes sintered at 800°C show good pore structure. Pore volume distribution studies done using mercury porosimetry showed lower porosity when compared to that of state-of-the-art cathode. The i-V characteristics of $LiNi_{0.8}Co_{0.2}O_2$ are good offering a current drain of 160 mA/cm^2 for a voltage polarization (IR free) of 140 mV. Impedance spectroscopic studies done on $LiNi_{0.8}Co_{0.2}O_2$ under different gas conditions indicate that the oxygen reduction reaction mechanism follows a positive order for O_2 concentration and negative for CO_2. This suggests that the oxygen reduction mechanism is qualitatively similar to that of state-of-the-art cathode listed in literature. Finally $LiNi_{0.8}Co_{0.2}O_2$ can be regarded as an alternate material to the conventional nickel oxide cathodes in molten carbonate fuel cells.

Current Collector:- The current collector corrosion properties were studied. Surface modification was used as an alternate current sollector. SS 304 was electroless plated with monolayers of nanostructured Co-Ni. Immersion tests that were carried out on SS304 and Co-Ni encapsulated SS304 indicated higher chromium dissolution rate in case of SS304 when compared to Co-Ni encapsulated SS304. SEM and EDAX analysis of the posttest SS304 indicated a loss of Cr from the surface. The surface composition of Co-Ni-SS304 showed very little change in terms of Co and Ni content suggesting that the corrosion scale predominantly

consists of Co and Ni oxides. XRD patterns of the corrosion scales indicated the presence of lithium ferrite along with $LiFe_5O_8$ in the case of SS304 and mixed lithium-cobalt-nickel-iron oxides in the case of Co-Ni-SS304.

The open circuit potential response of the SS304 and Co-Ni-SS304 measured as a function of the exposure time showed the presence of several plateaus due to the different corrosion reactions occurring on the surface of the sample. Cyclic voltammetry was used as a qualitative technique to compare the effect of surface modification and it was observed that the currents due to formation of scale were significantly lower in case of surface modified SS 304 when compared to bare steel. Conductivity of the corrosion scale was higher in the case of Co-Ni encapsulated SS304 when compared to SS304. Polarization resistance for oxygen reduction was significantly lower in the case of Co-Ni-SS304 when compared to SS304 due to the presence of CoO and NiO on the surface as compared to $LiFeO_2$ in case of SS304.

Cathode Model:- Mathematical models were used to identify the effect of different parameters on the performance of the cathode and the full cell. The electrolyte conductivity and exchange current density have very large effect on the performance of MCFC cathode as compared to other parameters. Due to low electrolyte conductivity as compared to solid phase conductivity, most of the polarization loss occurs in a region close to the electrolyte matrix. Most of the material within the center of the electrode does not take part in the electrochemical reaction. This leads to low active material utilization within the electrode. Both low electrode and electrolytic conductivity lead to very poor reaction rate distribution across the electrode.

Increase in reaction rate as exemplified by the exchange current density leads to decrease in polarization losses. Further, with increase in i_0^0 the polarization loss increases linearly with increasing applied loads. However, at low values of i_0^0 the polarization loss increases asymptotically and reaches a plateau with increase in current.

The amount of active material utilized also varies with exchange current density. At high values of i_0^0 (> 10 mA/cm^2), irrespective of the applied load most of the reaction takes place in a small part of the electrode near the electrolyte matrix and hence only 5% of the electrode is utilized. For small i_0^0 values the reaction rate is slow and hence this allows sufficient time for dissolved O_2 and CO_2 to reach the active solid interface and react. The slow reaction rate also

allows the reaction to take place much deeper within the electrode as compared to at high reaction rates. Both these factors contribute to the higher utilization observed for low i_o values. Changes in both gas phase and liquid phase diffusion coefficient do not have a significant effect on the polarization characteristics. In general, in the polarization curve a downward bending effect is observed due to kinetic limitations and an upward bending effect due to mass transfer limitations. Under normal operating conditions mass transfer is not rate limiting and the electrode is generally under mixed control.

The diffusion coefficients, electrolyte conductivity and the exchange current density are all affected by changes in temperature. All of them have an Arrhenius form of dependency on temperature. The activation energy and the frequency factor for each of these parameters have been estimated by fitting the model to experimental data of $LiNiCoO_2$ at different temperatures. Using these fitted parameters the performance of NiO and $LiCoO_2$ cathodes has been studied. Exchange current density for different materials was obtained by fitting the model to the experimental polarization data. Hence, apart from qualitative analysis of the cathode behavior, the model can be used to extract critical thermodynamic, kinetic and transport parameters from polarization data.

A key parameter whose effect on the behavior of the electrode has not been considered is electrolyte filling. Increasing the amount of electrolyte within the MCFC cathode increases the conductivity but reduces the mass transfer rate. Simulations were run by increasing $e^{(l)}$ and decreasing $e^{(g)}$ to account for the increase in electrolyte fill. Results from our model show that the polarization drops with increasing electrolyte filling. There was no optimum as seen experimentally. The model simulations were obtained by keeping all parameters except the porosities constant. Any modifications to the electrolyte content will change the interfacial surface areas ($a^{(sl)}$ and $a^{(gl)}$), which has not been accounted for in these simulations. Mercury porosimetry yields information on the active surface areas corresponding to micropores and macropores and also the liquid and gas porosity. Assuming that the micropores are flooded with electrolyte and macropores with gas, we can determine values for $a^{(sl)}$ and $a^{(gl)}$. These two parameters along with the porosities can be input into the model to determine the polarization behavior. In future, we plan to extend the homogeneous model to account for electrolyte filling by using data from mercury porosimetry.

74

We also developed a three phase homogeneous model based on volume averaging to analyze the performance of the full molten carbonate fuel cell. Relevant results of this model are summarized.

Most of the potential drop in the cell is due to ohmic resistances especially in the matrix. The drop in the cathode and the matrix becomes comparable at high current densities, since at high current densities the concentration polarization in the electrodes increases. The drop in the matrix is confirmed by the huge drop in the liquid phase potentials in the matrix. Concentration polarization effects become important at higher current densities. Concentration polarization exists in the cathode but not in the matrix since there is no gas crossover in the matrix. Hence it is important to take into account the effects of mass transfer while modeling the system.

Matrix thickness plays a critical role in determining cell performance. Reducing the thickness improves the performance but reduces the life of the fuel cell. Hence a compromise must be made between these two opposing phenomena while choosing the separator thickness. The local current density, which determines the reaction rate in the cathode and anode is nonuniform across the cell. This nonuniformity increases as the applied current density increases indicating that parts of the anode and cathode are not completely utilized. The state of art anode electrode parameters – exchange current density and the electrode conductivity are not the limiting factors for cell performance. However, electrolyte conductivity and cathode kinetics are a limiting factor.

In MCFC the cell potential varies linearly with the applied current density because the activation polarization observed in low temperature fuel cells at low current densities vanishes in high temperature cells. The maximum power density does not necessarily correspond to optimum power density, as the heat generation at such current densities is very high and is undesirable for the fuel cell operation.

REFERENCES

[1]   A. J. Appleby and F. R. Foulkes, Fuel Cells – Hand Book, Von Nostrand Reinhold, New York (1989).

[2]   K. Joon, *J. Power Sources*, **71,** 12 (1998).

[3]   J. R. Selman, Assessment of research needs for advanced fuel cells by the DOE advanced fuel cell working group (AFCWG), S.S. Penner, Editor, Permagon Press, New York (1984).

[4]   T. G. Benamin, E. L. Camara and L. G. Marianowski, Handbook of Fuel Cell Performance, Contract no. EC-77C-03-1545, Chicago, IL, (1980).

[5]   L. Christner, L. Paetsch, P.Patel and M. Farooque, Scale-up of internal reforming molten carbonate fuel cells. Proceedings of the 1988 Fuel Cell Seminar, Long Beach, CA 403, (1988).

[6]   K. Tanimoto, Y. Miyazaki, M. Yanagida, S. Tanase, T. Kojima, N. Ohtori, H. Okuyama, T. Kodama, *Denki Kagaku*, **59**(7), 619 (1991).

[7]   K. Tanimoto, Y. Miyazaki, M. Yanagida, T. Kojima, N. Ohtori, T. Kodama, *Denki Kagaku*, **63**(4), 316 (1995).

[8]   L. Plomp, E.F. Sitters, C. Vessies, F. C. Eckes, *J. Electrochem. Soc.*, **138**(2) (1991) 629.

[9]   L. Giorgi, M. Carewska, S. Scaccia, E. Simonetti, F. Zarzana, *Denki Kagaku*, **64**(6), 482 (1996).

[10]   C. Lagergren, A. Lundblad, B. Bergman, *J. Electrochem. Soc.*, **141**(11), 2959 (1994).

[11]   K. Nakagawa, S.Kihara and T. Kobayashi, in Proceedings of the 11th *International Corrosion Congress,* Florence, **4,** 4.37 (1990).

[12]   R A. Donado, L.G. Marionowski, H. C. Maru, and J. R. Selman, *J. Electrochem. Soc.*, **131**, 2541 (1984).

[13]   C. Yuh, R. Johnson, M. Farooque and H. Maru, *J. Power Sources*, **56,** 1 (1985).

[14]   K. Nakagawa, S. Kihara, and S. Ito, *Corrosion Engineering*, **37,** 411 (1988).

[15]   K. Tanimoto, Y. Miyazaki, M. Yanagida, S. Tanase, T. Kojima, N. Ohtori and T. Kodama, *Denki Kagaku*, **62**, 445 (1994).

[16]   K. Hiyama, T. Yoshioka, T. Yoshida, and Y. Fukui, *Corrosion Engineering*, **39,** 455 (1990).

[17]   M. Sakai, N. Ohta, M. Asano, and N. Iggata, *Corrosion Engineering*, **45,** 231 (1966).

[18] T. Shimada, N. Ariga, J. Sakai, and K. Masamura, Trans. Material. Res. Soc., Japan, **18A,** 569 (1994).

[19] H. Matsuyama, T. Nishina, and I. Uchida, in International symposium on Molten Salt Chemistry and Technology, M.-L. Saboungi, H. Kojima, J. Duruz and D. Shores, Eds., **PV 93-9,** The Electrochemical Society Proceeding Series, Pennington, NJ, USA 436 (1993).

[20] M. Keijzer, Ph.D. Thesis, Delft University, Netherlands (1998).

[21] M. Okuyama, M. Ushioda, and Y. Itoi, *Denki Kagaku*, **60,** 508 (1992).

[22] J. P. T. Vossen, R. C. Makkus, and J. H. W. de Wit, *J. Electrochem. Soc.*, **143,** 66 (1996).

[23] H. J. Davis, and D. R. Kinnibrugh, *J. Electrochem. Soc.*, **117,** 392 (1970).

[24] R. B. Swaroop, J. W. Sim, and K. Kinoshita, *J. Electrochem. Soc.*, **125,** 1799 (1978).

[25] J. P. T. Vossen, Ph.D. Thesis, Delft University, Netherlands (1994).

[26] A. Durairajan, B. Haran, B. Popov and R. White, *J. Power Sources*, **83,** 114 (1999).

[27] G. Wilemski, *J. Electrochem. Soc.*, **130**, 117 (1983).

[28] C. Y. Yuh and J. R. Selman, *J. Electrochem. Soc.*, **131**, 2062 (1984).

[29] J. A. Prins-Jansen, K. Hemmes and J. H. W de Wit, *Electrochem. Acta*, **40**, 3585 (1997).

[30] H. R. Kunz and L. A. Murphy, *J. Electrochem. Soc.*, **135**, 1124 (1988).

[31] E. Fontes, C. Lagergren and D. Simonsson, *Electrochem. Acta*, **38**, 2669 (1993).

[32] P.S. Christensen, H. Livbjerg, *Chem. Eng. Sci.*, 47, 2933 (1992).

[33] E. Fontes, M. Fontes and D. Simonsson, *Electrochem. Acta*, **141**, 1 (1996).

[34] J. A. Prins-Jansen, J. D. Fehribach, K. Hemmes and J. H. W. de Wit, *J. Electrochem. Soc.*, **143**, 1617 (1996).

[35] G. L. Lee, J. R. Selman and L. Pomp, *J. Electrochem. Soc.*, **140**, 390 (1993).

[36] E. Fontes, C. Lagergren, D. Simonsson, *J. Electroanal. Chem.*, **432**, 121 (1997).

[37] E. Fontes, M. Fontes, G. Lindbergh, D. Simonsson, *J. Appl. Electrochem.*, 27, 1149 (1997).

[38] P. de Vidts and R. E. White, *J. Electrochem. Soc.*, **144**, 1343 (1997).

[39] P. de Vidts, "Mathematical modeling of a nickel/hydrogen cell", Ph.D. Thesis, Texas A & M University, Texas, (1995).

[40] L.A.H. Machielse, Simple model for estimation of isothermal fuel cell performance, *Proc. Modeling on Batteries and Fuel cells*, **91-10**, 166 (1991).

[41]   F. Standaert, K. Hemmes, N. Woudstra, *J. Power Sources,* **63**, 221 (1996).

[42]   A. Durairajan, H. Colon, B. Haran, R. E. White and B. N. Popov, *J. Power Sources,* **104** (2), 157-168 (2002).

[43]   J. C. Slattery, Advanced Transport Phenomena, Cambridge University Press, New York, (1999).

[44]   M. Kaviany, Principles of Heat Transfer in Porous Media, Springer-Verlag, New York, (1991).

[45]   J. Prins-Jansen, "Cathodes in Molten Carbonate Fuel Cells", Ph.D. Thesis, Delft University of Technology, Netherlands, (1996).

[46]   E. L. Cussler, Diffusion, Mass Transfer in Fluid Systems, Cambridge University Press, New York, (1984).

[47]   S.H. Lu and J.R. Selman, *J. Electrochem. Soc.*, **136**, 1068 (1989).

[48]   P. L. Mangonon, Principles of Materials Selection for Engineering Design, Prentice Hall, New Jersey, USA 173 (1999).

[49]   K. Tanimoto, Y. Miyazaki, M. Yanagida, S. Tanase, T. Kojima, N. Ohtori, H. Okuyama, T. Kodama, *Denki Kagaku*, **59**(7), 619 (1991).

[50]   K. Ota, S. Mitsushima, S. Katao, S. Asano, H. Yoshitake, and N. Kamiya, *J. Electrochem. Soc.*, **139**(3), 667 (1992).

[51]   X. Zhang, P. Capobianco, A. Torazza, and B. Passalacqua, *Electrochemistry*, **67**(6) (1999).

[52]   J. B. J. Veldhuis, F. C. Eckes, and L. Plomp, *J. Electrochem. Soc.*, **139** (1), L6 (1992).

[53]   K. Ota, Y. Takeishi, S. Shibata, H. Yoshitake, and N. Kamiya, *J. Electrochem. Soc.*, **142**(10), 3322 (1995).

[54]   P Tomczyk, H Sato, K Yamada, T Nishina and I. Uchida, *J. Electroanal. Chem.*, **391,** 133 (1995).

[55]   B Y Yang and K Y Kim, *Electrochim. Acta*, **43,** 3343 (1998).

[56]   C. Y. Yuh and J. R. Selman, *J. Electrochem. Soc.*, **138**(12), 3642 (1991).

[57]   C. Y. Yuh and J. R. Selman, *J. Electrochem. Soc.*, **138**(12), 3649 (1991).

[58]   R. D. Shannon, G. T. Prewitt, *Acta Crystallogr.*, Sect. B 25, 925 (1969).

[59]   F. J. Perez, D. Duday, M. P. Hierro, C. Gomez, M. Romero, M. T. Casais, J. A. Alonso, M. J. Martinez and L. Daza, *J.Power Sources,* 86, 309 (2000).

[60]   *Assessment of Research Needs for Advanced Fuel Cells* by DOE advanced Fuel Cell Working Group, Ed. S. S. Penner, Pergamon Press, New York (1985).

[61]   J. S. Newman and C. W. Tobias, *J. Electrochem. Soc.*, **109**, 1183 (1962).

[62]   C. Lagergren and D. Simonsson, *J. Electrochem. Soc.*, **144**, 3813 (1997).

[63]   J. H. Hirschenhofer, D. B. Stauffer, R. R. Engleman, and M. G. Klett, Fuel Cell Handbook, 4-5 (1998).

[64]   N. Subramanian, B. S. Haran, P. Ganesan, R. E. White and B. N. Popov, "Analysis of Molten Carbonate Fuel Cell Performance Using a Three Phase Homogeneous Model", Accepted for publication in *J. Electrochem. Soc.*, April 2002.

[65]   J. Soler, T. Gonzalez, M. J. Escudero, T. Rodrigo, L. Daza, *J. Power Sources*, **4650**, 1 (2002).

[66]   M. Doyle and J. Newman, A. S. Gozdz, C. N. Schmutz and J-M Tarascon, *J. Electrochem. Soc.*, **143**, 1890 (1996).

[67]   C. Y. Yuh,"Potential Relaxation and AC Impedance of Porous Electrodes', Ph.D. Thesis, Illinois Institute of Technology, Chicago, Illinois, (1985).

[68]   C. Y. Yuh and J. R. Selman, *AIChE J.*, **34**, 1949 (1998).

LIST OF ACRONYMS AND ABBREVIATIONS

$\langle c_i \rangle^{(l)}$ Concentration of species 'i' in the liquid phase, mol/cm^3

$\langle c_i \rangle^{(g)}$ Concentration of species 'i' in the gas phase, mol/cm^3

$\langle c \rangle^{(g)}$ Total concentration in the gas phase, mol/cm^3

$\langle CO_2 \rangle^g$ Volume averaged concentration of CO_2 in the gas phase, mol/cm^3

$\langle O_2 \rangle^g$ Volume averaged concentration of O_2 in the gas phase, mol/cm^3

$\langle H_2 \rangle^g$ Volume averaged concentration of H_2 in the gas phase, mol/cm^3

$\langle CO_2 \rangle^l$ Volume averaged concentration of CO_2 in the liquid phase, mol/cm^3

$\langle O_2 \rangle^l$ Volume averaged concentration of O_2 in the liquid phase, mol/cm^3

$\langle H_2 \rangle^l$ Volume averaged concentration of H_2 in the liquid phase, mol/cm^3

$\langle CO_2 \rangle^{(g)*}$ Bulk concentration of CO_2 in the gas phase, mol/cm^3

$\langle O_2 \rangle^{(g)*}$ Bulk concentration of O_2 in the gas phase, mol/cm^3

$\langle H_2 \rangle^{(g)*}$ Bulk concentration of H_2 in the gas phase, mol/cm^3

$\langle CO_2 \rangle^{(l)*}$ Bulk concentration of CO_2 in the liquid phase, mol/cm^3

$\langle O_2 \rangle^{(l)*}$ Bulk concentration of O_2 in the liquid phase, mol/cm^3

$\langle H_2 \rangle^{(l)*}$ Bulk concentration of H_2 in the liquid phase, mol/cm^3

$a_k^{(lg)}$ Specific surface area at the gas/liquid interface in the electrode k, cm^2/cm^3

$a_k^{(sl)}$ Specific surface area at the liquid/solid interface in the electrode k, cm^2/cm^3

b Correction for diffusion coefficient

c Total concentration, mol/cm^3

$c_{(i)}$ Concentration of species i, mol/cm^3

d Correction for conductivity in the electrodes

d_s Correction for conductivity in the matrix

$D_{i,k}^{(g)}$	Diffusion coefficient of species 'i' in electrode k in the gas phase, cm^2/s
$D_{i,k}^{(l)}$	Diffusion coefficient of species 'i' in electrode k in the liquid phase, cm^2/s
$D_{(AB)}$	Diffusion coefficient of A into B, cm^2/s
$D_{CO_2}^{(g)}$	Diffusion coefficient of CO_2 in the gas phase, cm^2/s
$D_{O_2}^{(g)}$	Diffusion coefficient of O_2 in the gas phase, cm^2/s
$D_{CO_2}^{(l)}$	Diffusion coefficient of CO_2 in the liquid phase, cm^2/s
$D_{O_2}^{(l)}$	Diffusion coefficient of O_2 in the liquid phase, cm^2/s
E_{eqc}	Equilibrium potential of the cathode, V
E_{eqa}	Equilibrium potential of the anode, V
I	Applied current, A/cm^2
$\overline{F}_i^{(lg)}$	Average flux of species 'i' from the liquid phase into the gas phase, $mol/cm^3 s$
i_0^0	Concentration independent exchange current density, $A/cm2$
i_0	Concentration dependent exchange current density, $A/cm2$
$i^{(l)}$	Current density in the electrolyte, A/cm^2
$i^{(s)}$	Current density in the solid, A/cm^2
$\overline{i}^{(l)}$ (or i_2)	Volume averaged current density in the electrolyte, A/cm^2
$\overline{i}^{(s)}$	Volume averaged current density in the solid, A/cm^2
$J_{(i)}^{\diamond}$	Molar flux of species i relative to molar average velocity, $mol/cm^2 s$
$j_{(i)}^{\diamond}$	Mass flux of species i relative to molar average velocity, $mol/cm^2 s$
$j_{(i)}$	Mass flux of species i relative to mass average velocity, $mol/cm^2 s$
$i_{0,k}^0$	Concentration independent exchange current density in the electrode k, $A/cm2$
$i_{0,k}$	Concentration dependent exchange current density in the electrode k, $A/cm2$
$i^{(l)}$	Current density in the electrolyte, A/cm^2
$i^{(s)}$	Current density in the solid, A/cm^2

$\langle j_k \rangle^{(sl)}$	Average local current density due to reaction occurring in electrode k at the liquid/solid interface, A/cm^2
$K_{e,i,k}$	Equilibrium constant relating the concentration of species 'i' in the liquid and gas phase in electrode k, $\dfrac{\langle c^*_{CO_2} \rangle^{(l)}}{\langle c^*_{CO_2} \rangle^{(g)}}$
$k_{i,k}^{(lg)}$	Rate constant of molar flux of species 'i' between the liquid and gas phase in electrode k, cm/s
K_{e,CO_2}	Equilibrium constant relating the concentration of CO_2 in the liquid and gas phase, $\dfrac{\langle c^*_{CO_2} \rangle^{(l)}}{\langle c^*_{CO_2} \rangle^{(g)}}$
K_{e,O_2}	Equilibrium constant relating the concentration of O_2 in the liquid and gas phase, $\dfrac{\langle c^*_{O_2} \rangle^{(l)}}{\langle c^*_{O_2} \rangle^{(g)}}$
$k_{CO_2}^{(lg)}$	Rate constant of molar flux of CO_2 between the liquid and gas phase cm/s
$k_{O_2}^{(lg)}$	Rate constant of molar flux of O_2 between the liquid and gas phase cm/s
L	Thickness of the fuel cell, cm
$M_{(i)}$	Molecular weight of species i, gm/mol
N_i	Molar flux of species i with respect to a fixed frame of reference, mol/cm^{2}s
$\overline{N}_i^g$	Volume averaged molar flux of species i in the gas phase, mol/cm^{2}s
$\overline{N}_i^l$	Volume averaged molar flux of species i in the liquid phase, mol/cm^{2}s
N_i	Molar flux of species i with respect to a fixed frame of reference, mol/cm^{2}s
$N_i^{(k)}$	Molar flux of species 'i' in phase 'k', mol/cm^{2}s
n_k	Number of electrons exchanged through reaction 'k'
$n_{(lg)}$	Unit normal vector to the surface $S_{(lg)}$ pointing out of the liquid into the gas phase
$n_{(ls)}$	Unit normal vector to the surface $S_{(ls)}$ pointing out of the liquid into the gas phase
$p^*_{CO_2}$	Equilibrium partial pressure of CO_2, atm.

$p_{O_2}^*$	Equilibrium partial pressure of O_2, atm.
$p_{H_2}^*$	Equilibrium partial pressure of H_2, atm.
p	Total pressure, atm.
$\overline{R}_i^{ls}$	Average rate of production f species 'i' at the liquid/solid interface, mol/cm^{3}s
$\overline{R}_i^{(gs)}$	Average rate of production f species 'i' at the gas/solid interface, mol/cm^{3}s
$r_i^{(lg)}$	Molar flux of species 'i' from the liquid into the gas phase, mol/cm^{2}s
s_{ik}	Stoichiometry of species 'i' in reaction 'k'
$S_{(lg)}$	Surface that coincides with the liquid/gas interface inside volume V, cm^2
$S_{(ls)}$	Surface that coincides with the liquid/solid interface inside volume V, cm^2
T	Temperature, K
$u_i^{(k)}$	Dimensionless concentration of species 'i' in phase 'k'
V	Volume of porous media, cm^3
$V_{(i)}$	Volume of phase i in the porous media, cm^3
V_{CO_2}	Diffusion volume of CO_2
V_{O_2}	Diffusion volume of O_2
$x_{(i)}$	Mole fraction of species i
x_1	Cathode-matrix interface
x_2	Matrix-anode interface
$\langle f \rangle$	Overpotential, V
$\langle f \rangle^{(l)}$	Liquid phase potential, V
$\langle f \rangle^{(s)}$	Solid phase potential, V
$f^{(k)}$	Potential in phase 'k', V
a_c	Cathodic transfer coefficient
a_a	Anodic transfer coefficient
$a_{c,k}$	Cathodic transfer coefficient of electrode k

$\alpha_{a,k}$	Anodic transfer coefficient of electrode k
$\varepsilon_k^{(g)}$	Gas porosity at electrode k
$\varepsilon_k^{(l)}$	Liquid porosity at electrode k
$\varepsilon_k^{(s)}$	Solid porosity at electrode k
$\varepsilon^{(g)}$	Gas porosity
$\varepsilon^{(l)}$	Liquid porosity
$\varepsilon^{(s)}$	Solid porosity
κ_{app}	Apparent electrolyte conductivity, S/cm $= \kappa\left(\varepsilon^{(l)}\right)^d$
κ	Electrolyte conductivity, S/cm
σ_k	Electrode conductivity of electrode k, S/cm
v	Mass average velocity, cm/s
$v^{\lozenge}$	Molar average velocity, cm/s
k	Electrode
c	Cathode
a	Anode
σ_{app}	Apparent electrode conductivity, S/cm $= \sigma\left(\varepsilon^{(s)}\right)^d$
$\rho_{(i)}$	Density of species i, gm/cm^3
σ	Electrode conductivity, S/cm
l	Liquid phase
g	Gas phase

APPENDIX A – FIGURES AND TABLES
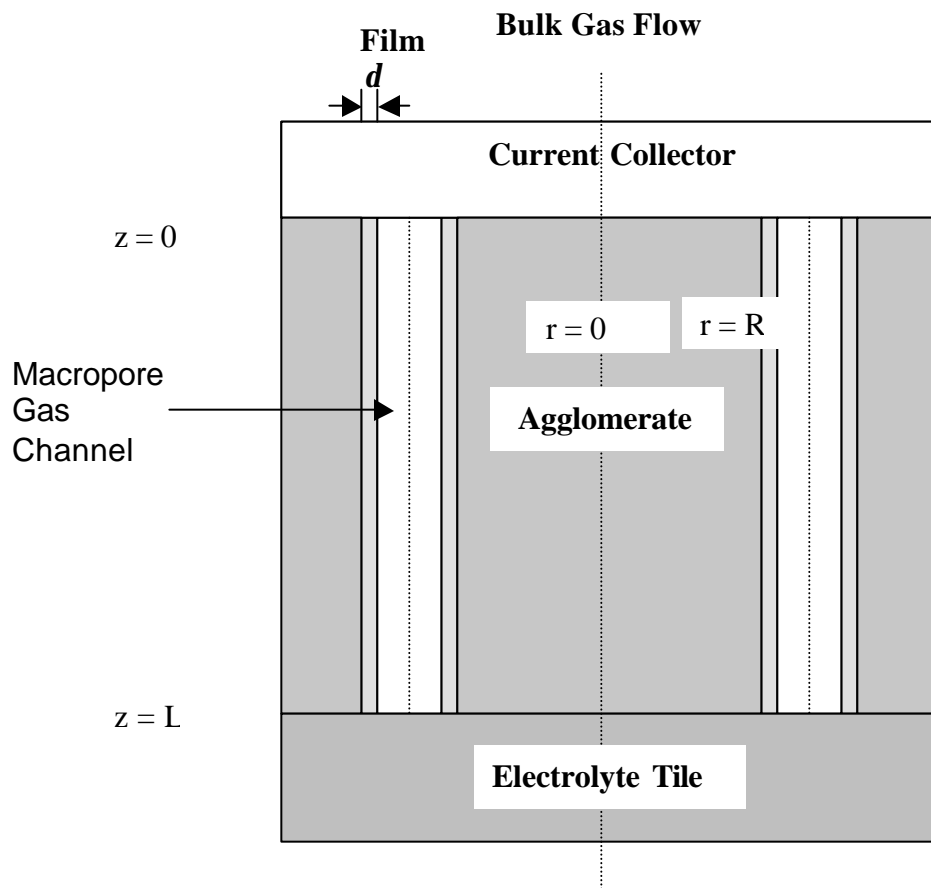
Figure 1. Schematic of the MCFC cell based on the agglomerate model.

Figure 2.   3cm^2 cell used to acquire the experimental data.
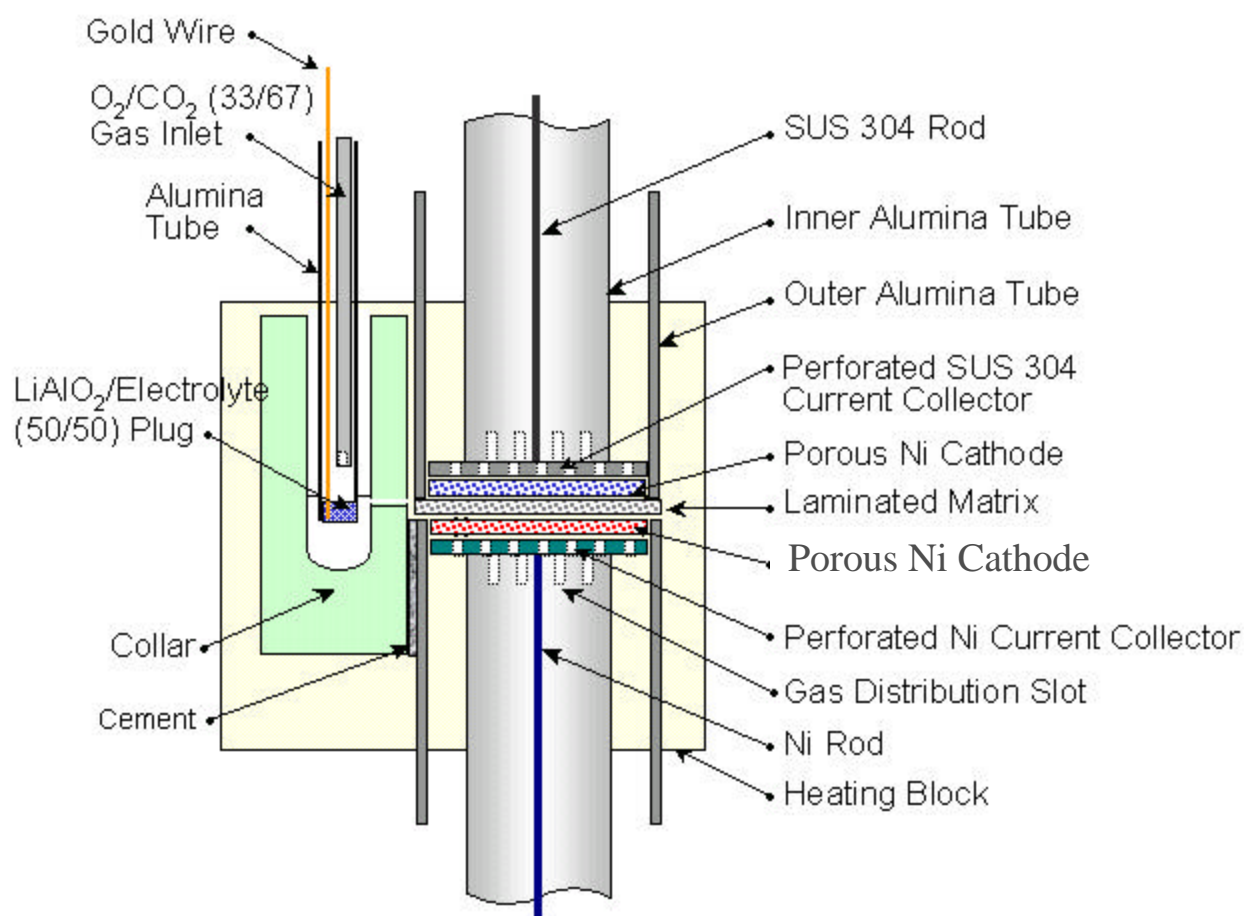
Figure 3. Schematic of the 3cm^2 cell used to acquire the experimental data.
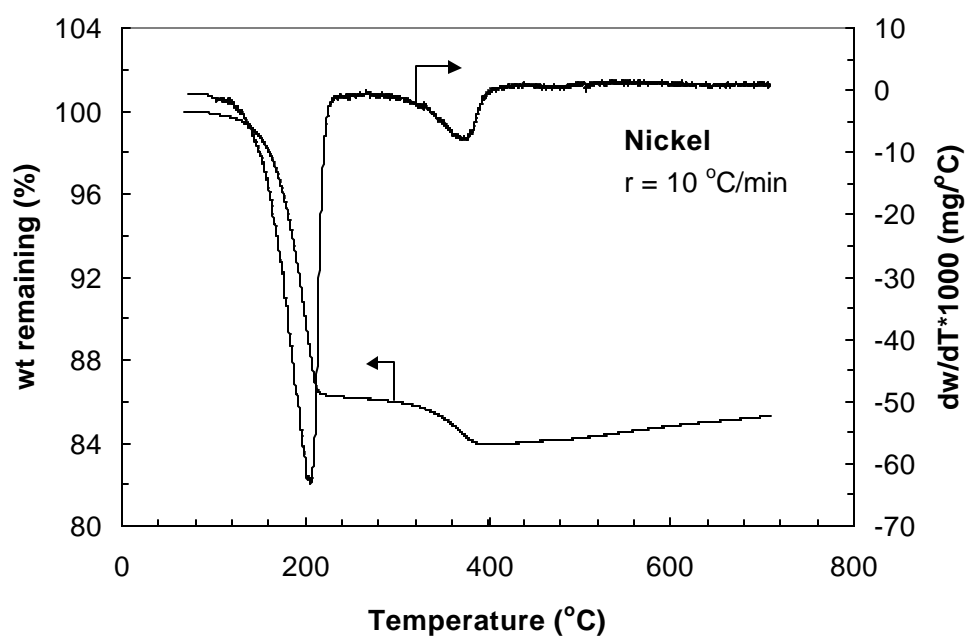
Figure 4. Thermo gravimetric analysis (TGA) of an aqueous nickel tape.

5.7 μm   5.7 μm   5.7 μm

$LiNi_{0.7}Co_{0.3}O_2$ $LiNi_{0.8}Co_{0.2}O_2$ $LiNi_{0.9}Co_{0.1}O_2$
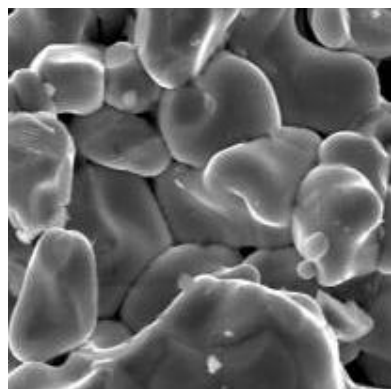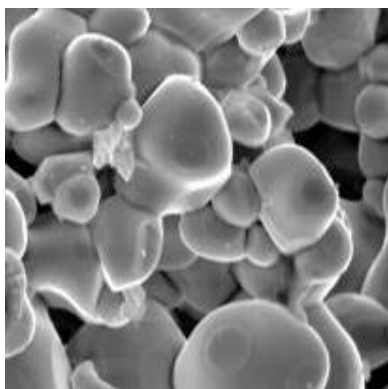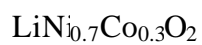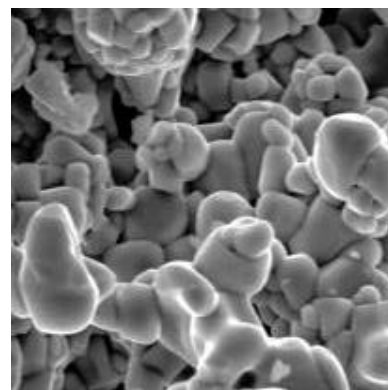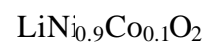
Magnification X2000

Figure 5.   Scanning electron micrographs of synthesized $LiNi_xCo_{1-x}O_2$ with different amounts of cobalt doping (x = 0.1, 0.2 and 0.3).
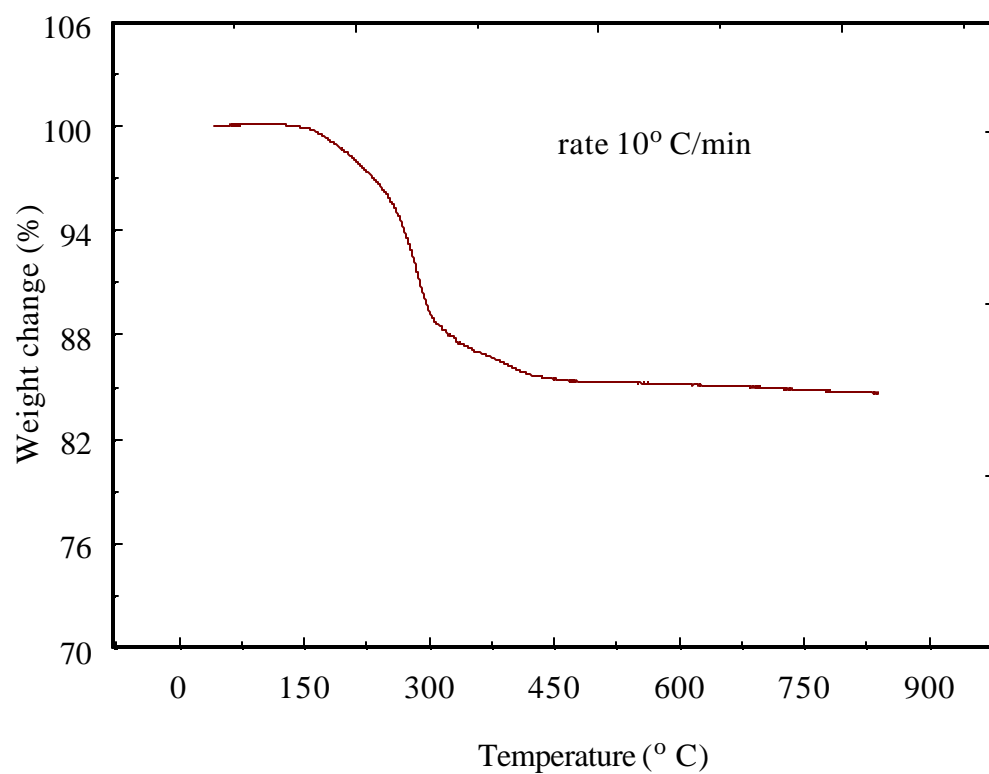
Figure 6. Thermo gravimetric analysis (TGA) of $LiNi_{0.8}Co_{0.2}O_2$ tape obtained by non-aqueous tapecasting.

800 ℃   5.7 μm

850 ℃   5.7 μm

900 ℃   5.7 μm
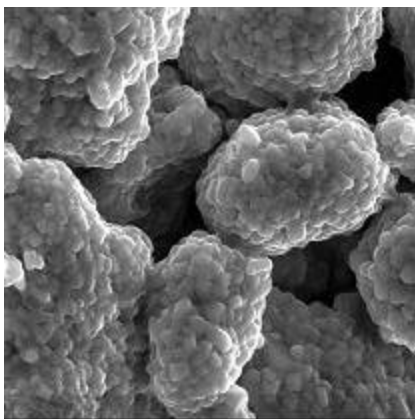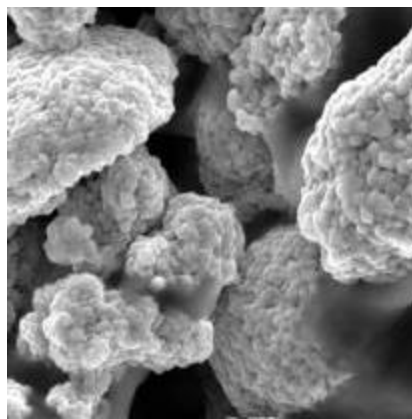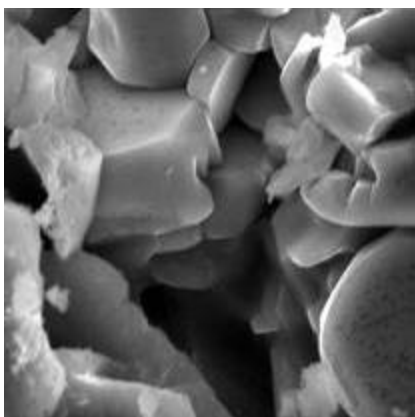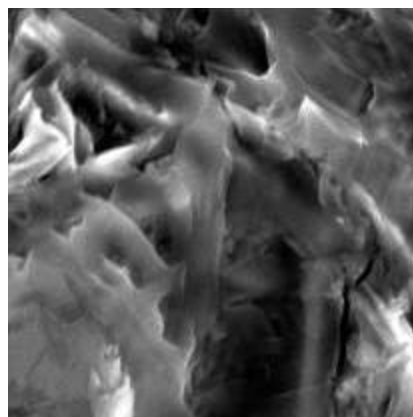
1000 ℃   5.7 μm

Magnification X2000

Figure 7.   SEM pictured of $LiN_{0.8}Co_{0.2}O_2$ electrodes obtained after tapecasting and
                sintering.
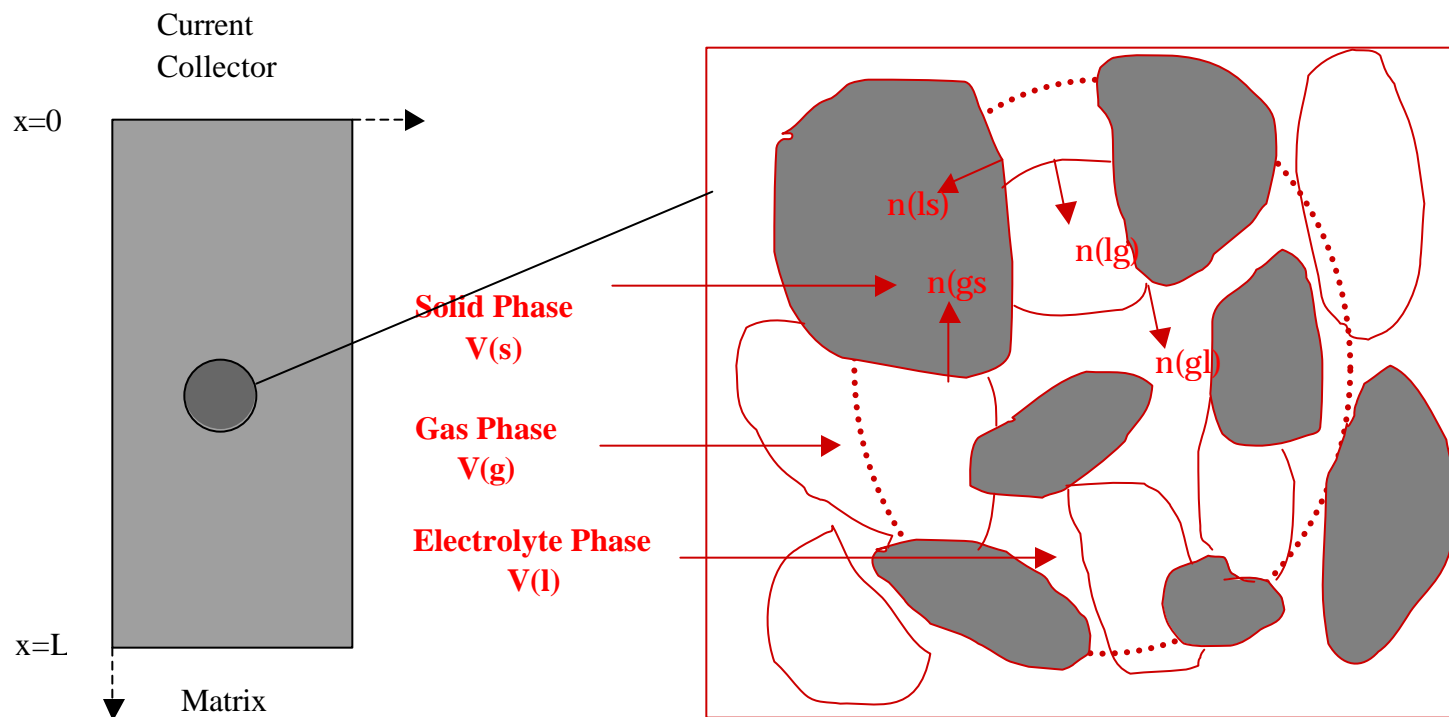
Figure 8. Volume averaging in porous electrode.
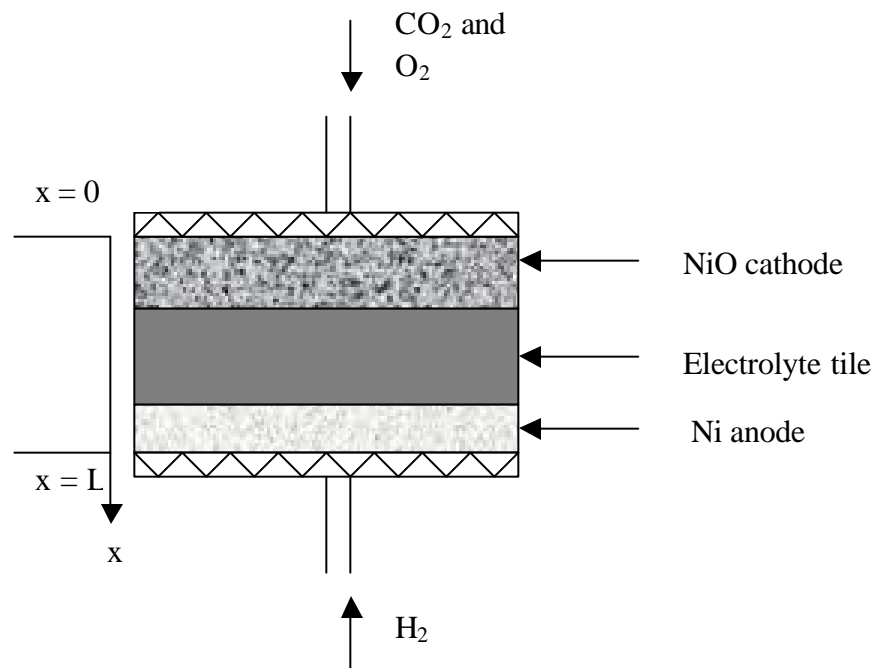
Figure 9. Schematic of MCFC full cell based on the volume averaged model.
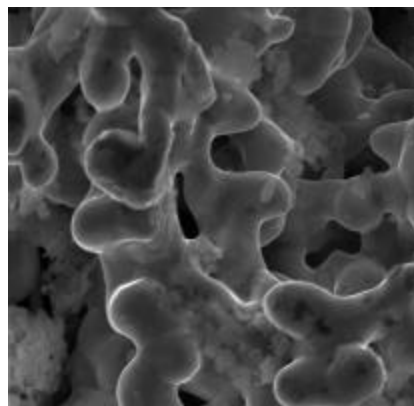
Nickel Electrode Prepared
by Aqueous Tapecasting

Cobalt Encapsulation
Followed by Sintering at
800°C

Cobalt encapsulated tape
after deposition
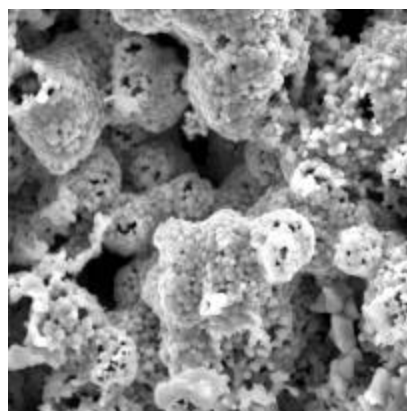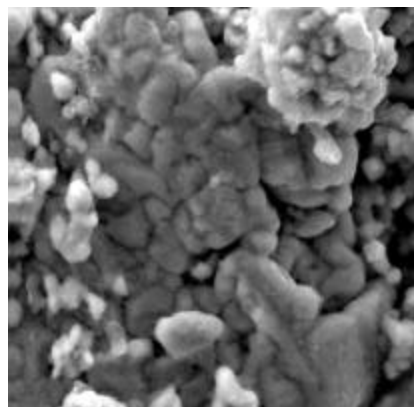
Figure 10. SEM photographs of bare and cobalt microencapsulated nickel electrodes obtained by tape casting and sintering.
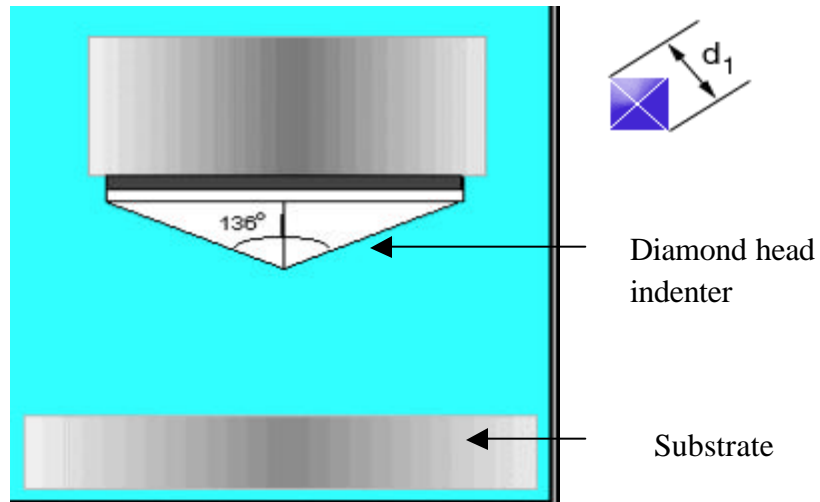
Figure 11. Schematic of a Vickers hardness tester showing the diamond tip indenter with a phase angle of 136°C.
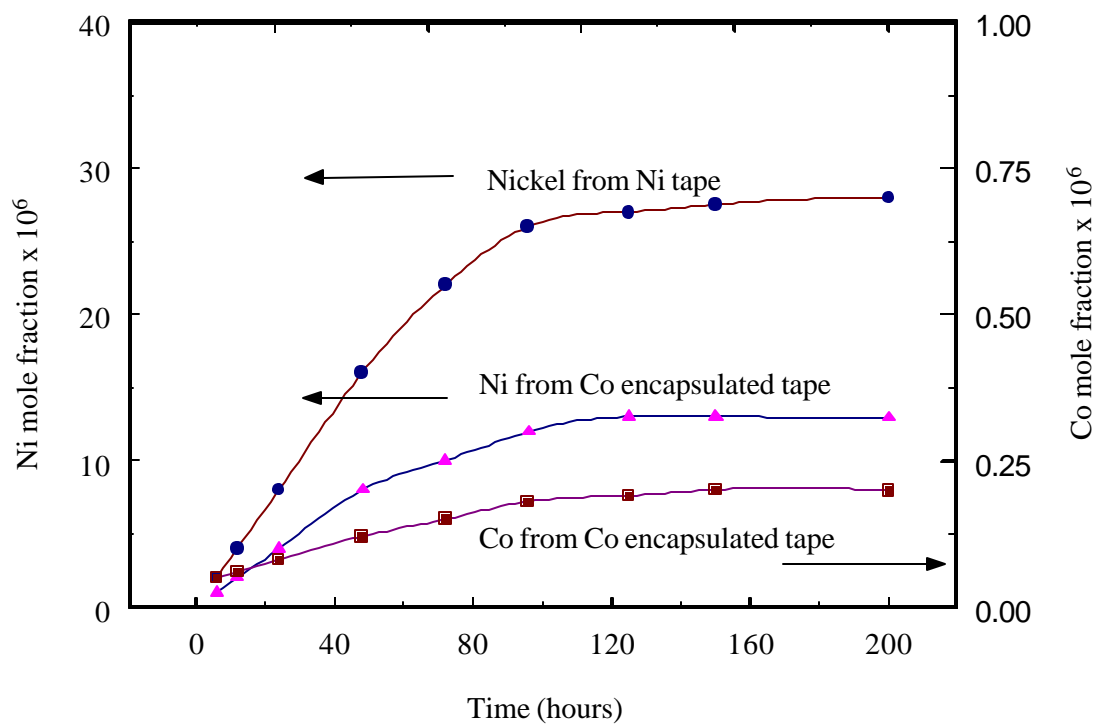
Figure 12. Atomic absorption spectroscopy analysis of dissolved nickel and cobalt in molten carbonate melt.
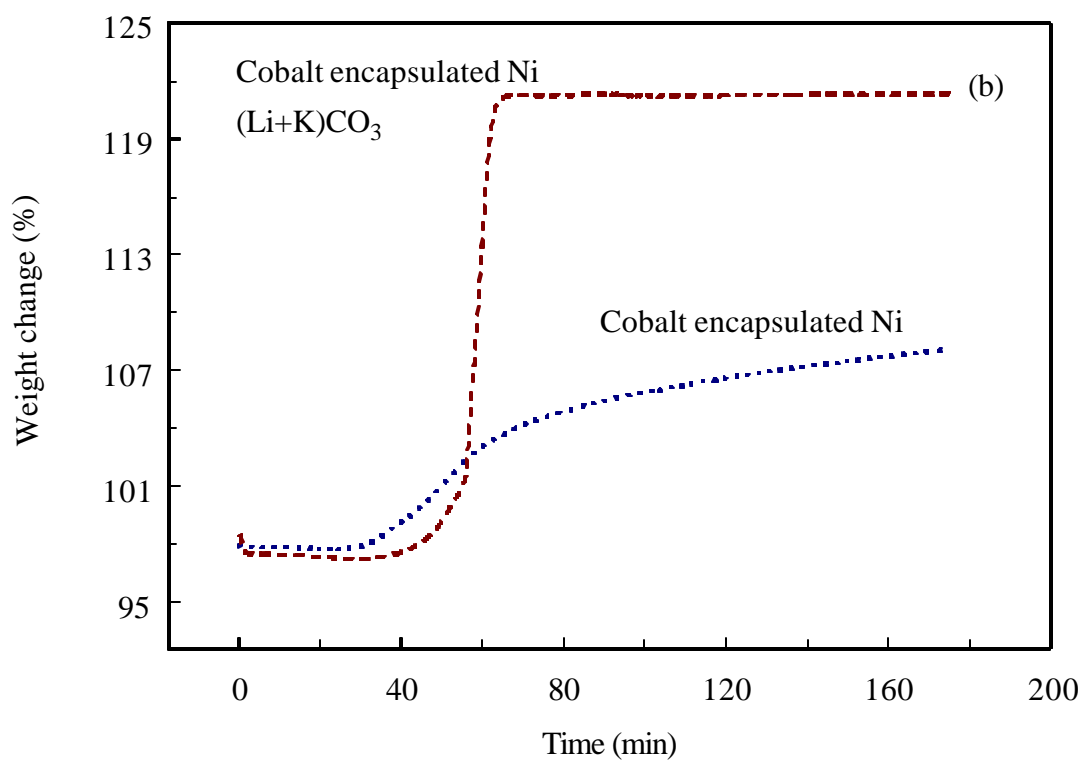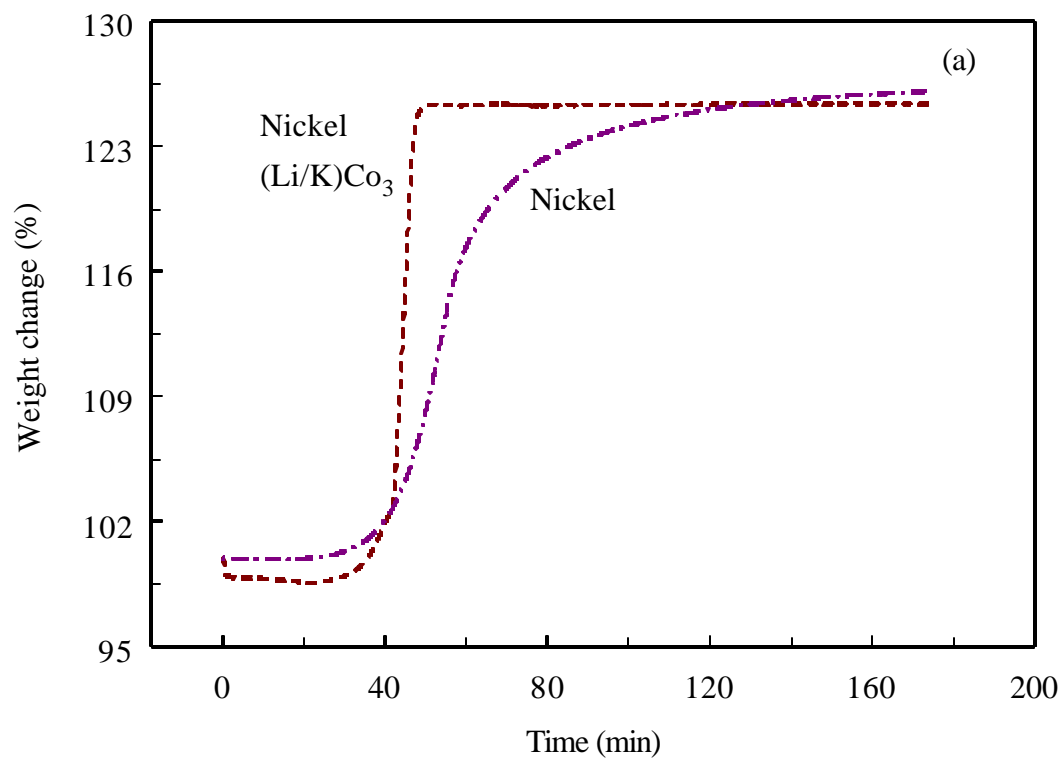
Figure 13. TGA analysis of sintered nickel (a) and cobalt encapsulated nickel (b) tapes under cathode gas conditions in the presence and absence of molten carbonate melt.
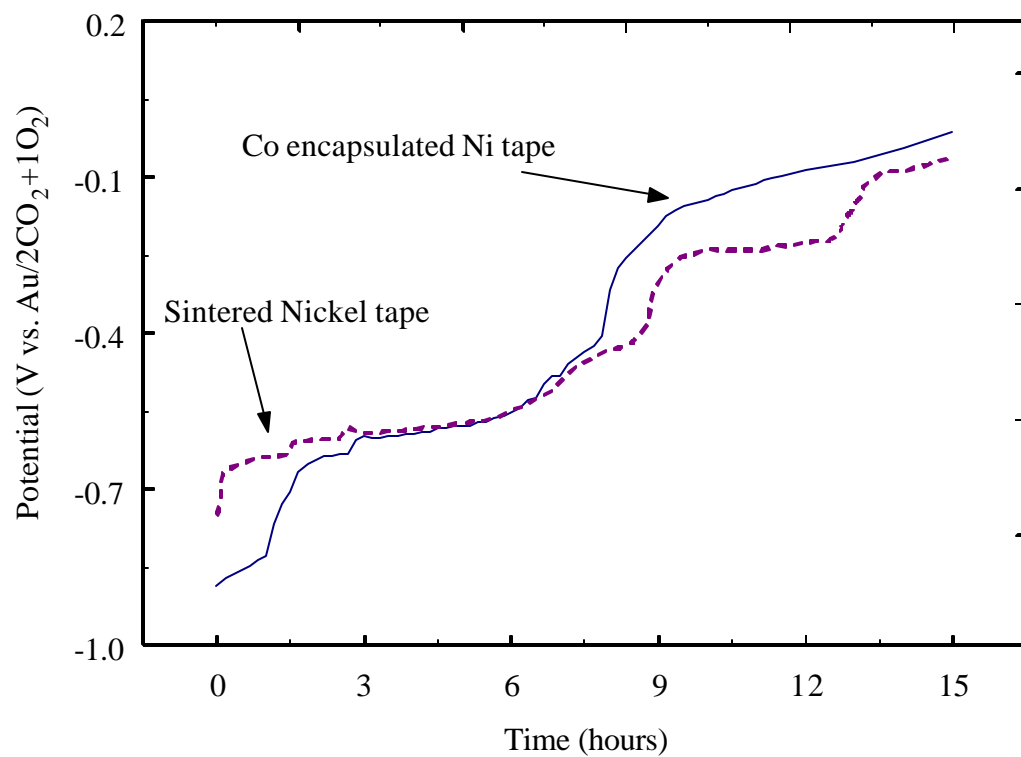
Figure 14. Open circuit potential as a function of time during the *in-situ* oxidation of bare and cobalt encapsulated nickel tapes under cathode gas conditions.
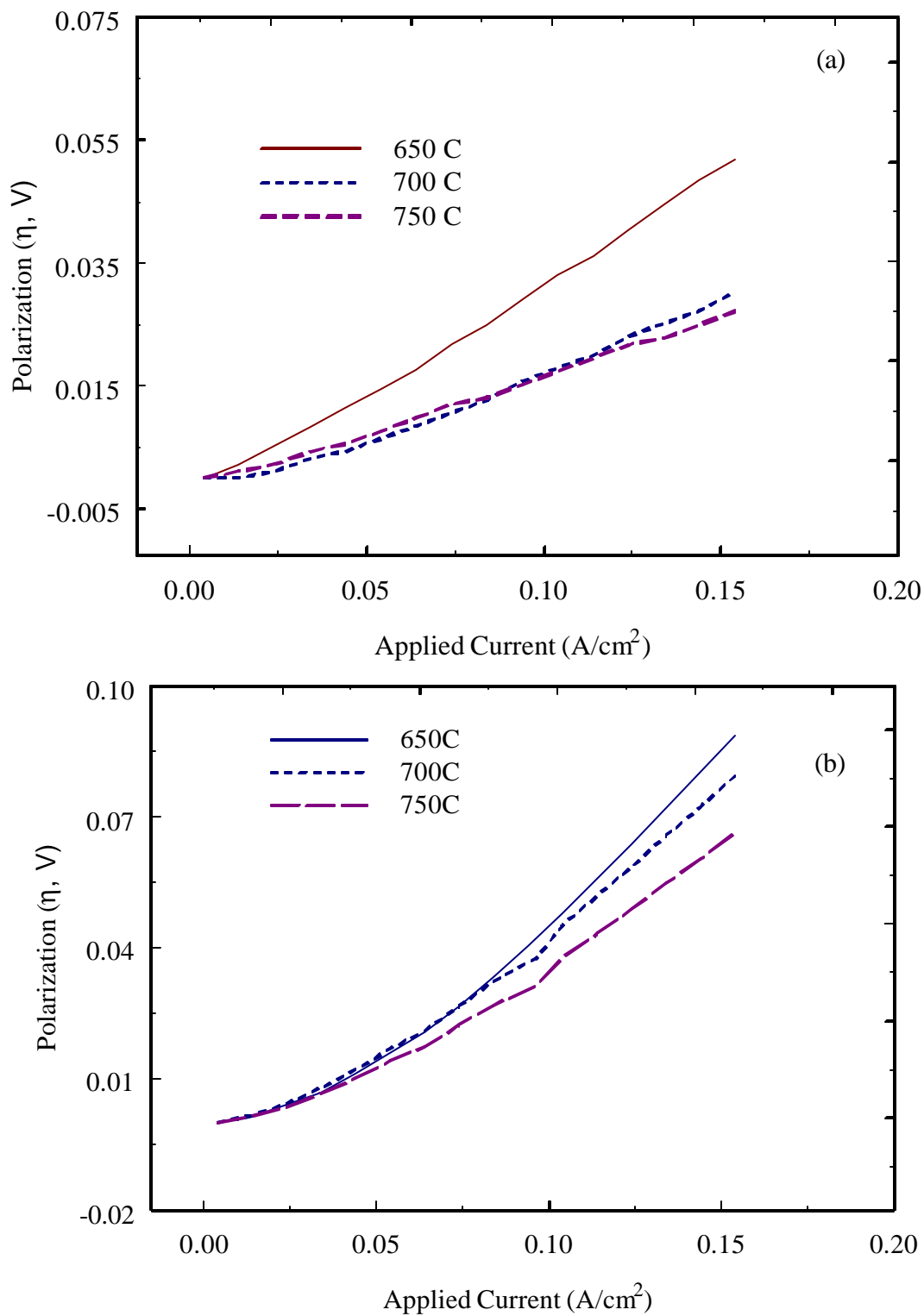
Figure 15. Comparison of cathode polarization behavior at different current loads for bare (a) and cobalt encapsulated nickel (b) cathodes at different temperatures.
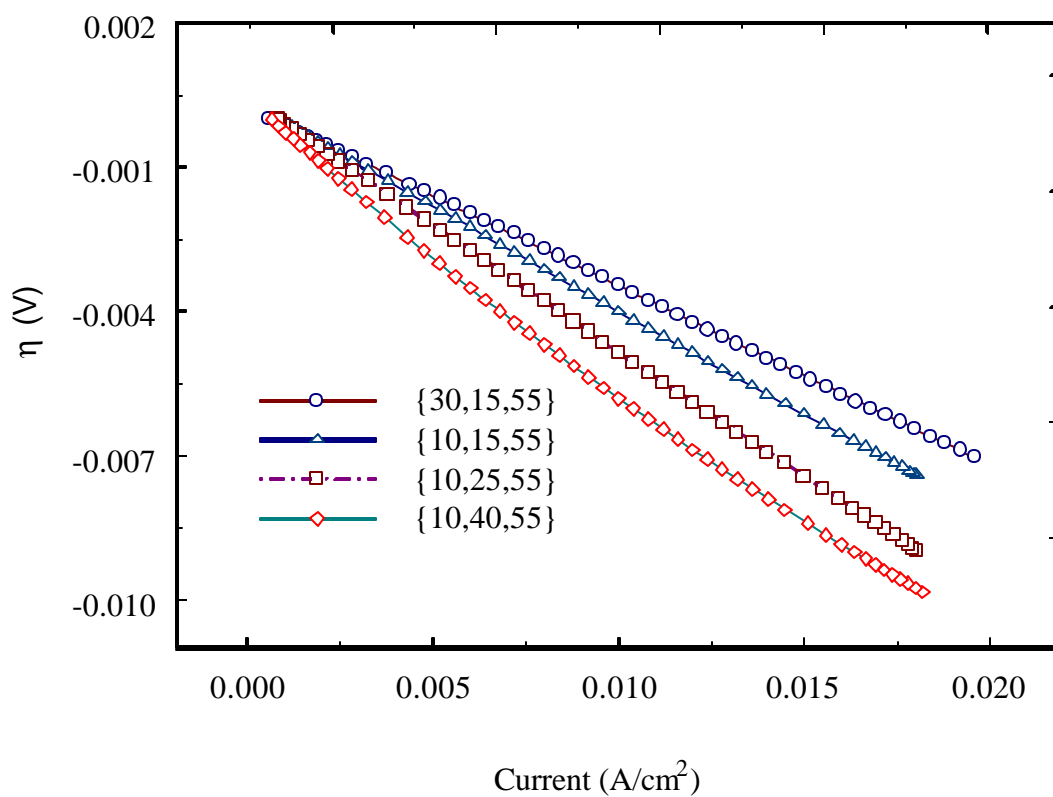
Figure 16. Comparison of i-V plots obtained for CoO-NiO electrodes under different cathode gas and temperature conditions.
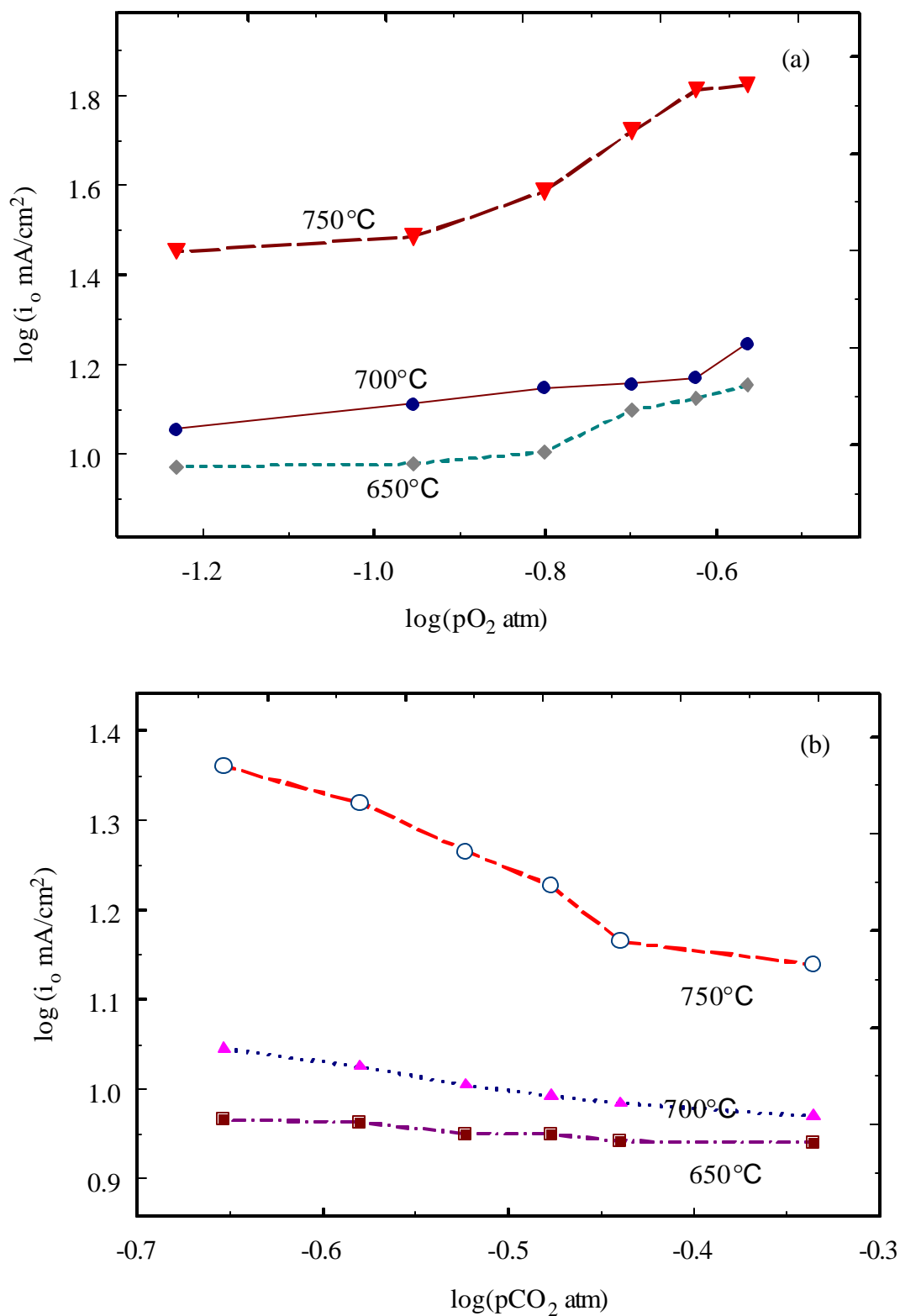
Figure 17. Plot of apparent exchange current density of cathode reaction on cobalt encapsulated nickel as a function of O_2 (a) and CO_2 (b) partial pressures at 650, 700 and 750°C.
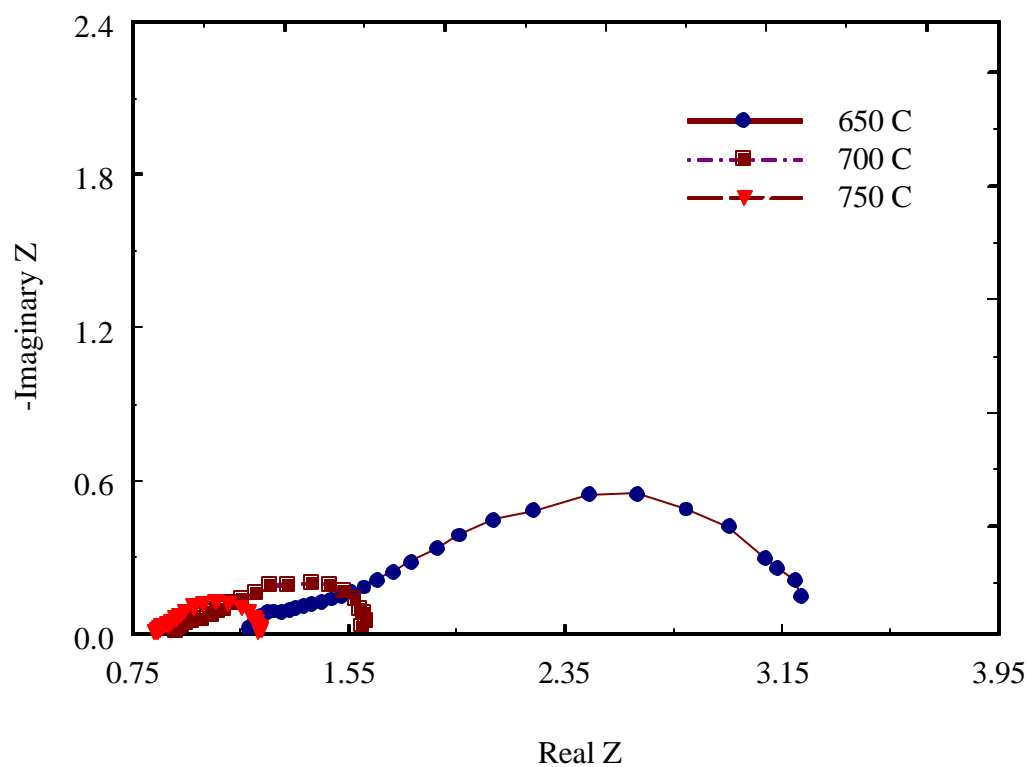
Figure 18. Nyquist plots of impedance response of NiO electrode at different temperatures at a particular gas composition.

103
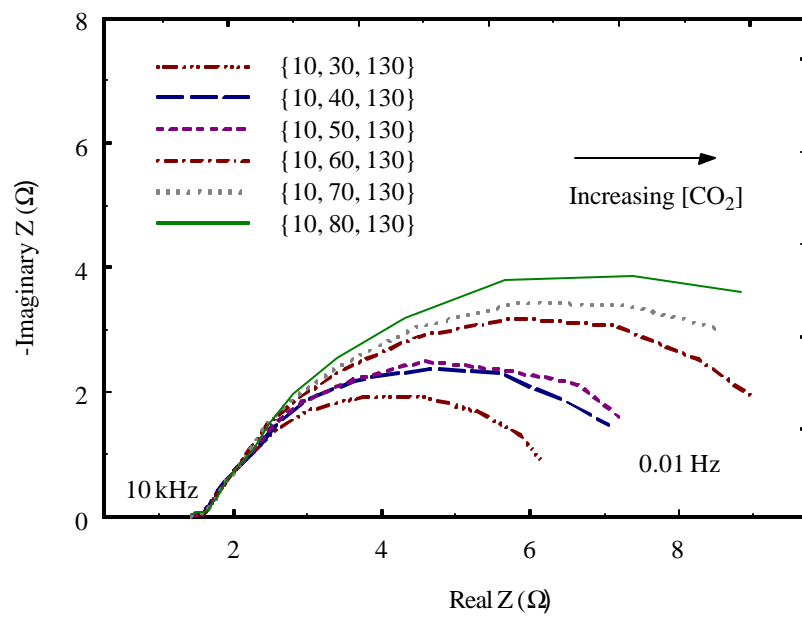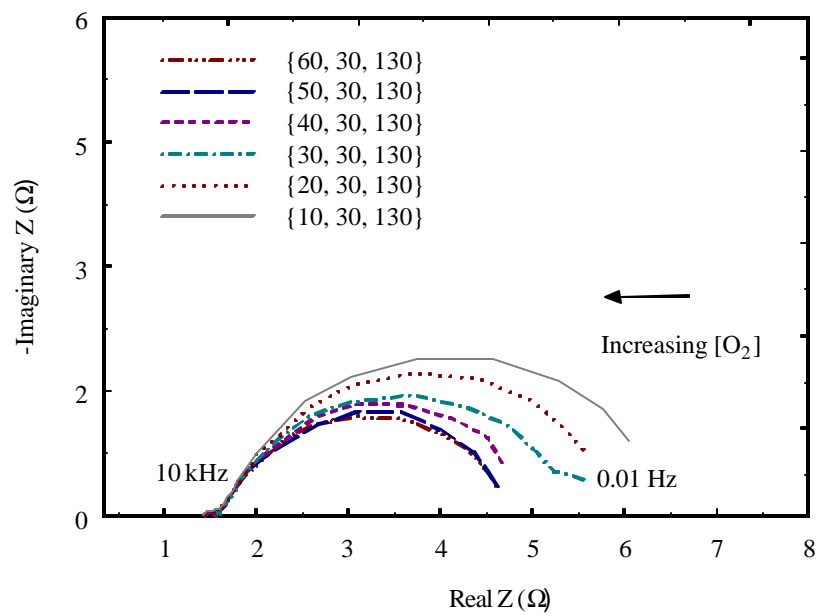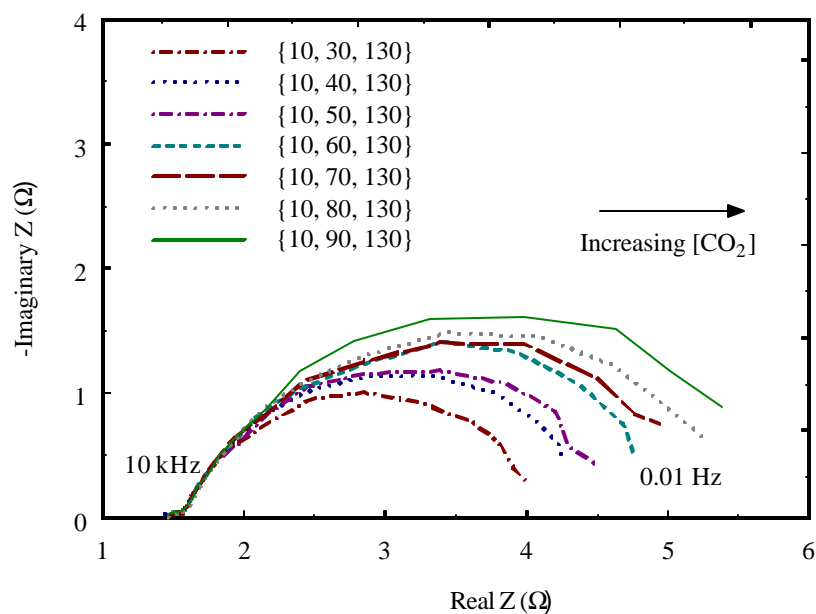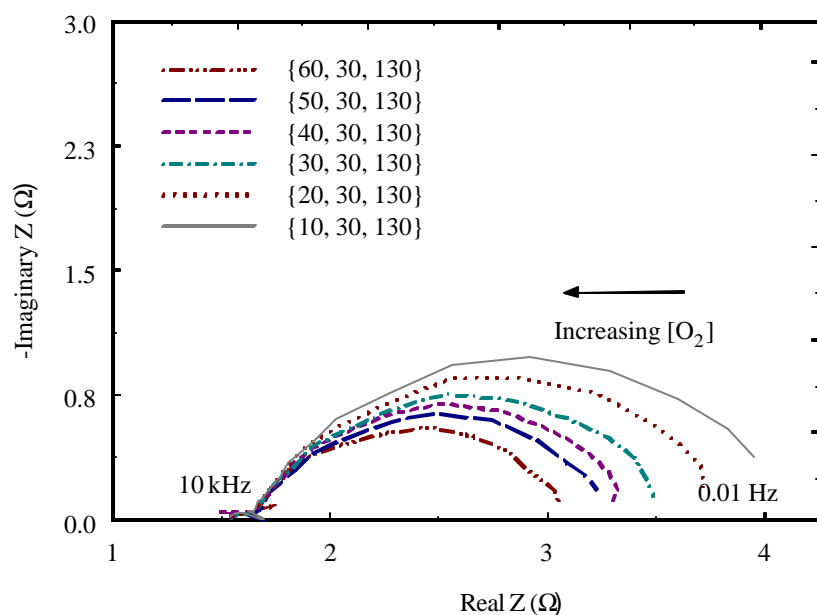
Figure 19a

Figure 19. Nyquist plots of impedance response of cobalt encapsulated nickel electrode as a function of O_2 and CO_2 partial pressures at 650°C (a) and 700°C (b) (the numbers in parenthesis "{}" indicates the O_2, CO_2 and N_2 concentrations in cc/min).

Co-Ni Tape - post test

Ni Tape - post test

Intensity (arbitrary units)

2 theta (deg)
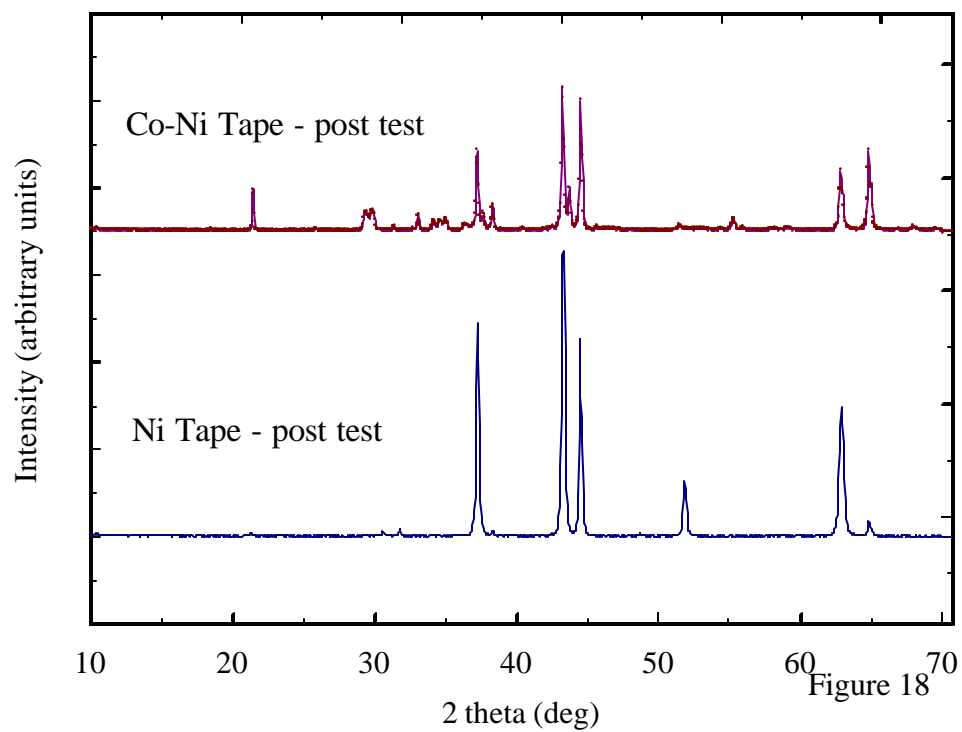
Figure 18

Figure 20.   XRD patterns of NiO and Co-NiO cathodes treated in molten carbonate under cathode gas conditions for a period of 300 hours.
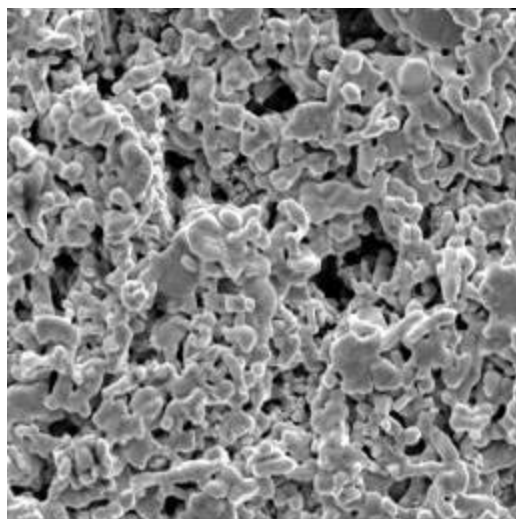
Magnification X 2000

Figure 21. SEM photograph of cobalt microencapsulated nickel powder electrode obtained by tape casting and sintering.
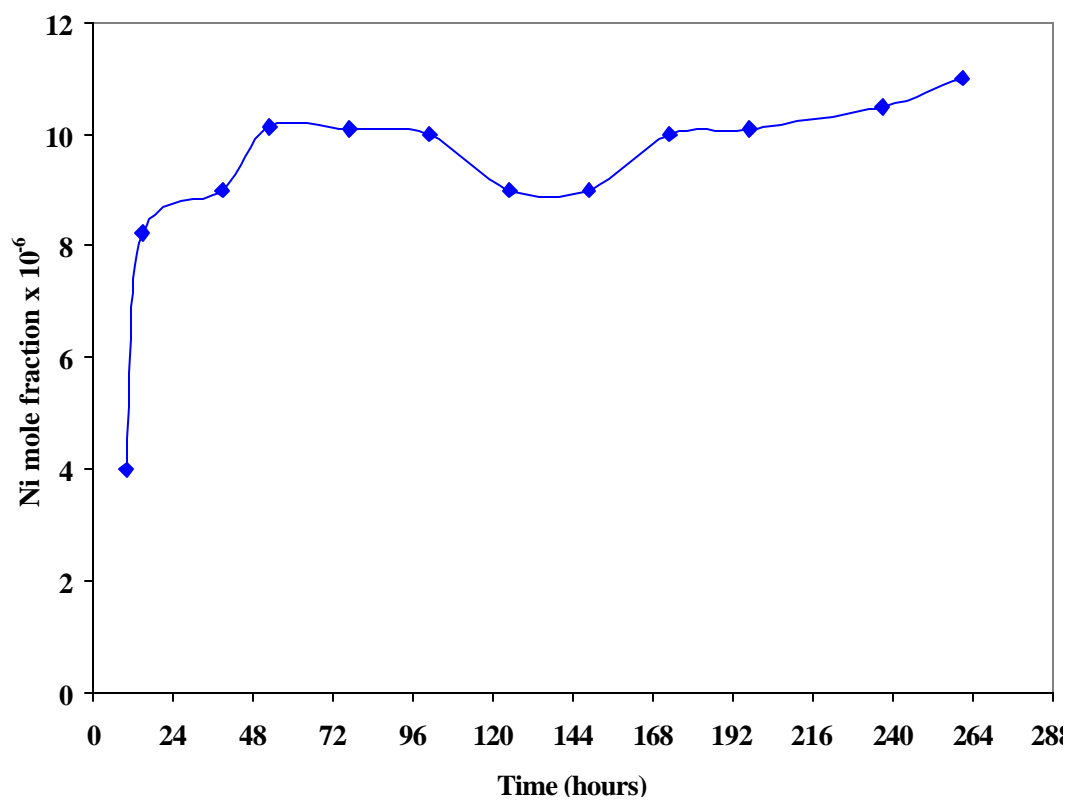
Figure 22. Atomic absorption spectroscopy analysis of dissolved nickel in molten carbonate melt.
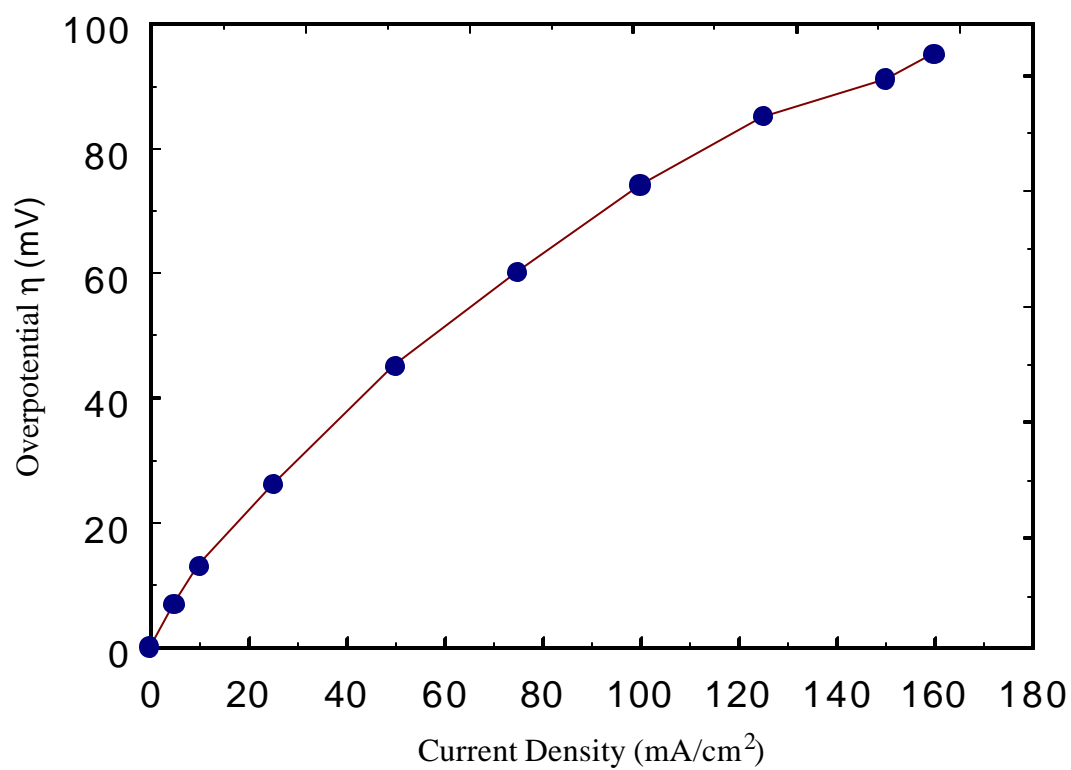
Figure 23. Cathode polarization behavior at different current loads for cobalt encapsulated nickel powder electrode.
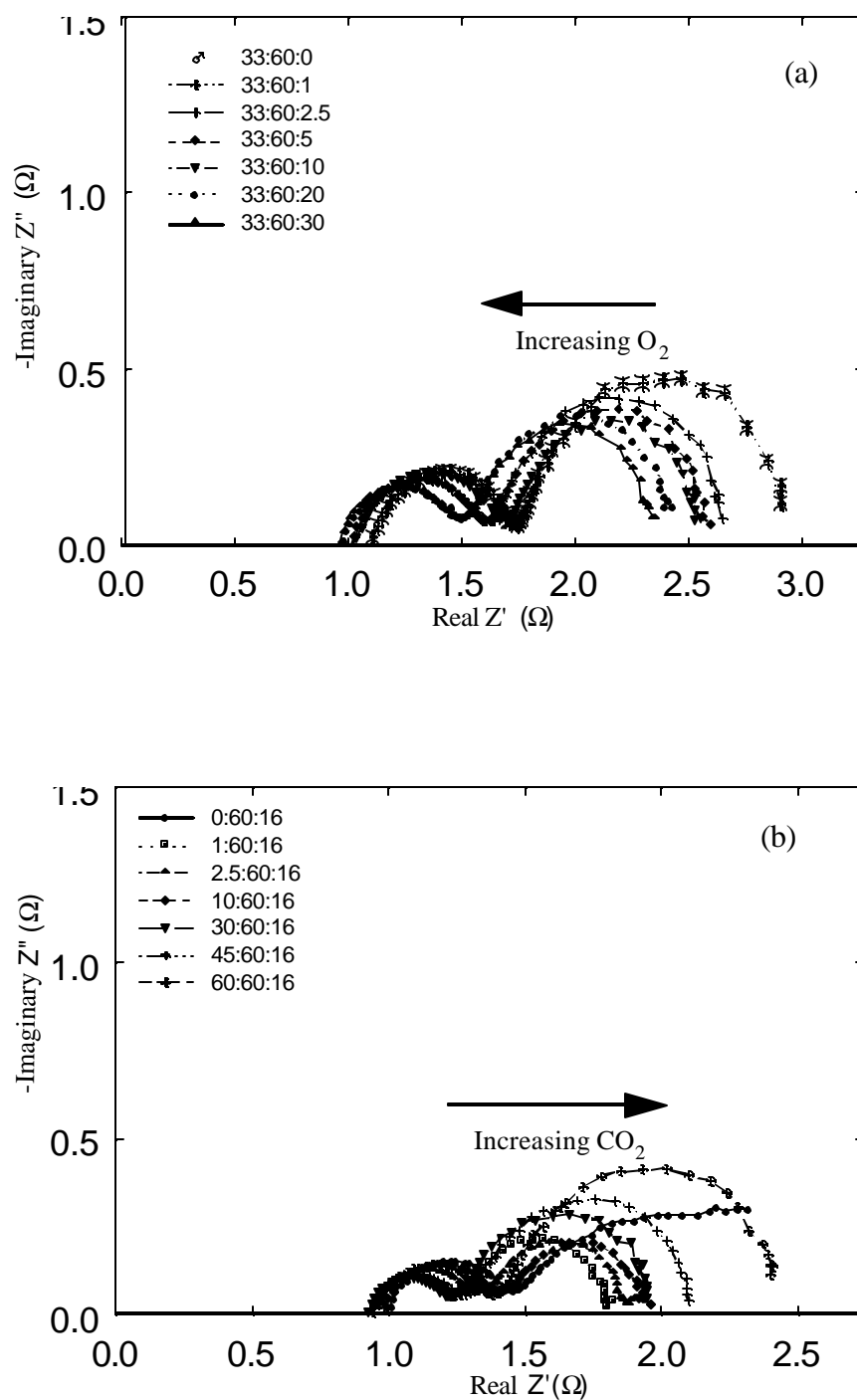
Figure 24. Nyquist plots of impedance response of cobalt encapsulated nickel powder electrode as a function of (a) O_2 and (b) CO_2 partial pressures at 650°C (the numbers in parenthesis "{}" indicates the O_2, CO_2 and N_2 concentrations in cc/min).
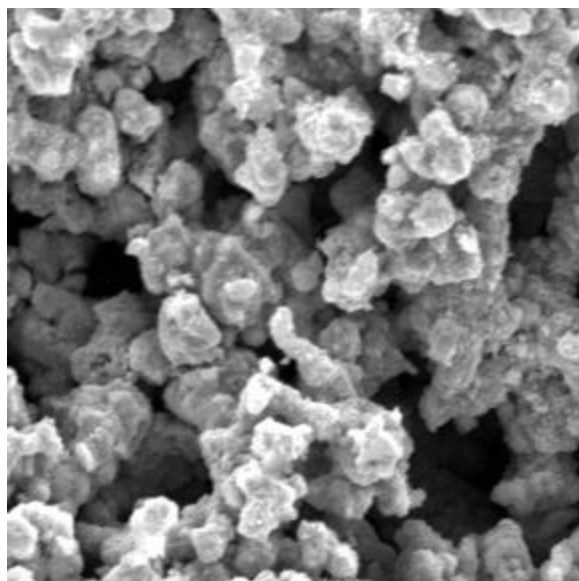
Figure 25.   SEM pictures of La0.8Sr0.2CoO3 coated NiO electrodes obtained after sintering. (Magnification x 2000).
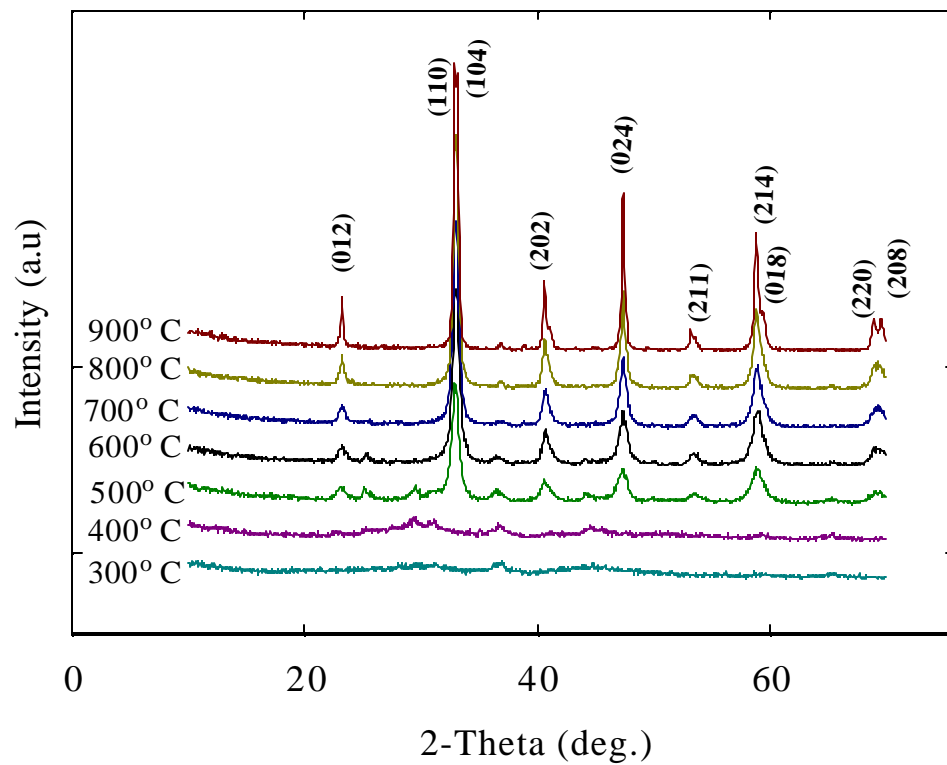
Figure 26. X-ray diffraction patterns of $La_{0.8}Sr_{0.2}CoO_3$ obtained after different heat treatment of the gel precursor.
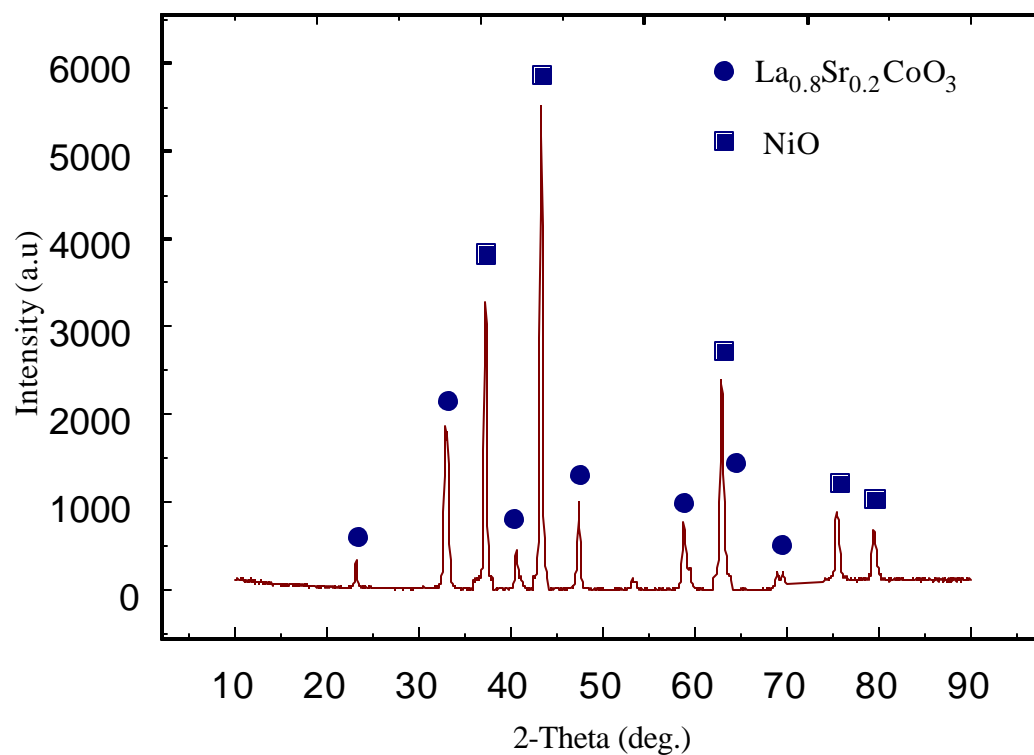
Figure 27.　X-ray diffraction patterns of $La_{0.8}Sr_{0.2}CoO_3$ coated NiO sintered at 900° C.
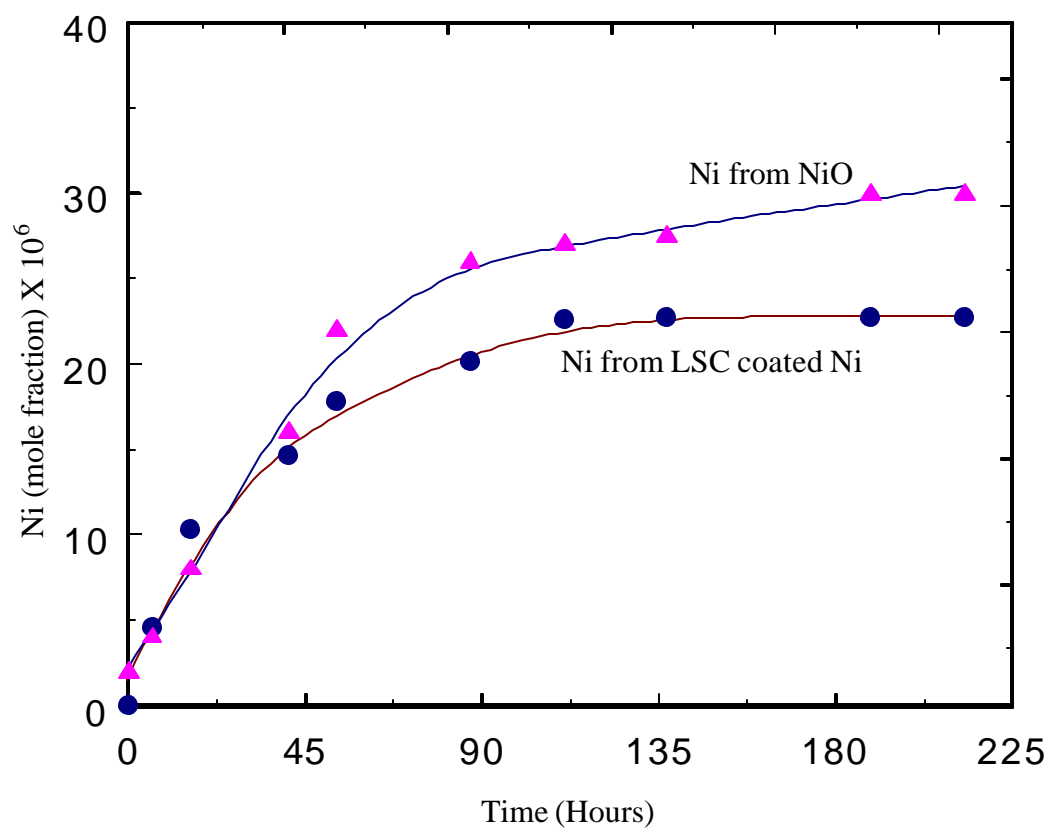
Figure 28. Atomic absorption spectroscopy analysis of dissolved nickel in molten carbonate melt coming from $La_{0.8}Sr_{0.2}CoO_3$ electrodes during short-term stability tests.
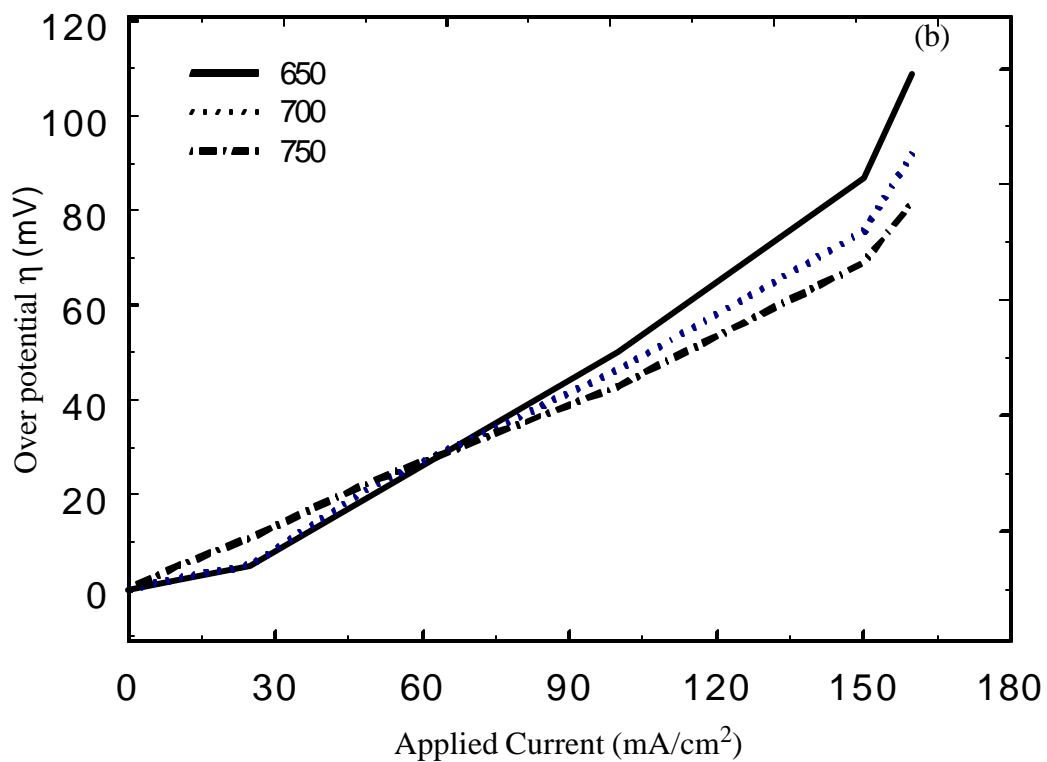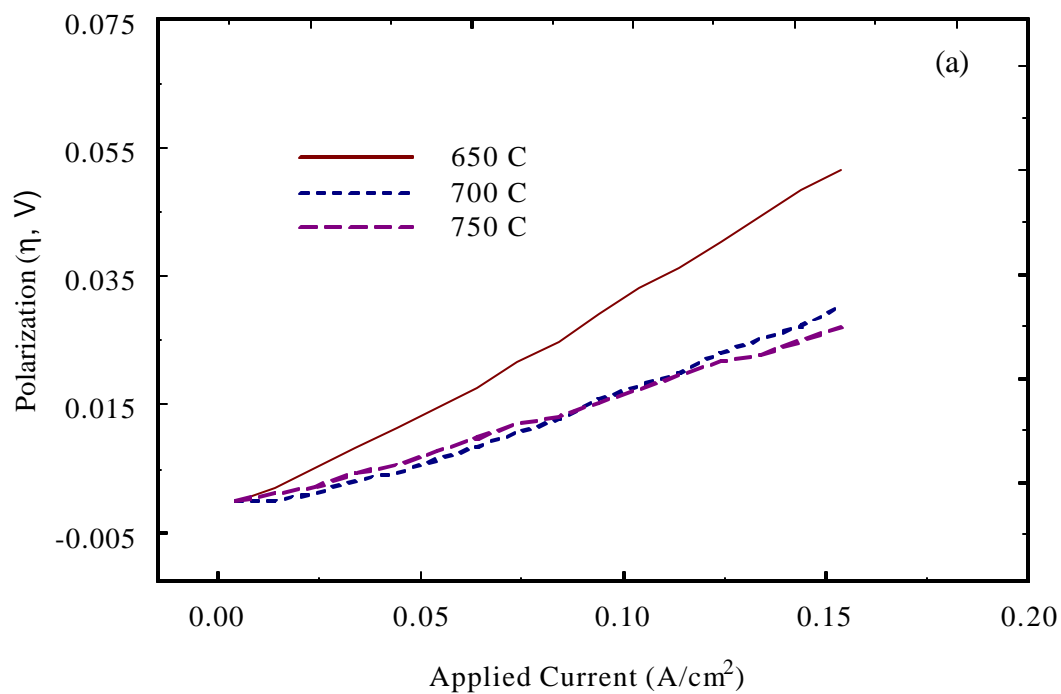
Figure 29. Comparison of cathode polarization behavior at different temperatures for bare nickel oxide (a) and $La_{0.8}Sr_{0.2}CoO_3$ coated NiO cathodes(b).
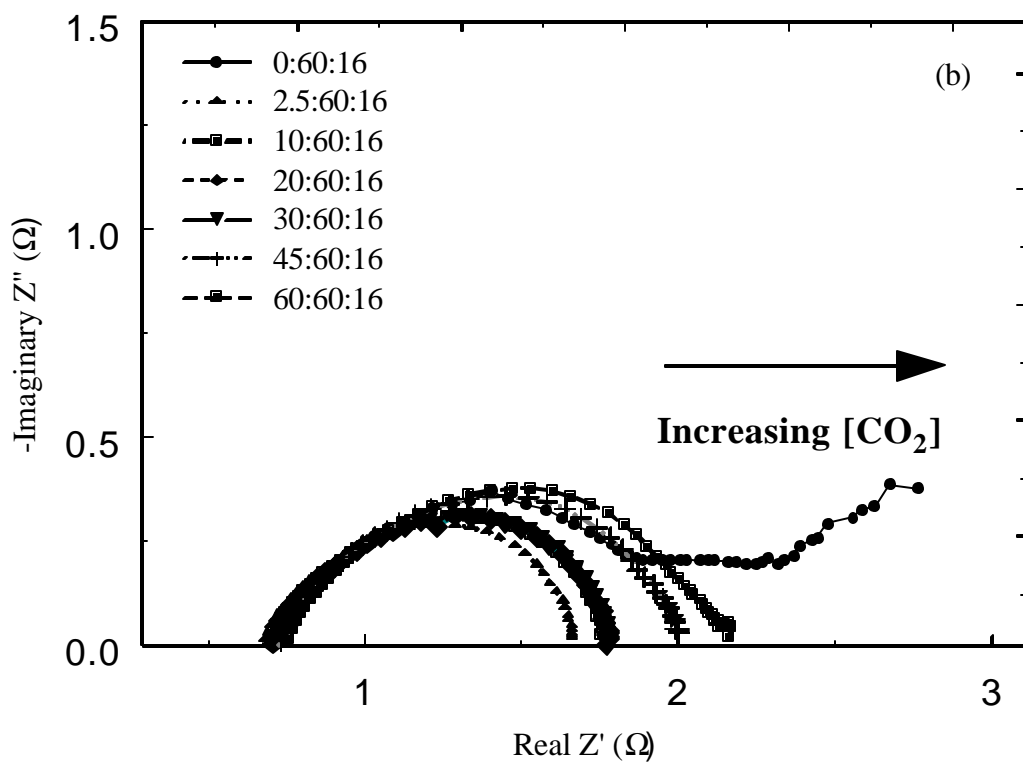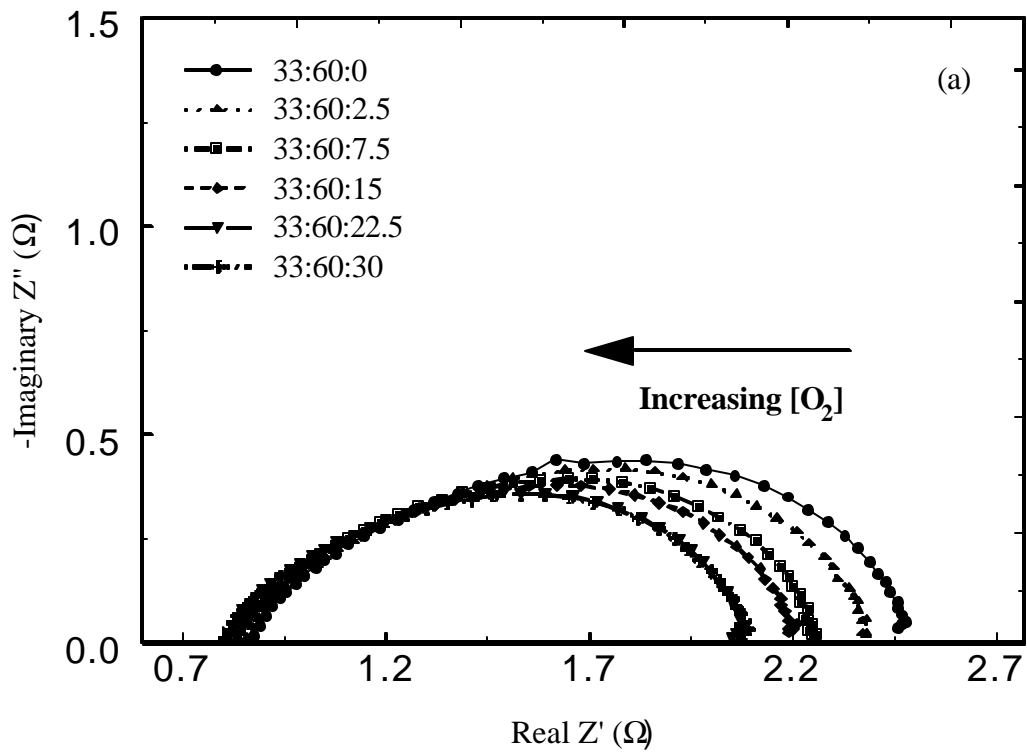
Figure 30 (a and b)
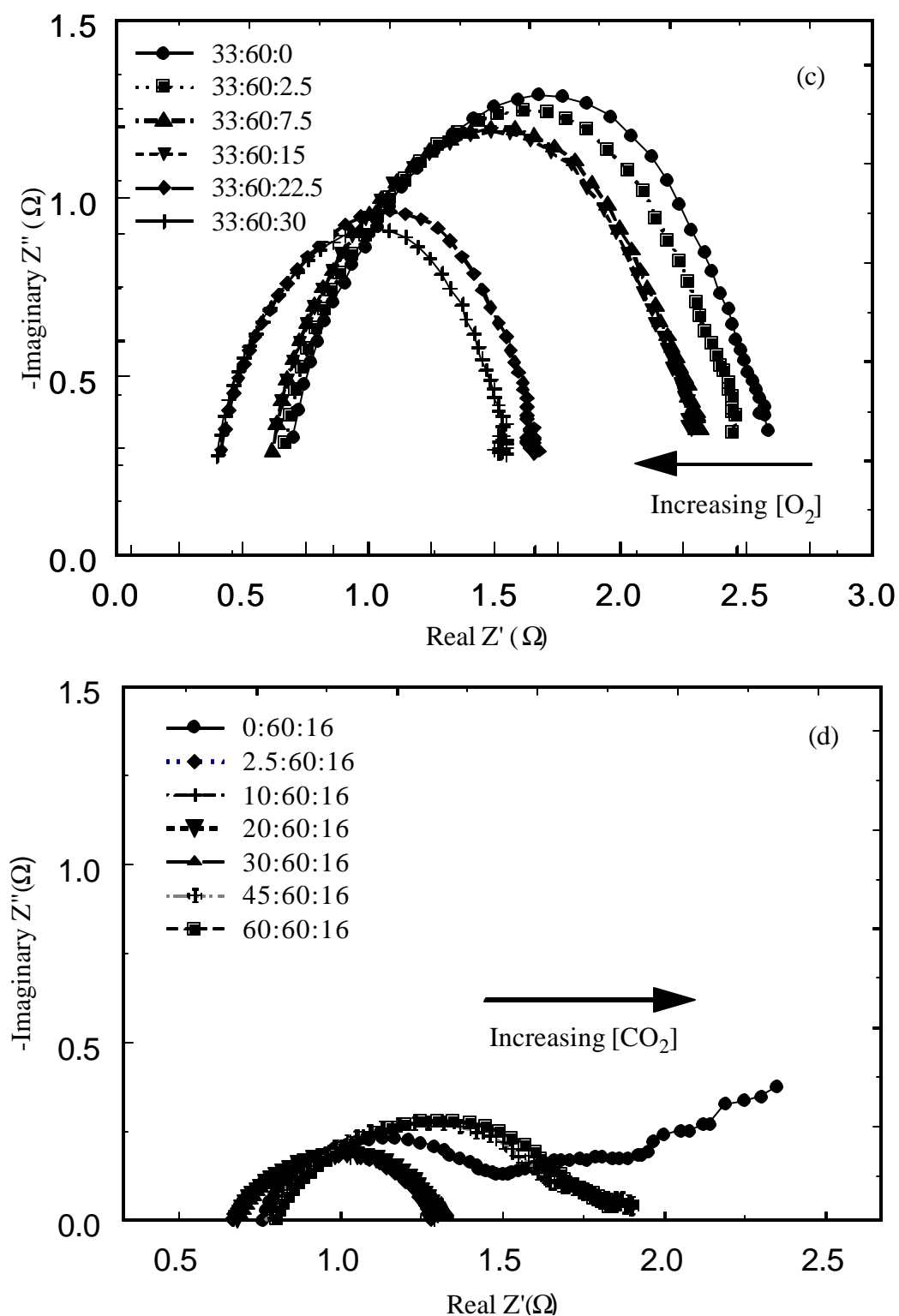
Figure 30. Nyquist plots of impedance response of $La_{0.8}Sr_{0.2}CoO_3$ coated NiO electrode as a function of O_2 and CO_2 partial pressures at 650°C (a and b), 700°C (c and d).
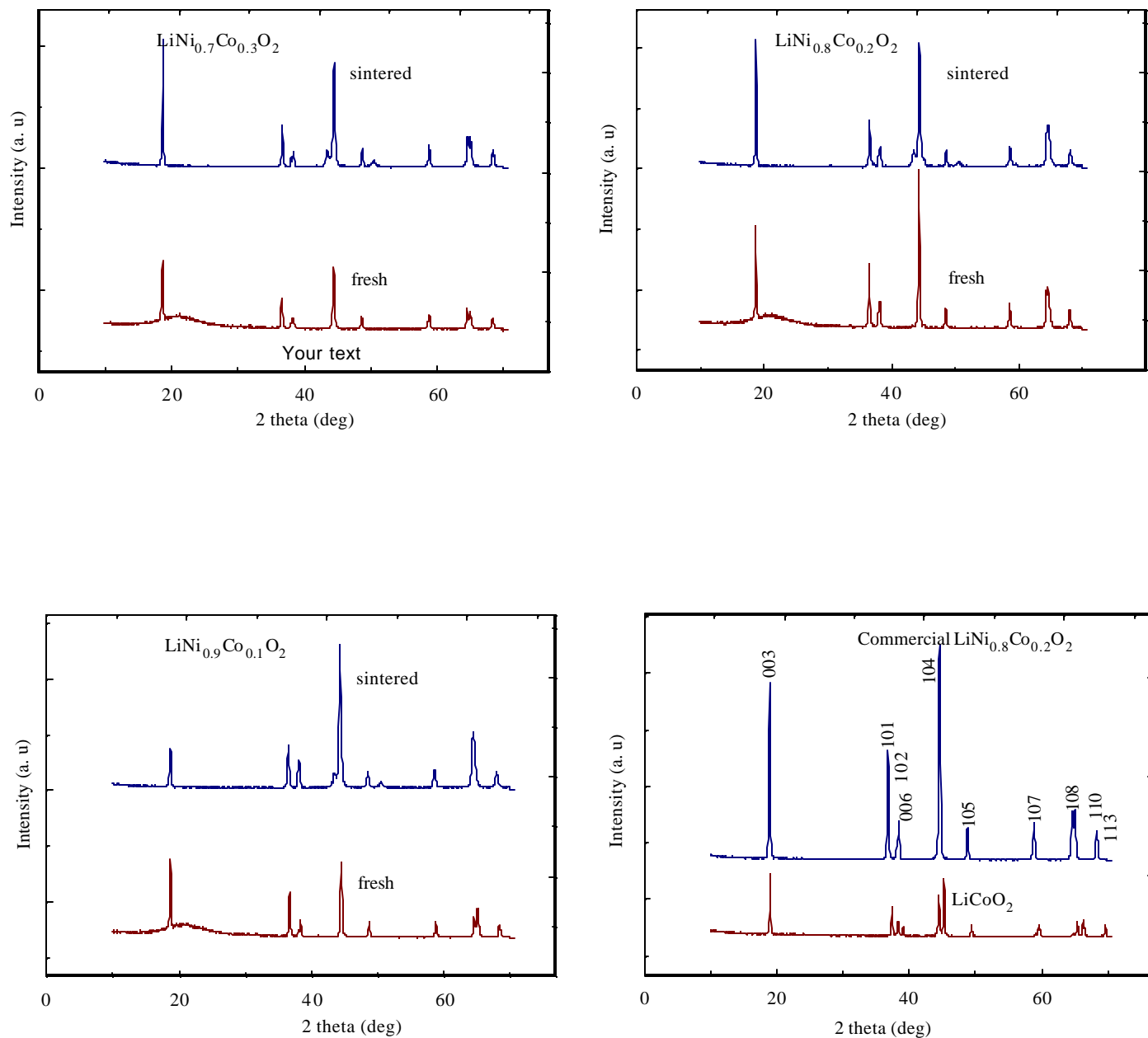
Figure 31. X-ray diffraction patterns of pristine $LiCoO_2$ and $LiNi_xCo_{1-x}O_2$ solid solutions obtained by solid-state reaction procedure from lithium nitrate, nickel hydroxide and cobalt oxalate precursors. The XRD pattern of commercial $LiNi_{0.8}Co_{0.2}O_2$ is shown for comparison.
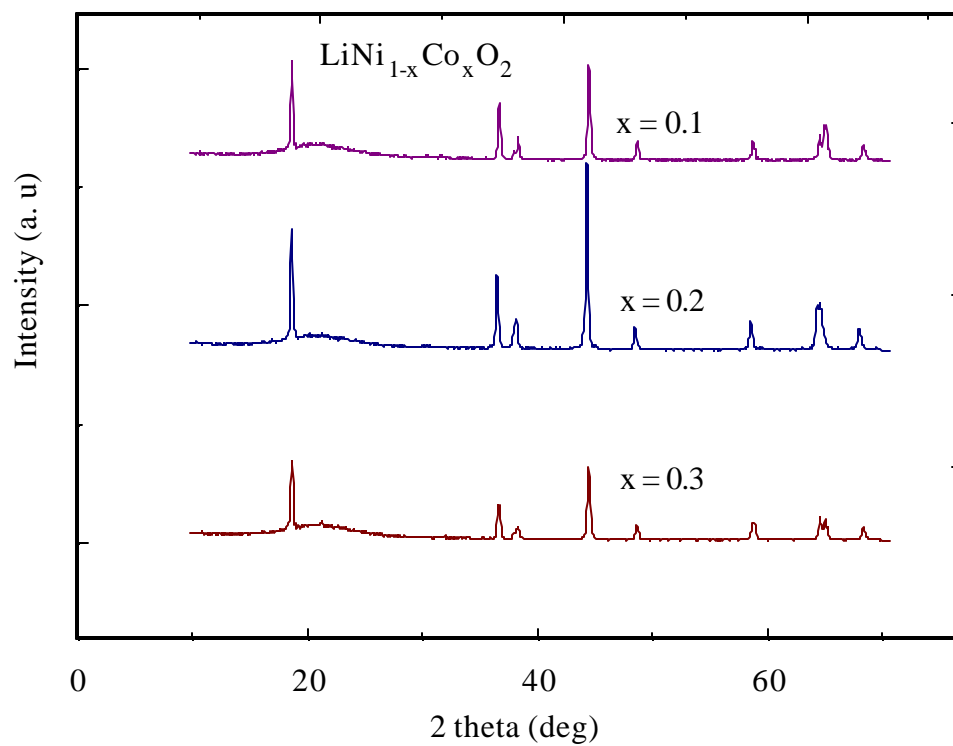
Figure 32. X-ray diffraction patterns of $LiNi_xCo_{1-x}O_2$ mixed oxides after sintering in air at 800°C for 24 hours.
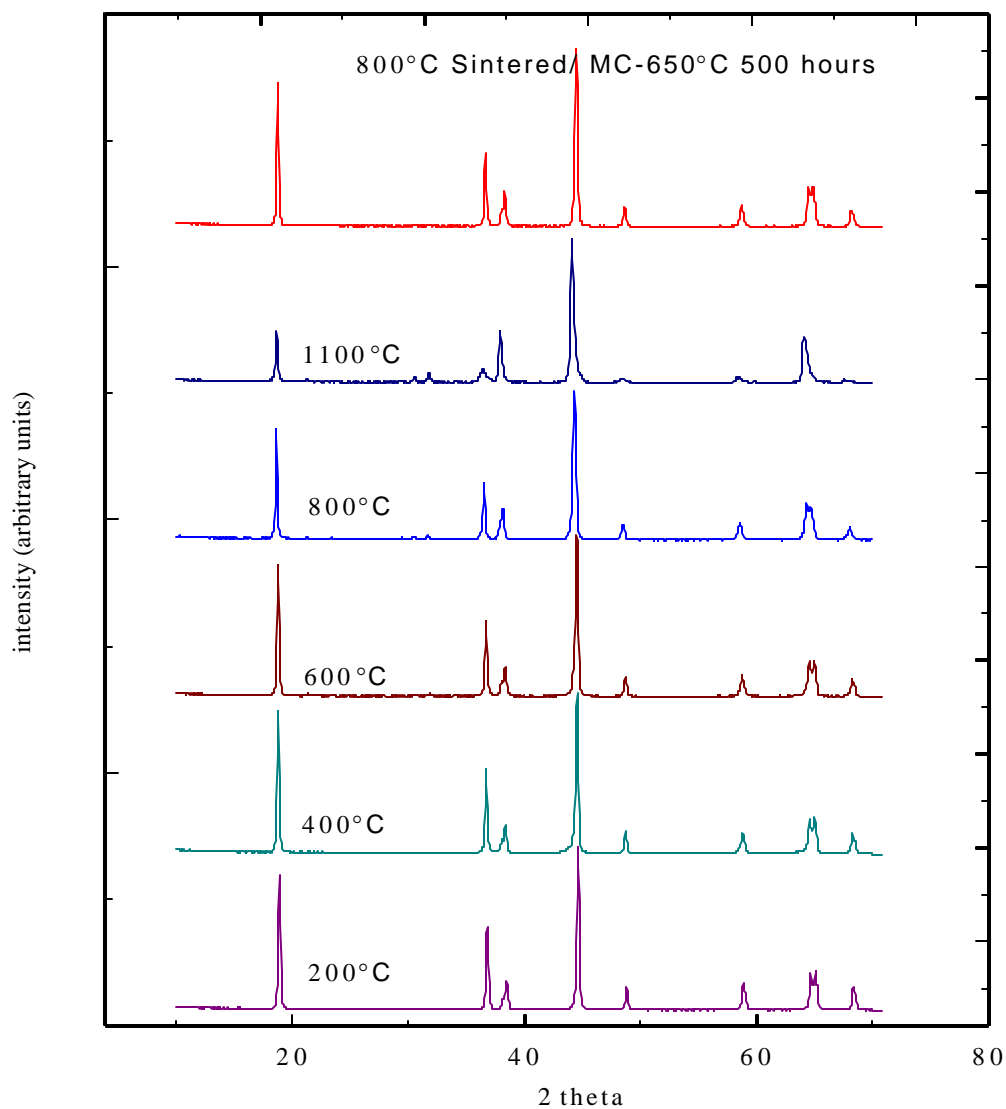
Figure 33. X-ray diffraction patterns of LiNi$_{0.8}$Co$_{0.2}$O$_2$ mixed oxides after sintering at different temperatures in air 24 hours. LiNi$_{0.8}$Co$_{0.2}$O$_2$ sintered in molten carbonate eutectic at 650°C for 500 hours is shown for comparison.
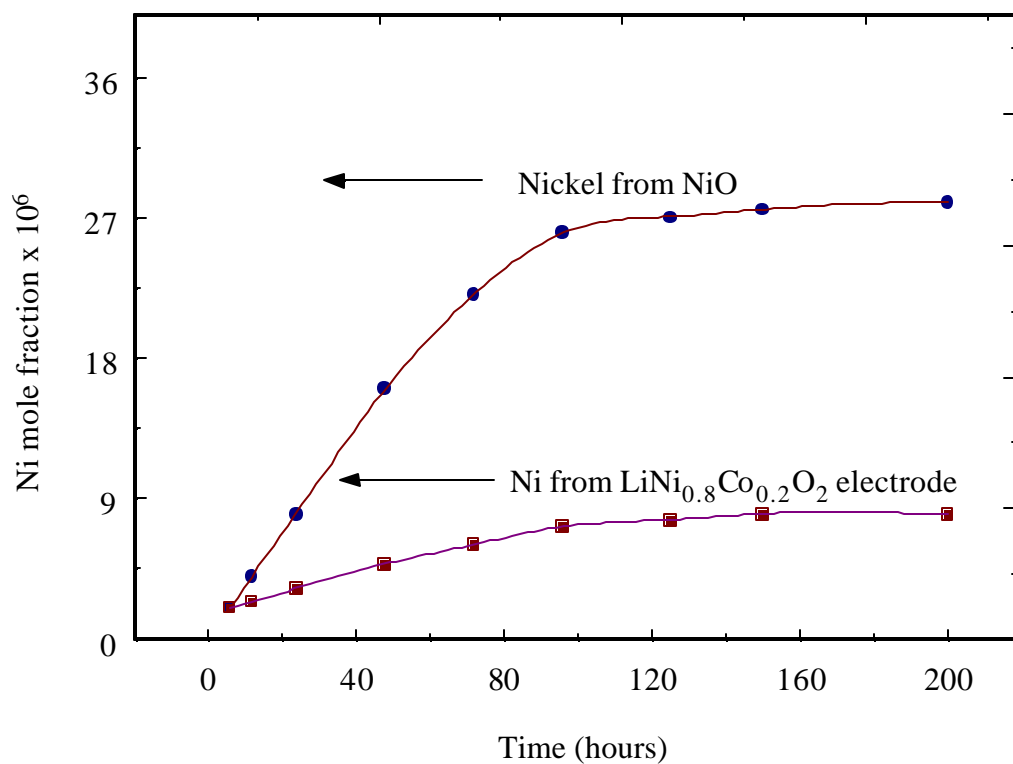
Figure 34. Atomic absorption spectroscopy analysis of dissolved nickel in molten carbonate melt coming from $LiNi_{0.8}Co_{0.2}O_2$ electrodes during immersion tests.
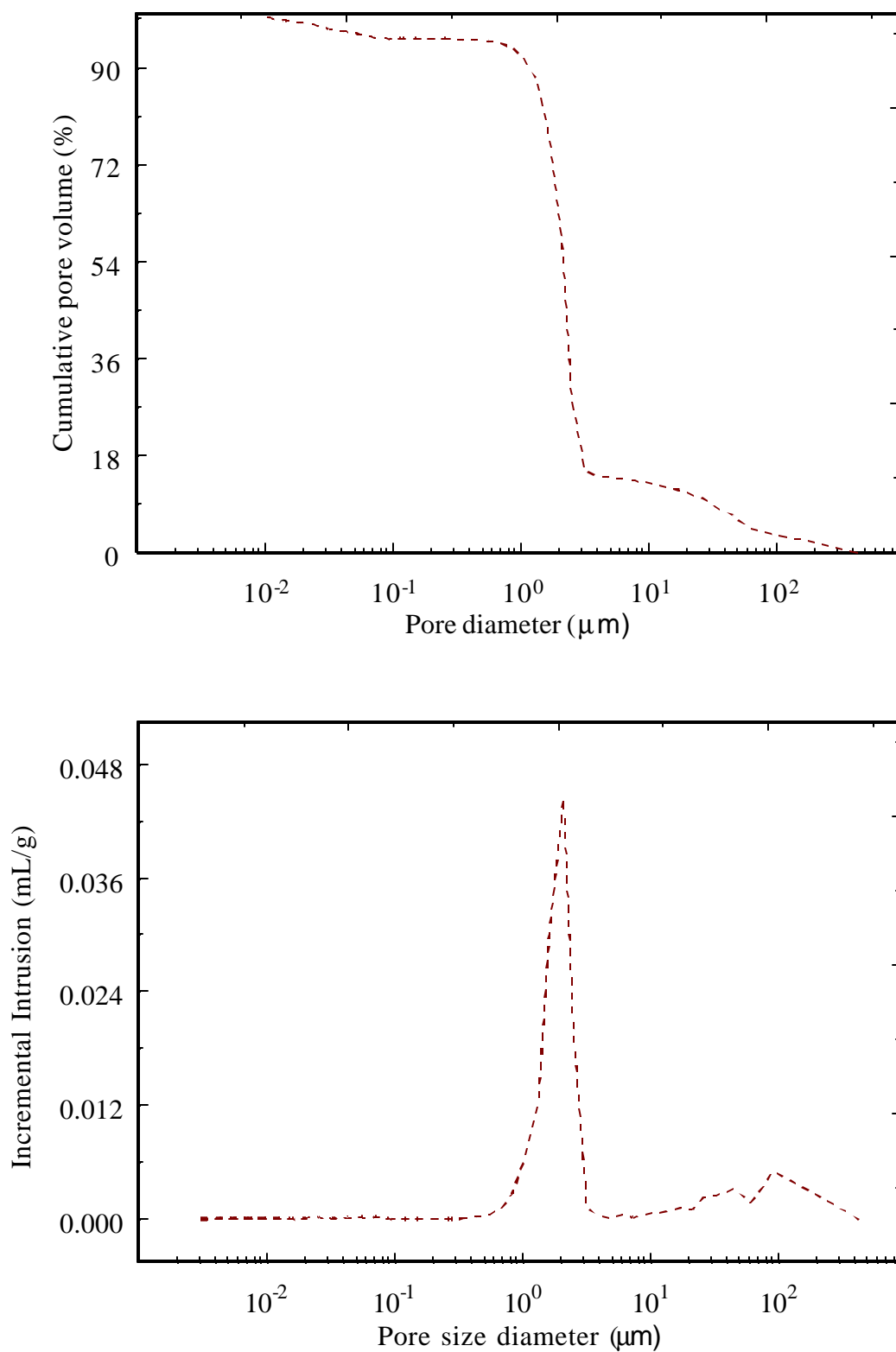
Figure 35. Pore volume distribution obtained on LiNi$_{0.8}$Co$_{0.2}$O$_2$ electrodes by mercury intrusion method.
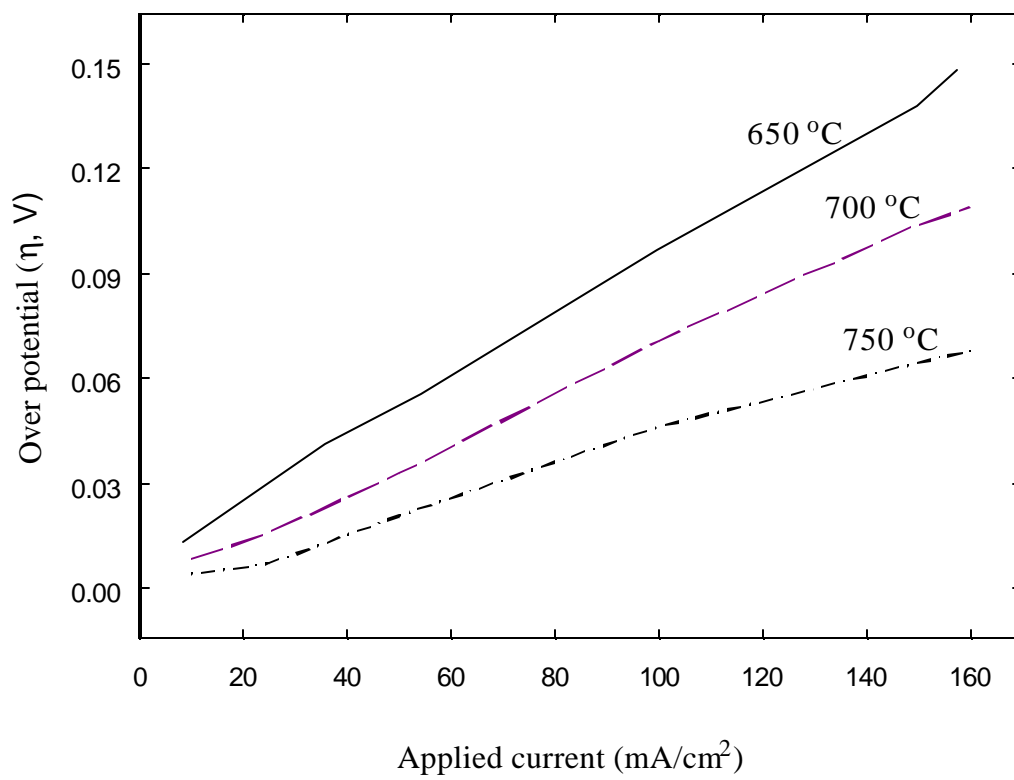
Figure 36. Comparison of Cathode polarization behaviors at different current loads for $LiNi_{0.8}Co_{0.2}O_2$ cathodes at different temperatures.
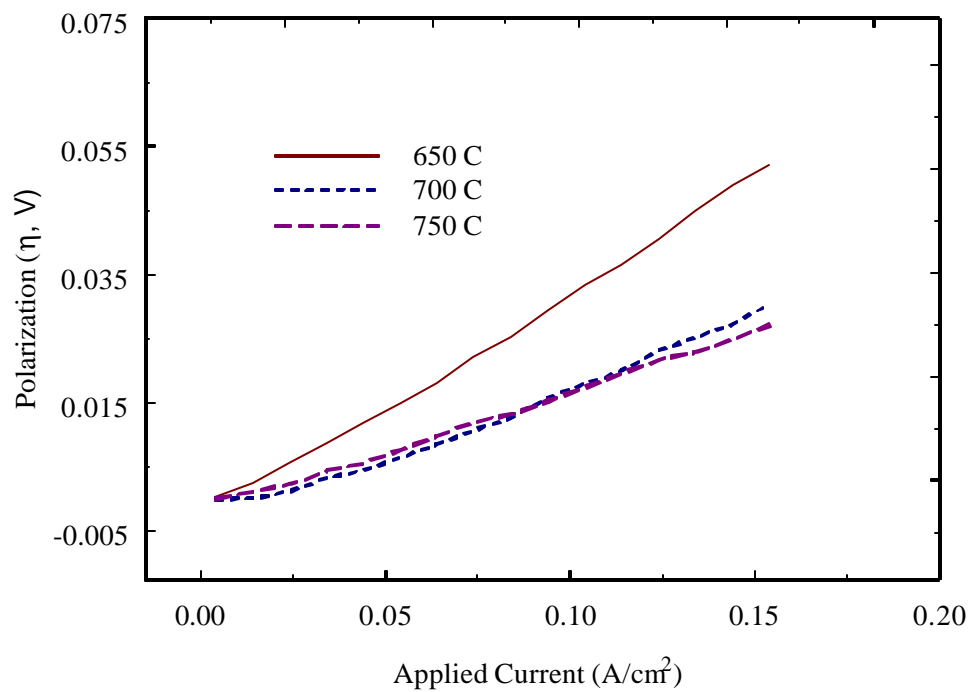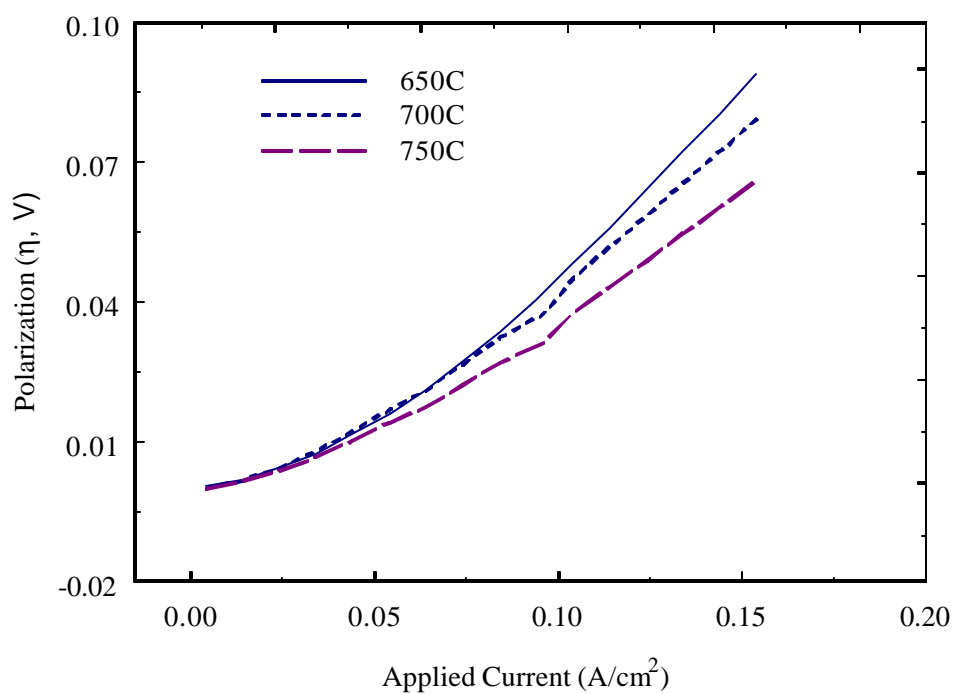
Figure 37. Polarization behavior of (a) bare and (b) cobalt encapsulated nickel oxide electrodes at different operating temperatures.

124
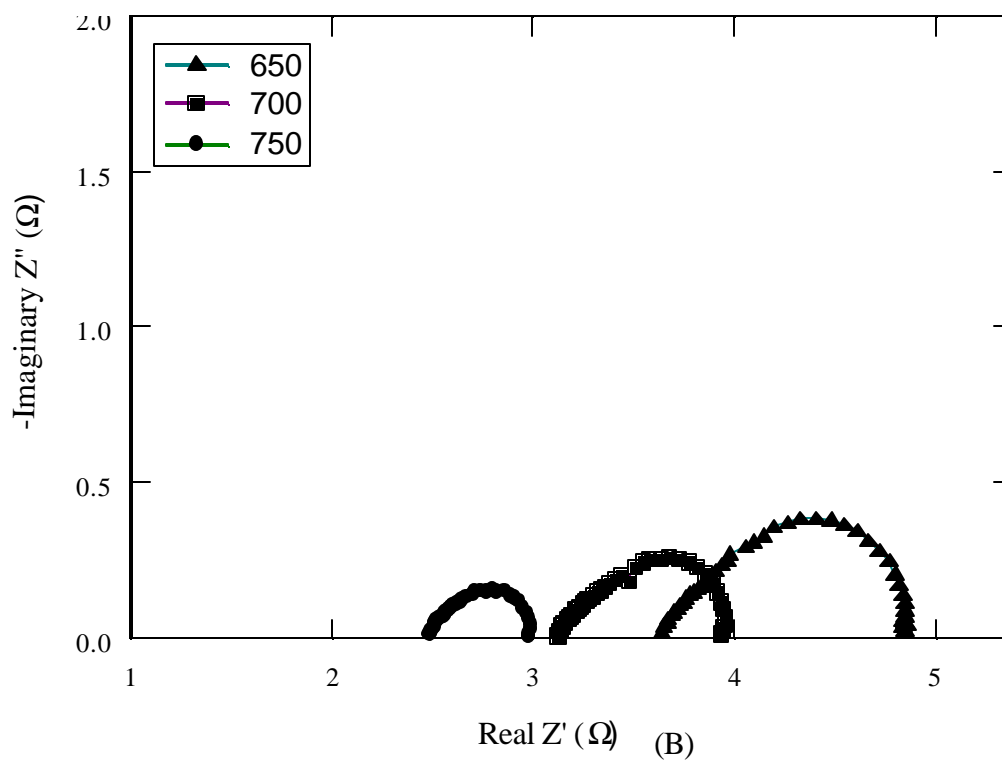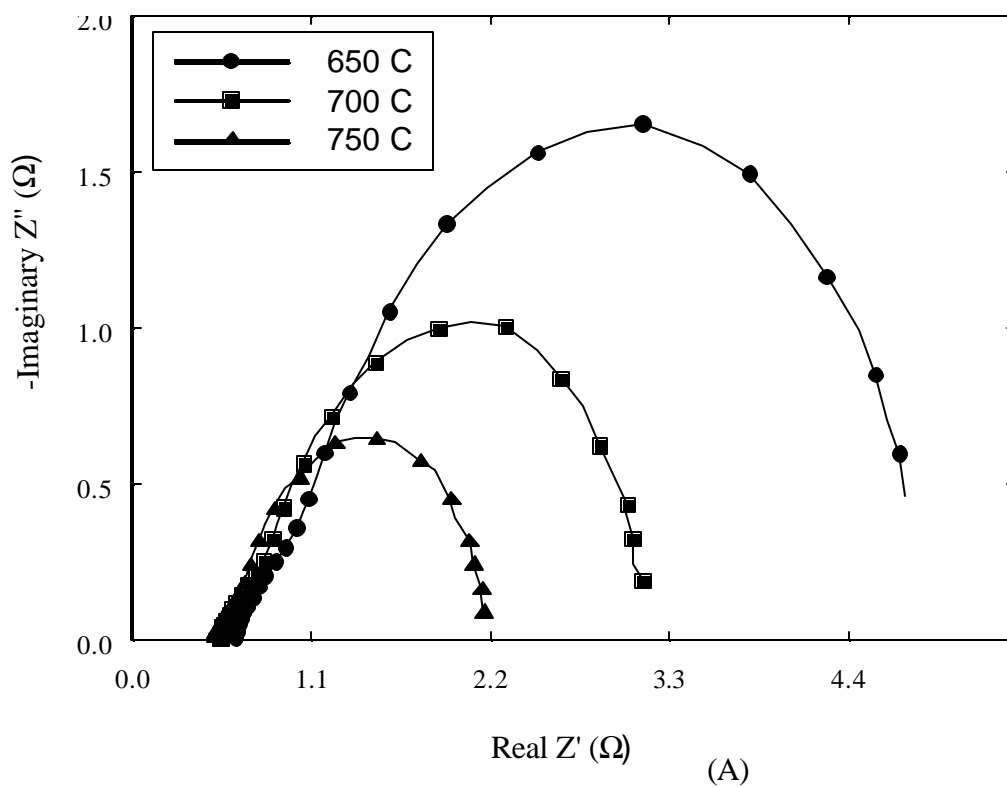
Figure 38. Nyquist plots of LiCoO$_2$ (a) and NiO (b) at different operating temperatures in standard cathode gas atmosphere.

(A)

(B)

Figure 39a & 39b

126

(C)

(D)

Figure 39c & 39d

127

(E)

(F)
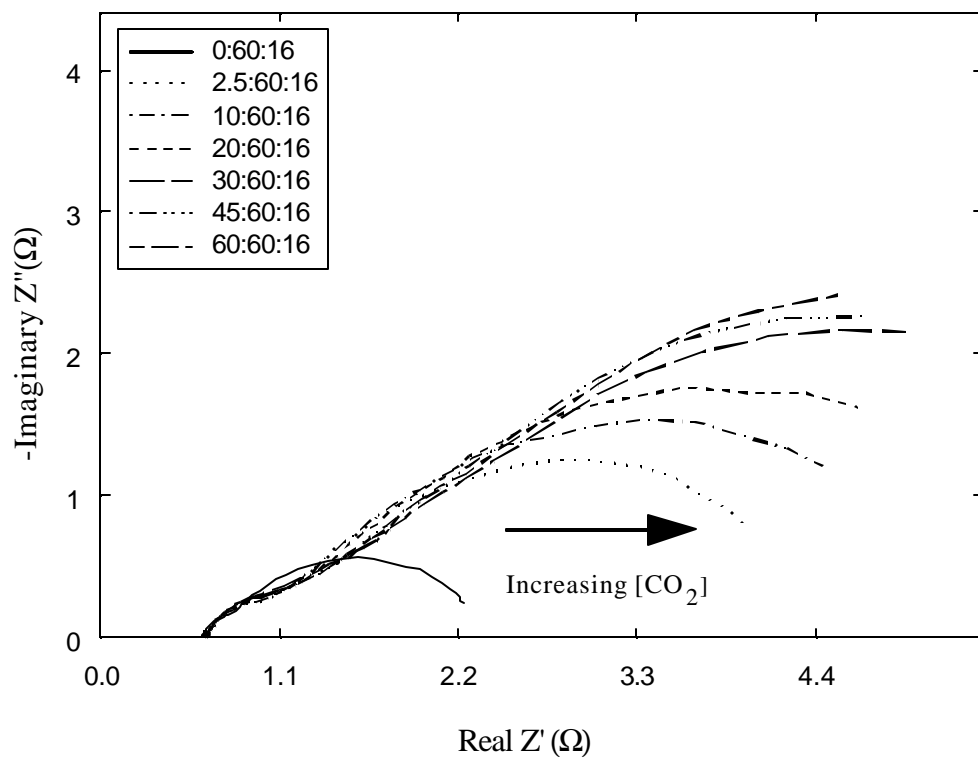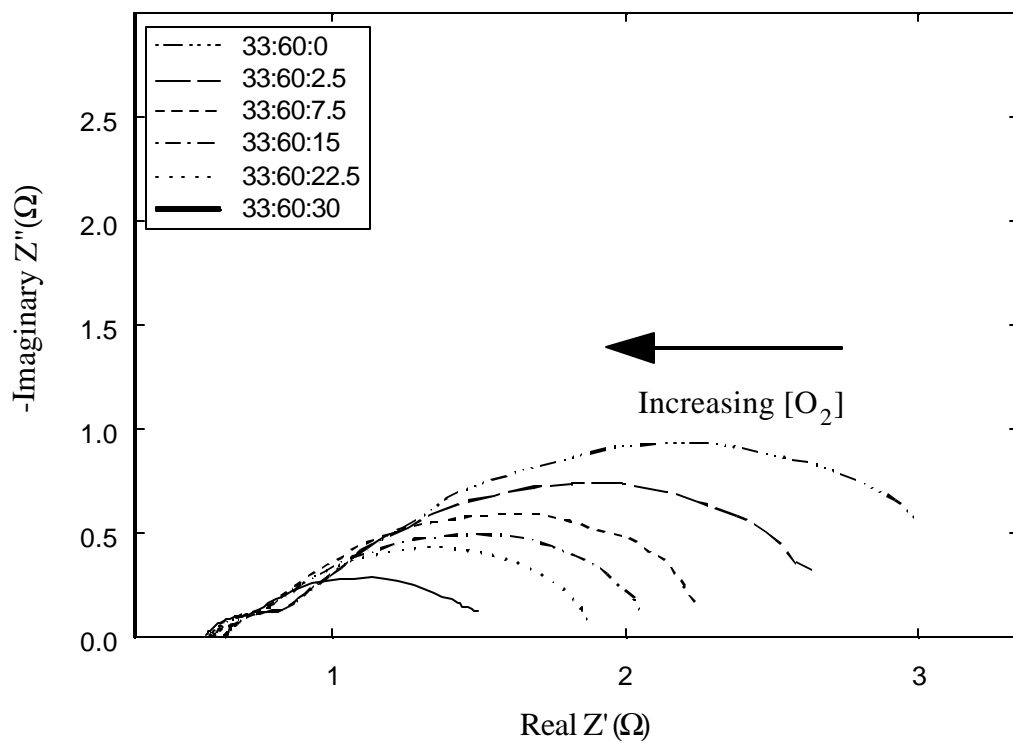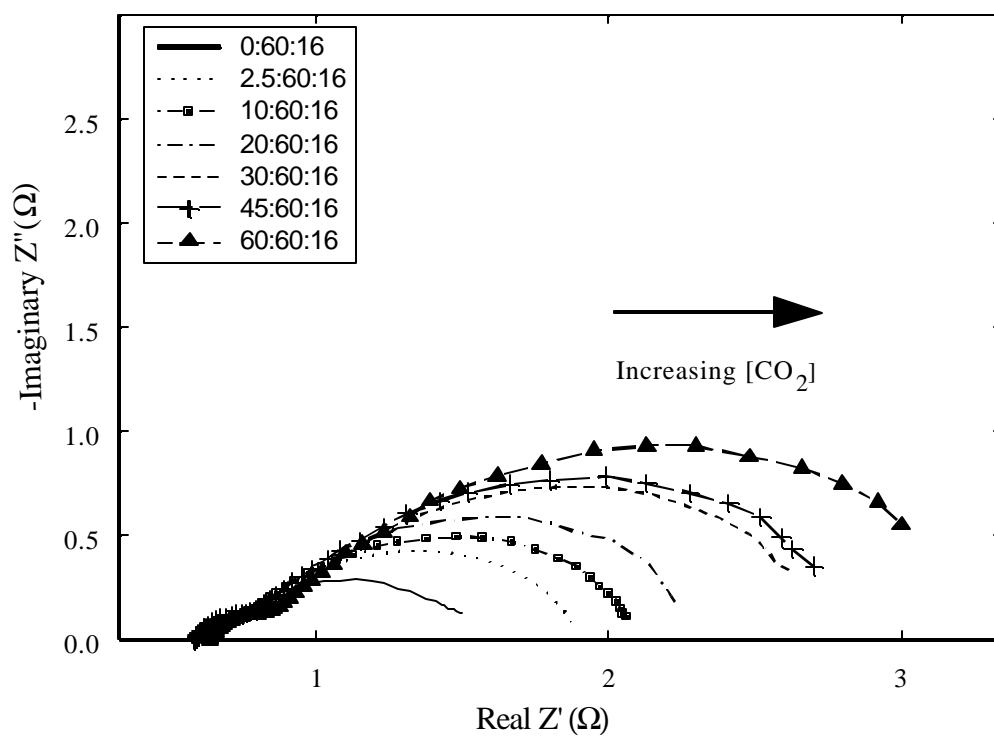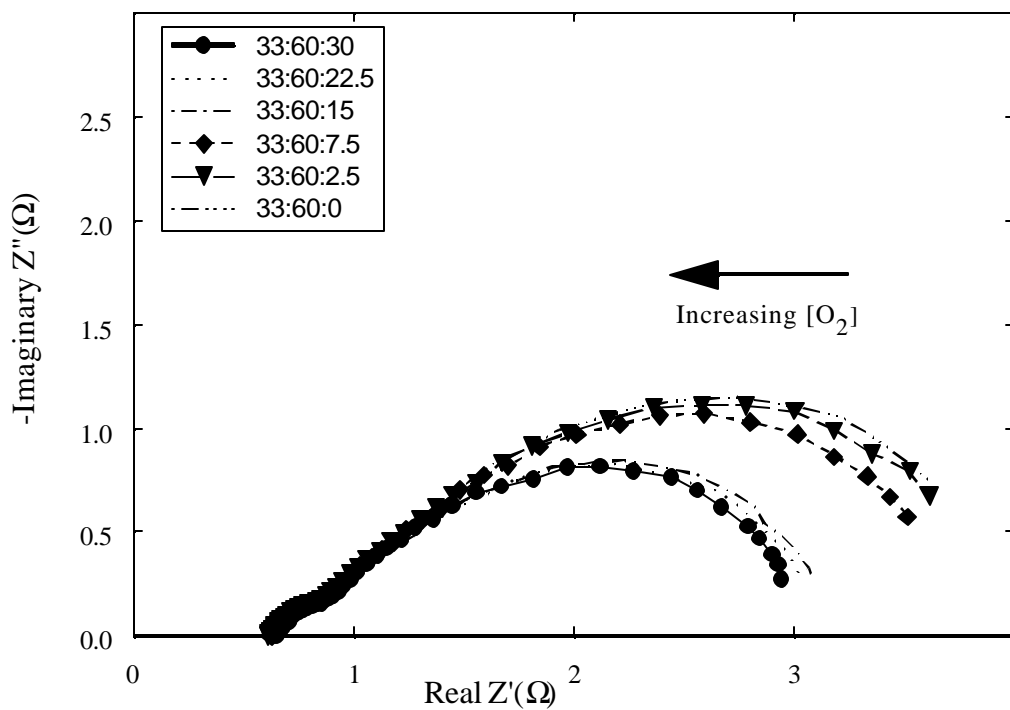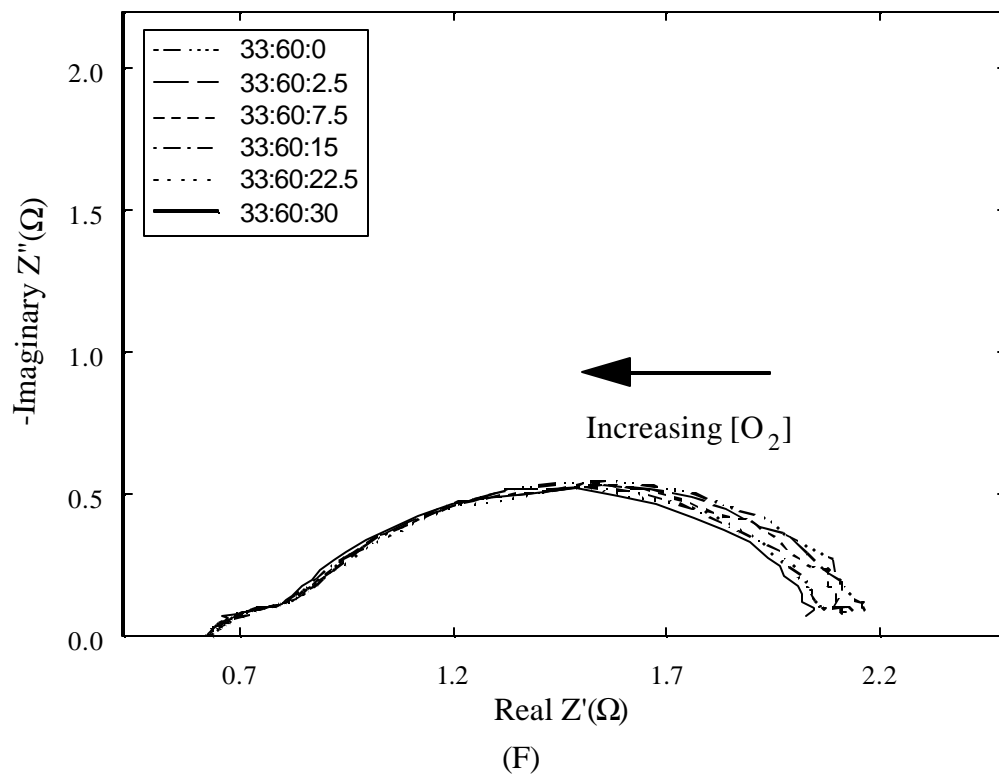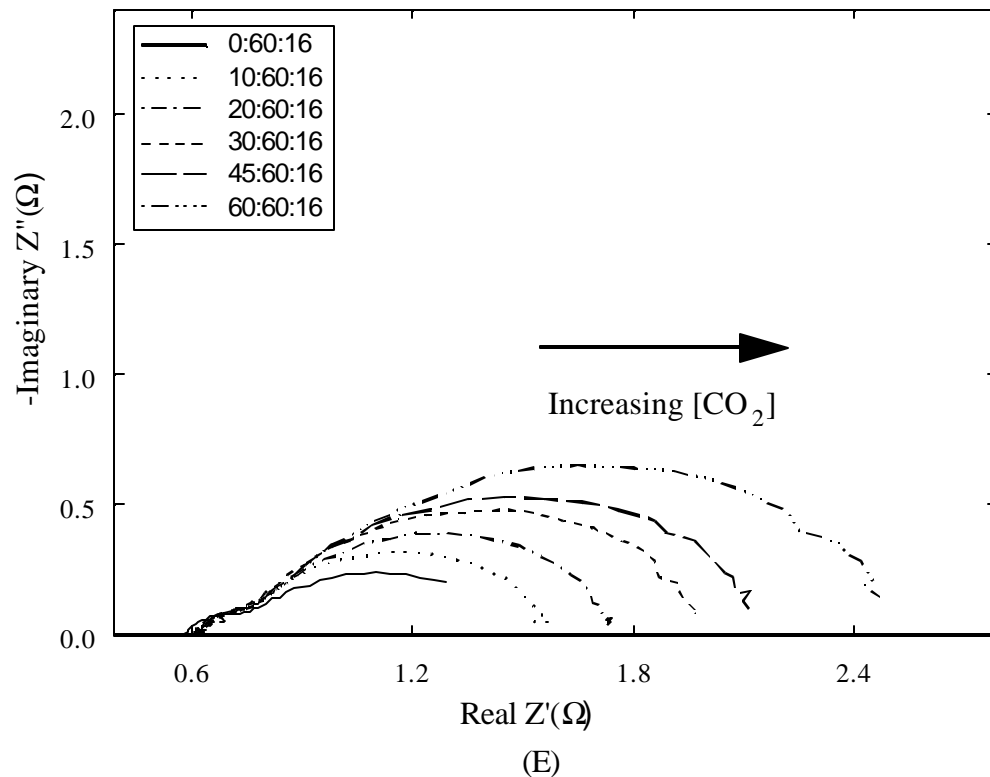
Figure 39. Nyquist plots of impedance response of $LiNi_{0.8}Co_{0.2}O_2$ electrode as a function of O_2 and CO_2 partial pressures at 650°C (a & b) and 700°C (c & d) 750° C (e & f) (the numbers in parenthesis "{}" indicates the CO_2, N_2 and O_2 concentrations in cc/min).

128
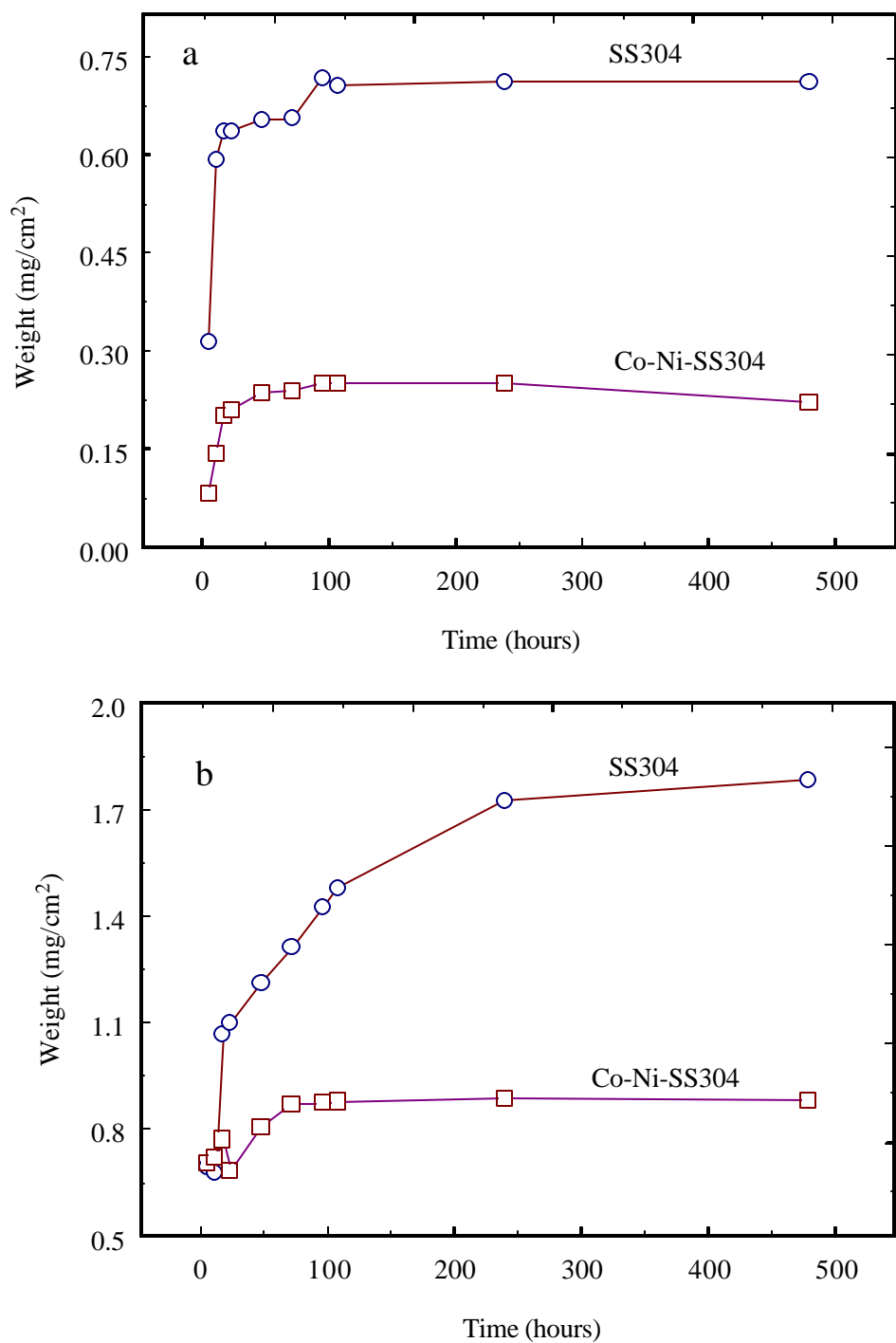
Figure 40. Atomic absorption spectroscopy analysis of dissolved chromium (a, top) and nickel (b, bottom) concentrations in the molten carbonate melt due to the immersion of SS304 and Co-Ni-SS304 after immersion in the molten carbonate melt.
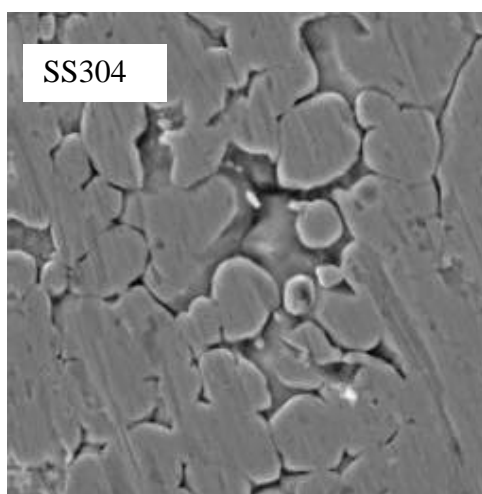
SS304

12 mm
Magnification = 1500
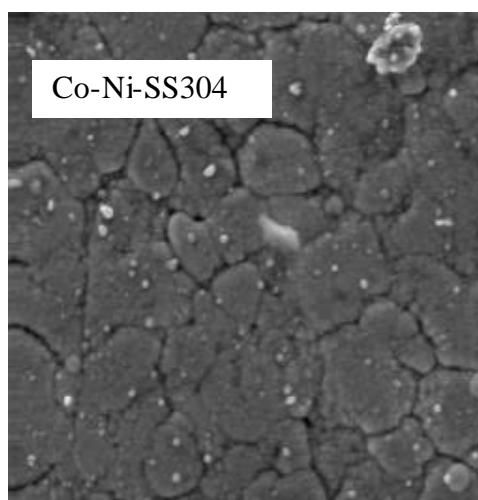
Co-Ni-SS304

9.5 mm
Magnification = 2000

Posttest SS304

12 mm
Magnification = 1500
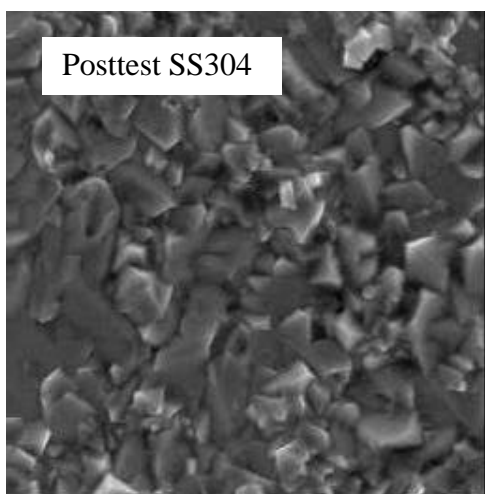
Posttest Co-Ni-SS304
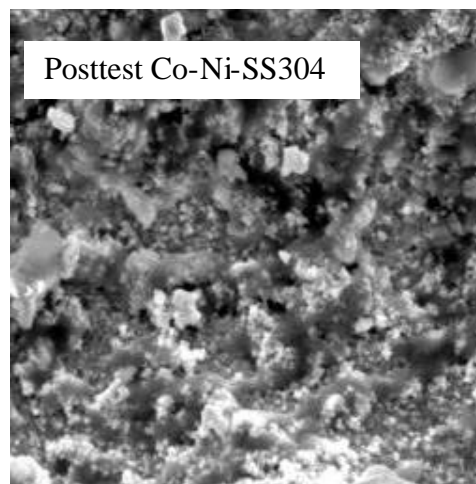
12 mm
Magnification = 1500

Figure 41. SEM photographs of fresh and posttest SS304 and Co-Ni-SS304. Post-test specimens were obtained after 500 hours of operation in molten carbonate under cathode gas conditions.

SS304   Co-Ni-SS304
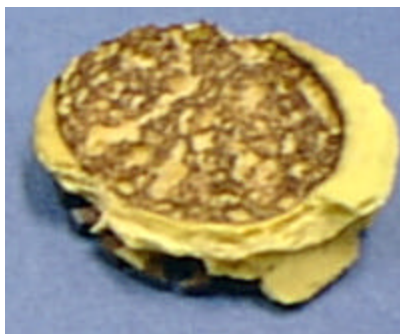
EDAX 6.5 wt.% Cr   EDAX 0.24 wt.% Cr

Figure 42.   EDAX analysis on the separator matrix.
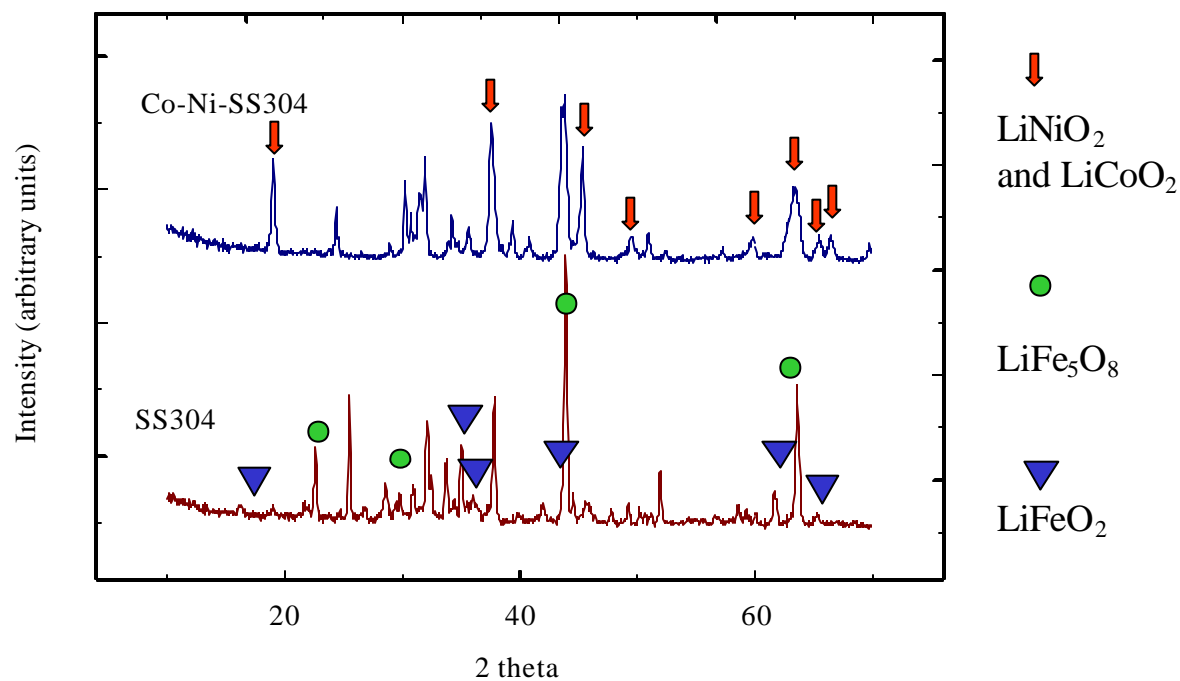
Figure 43. X-ray diffraction patterns of corrosion scales formed in posttest SS304 and Co-Ni-SS304. Post-test specimens were obtained after 500 hours of operation in molten carbonate under cathode gas conditions.
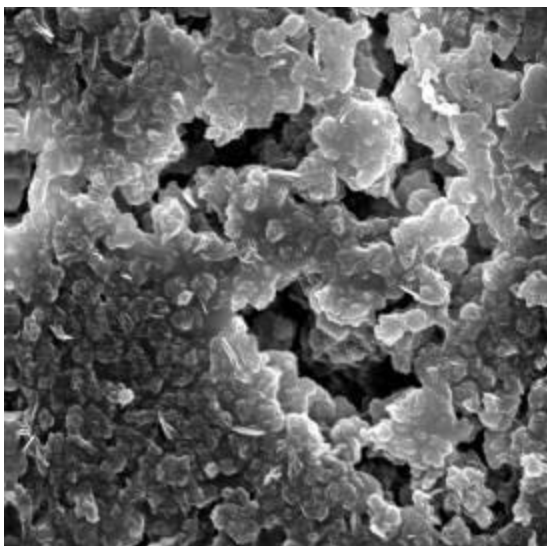
**LiAlO$_2$ Separator
Before test**

**19mm
Magnification – 1000**
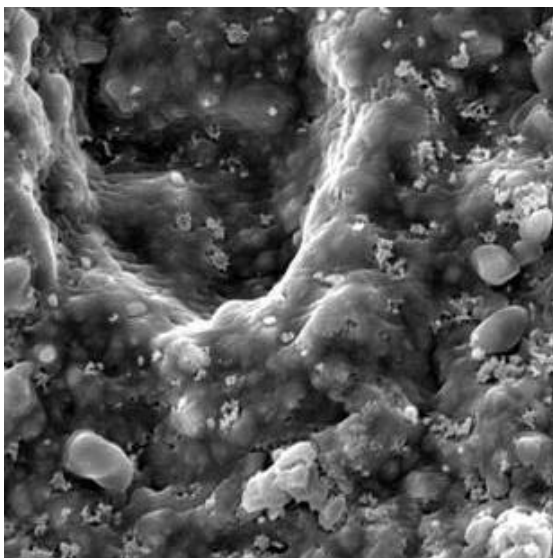
**LiAlO$_2$ Separator
SS 304 (time = 500 hours)**

**12 mm
Magnification – 1500**
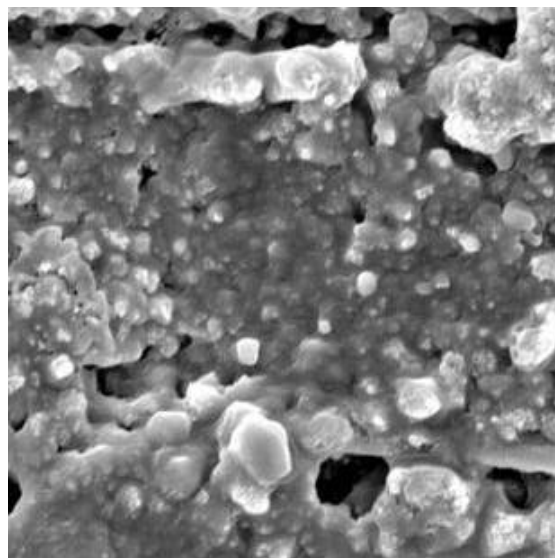
**LiAlO$_2$ Separator
Co-Ni (time = 500 hours)**

**12 mm
Magnification – 1500**

Figure 44.   SEM photographs of fresh and posttest LiAlO$_2$ separators used in cells containing SS304 and Co-Ni-SS304. Post-test specimens were obtained after 500 hours of operation in molten carbonate under cathode gas conditions.
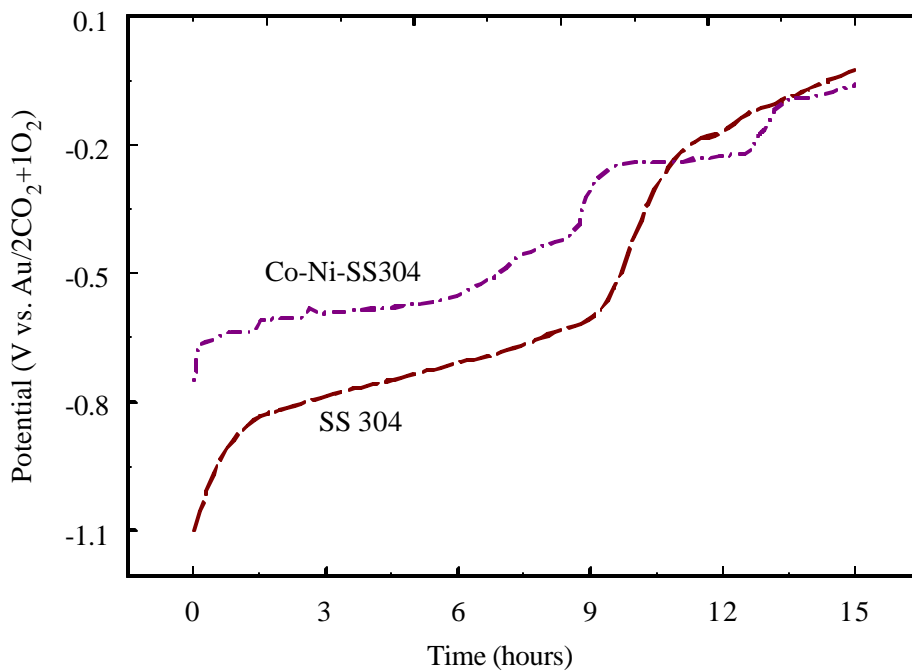
Figure 45. Open circuit potential response of SS304 and Co-Ni-SS304 as a function of exposure time in molten carbonate melt under cathode gas conditions. The potential is referenced to a gold electrode with $2CO_2+1O_2$ as the reference gas.
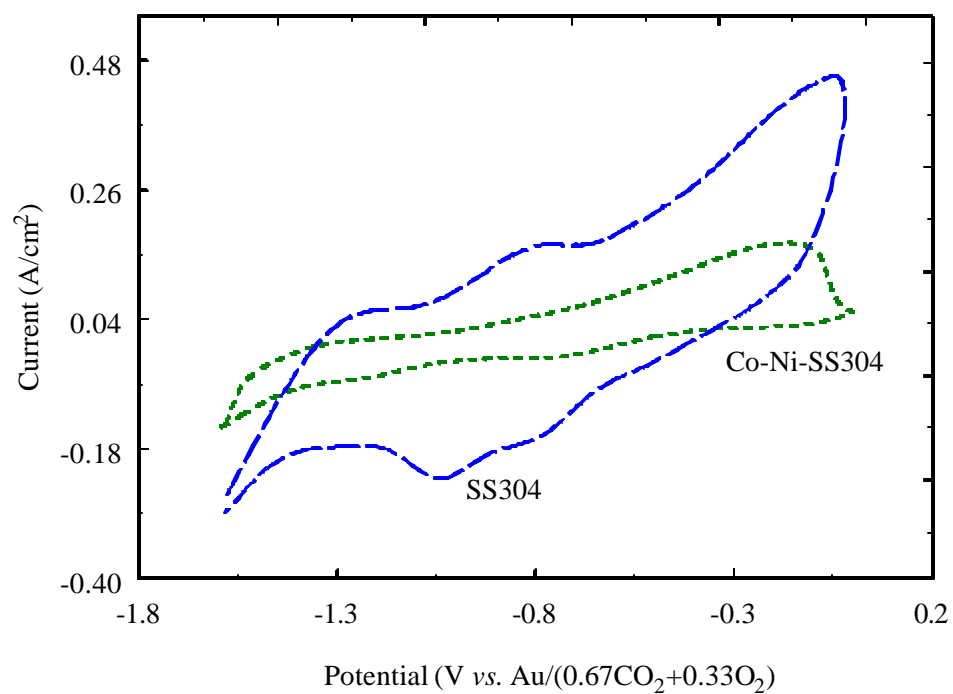
Figure 46. Cyclic voltammograms of SS304 and Co-Ni-SS304 recorded after 2 hours of immersion in molten carbonate at open circuit potential under cathode gas conditions.
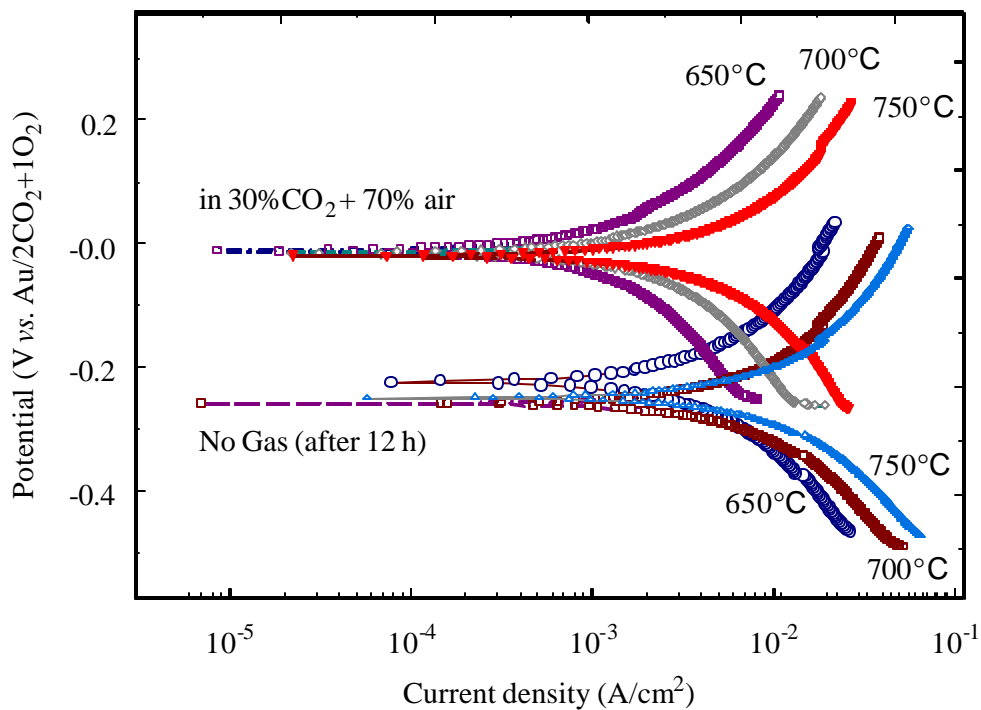
Figure 47. Tafel polarization curves for SS304 obtained as a function of different gas compositions and temperatures. The potential is referenced to a gold electrode with $2CO_2+1O_2$ as the reference gas.

136
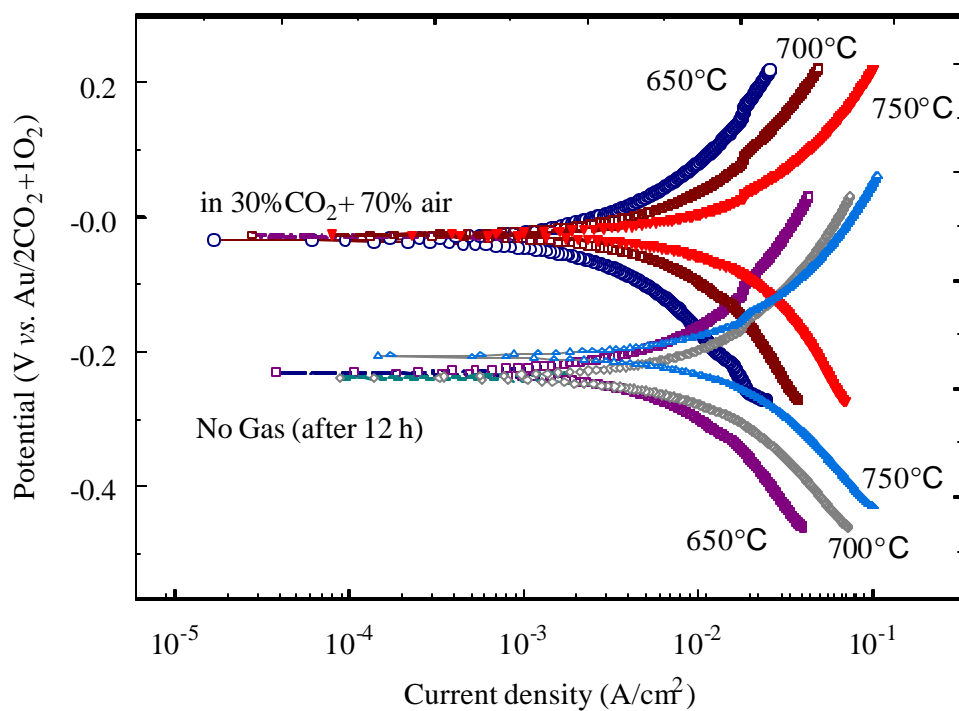
Figure 48. Tafel polarization curves for Co-Ni-SS304 obtained as a function of different gas compositions and temperatures. The potential is referenced to a gold electrode with $2CO_2+1O_2$ as the reference gas.
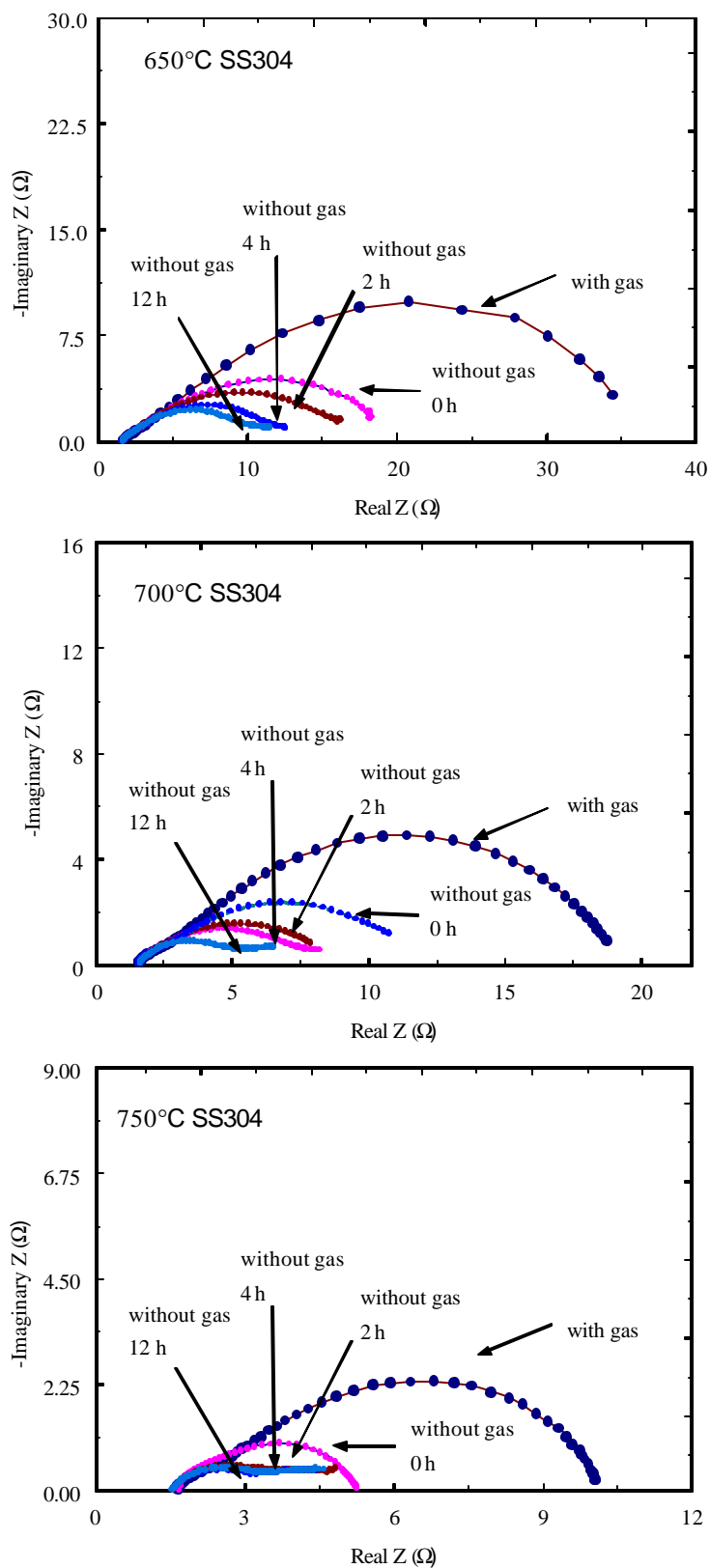
Figure 49. Nyquist plots of impedance response of SS304 obtained as a function of different gas compositions and temperatures.
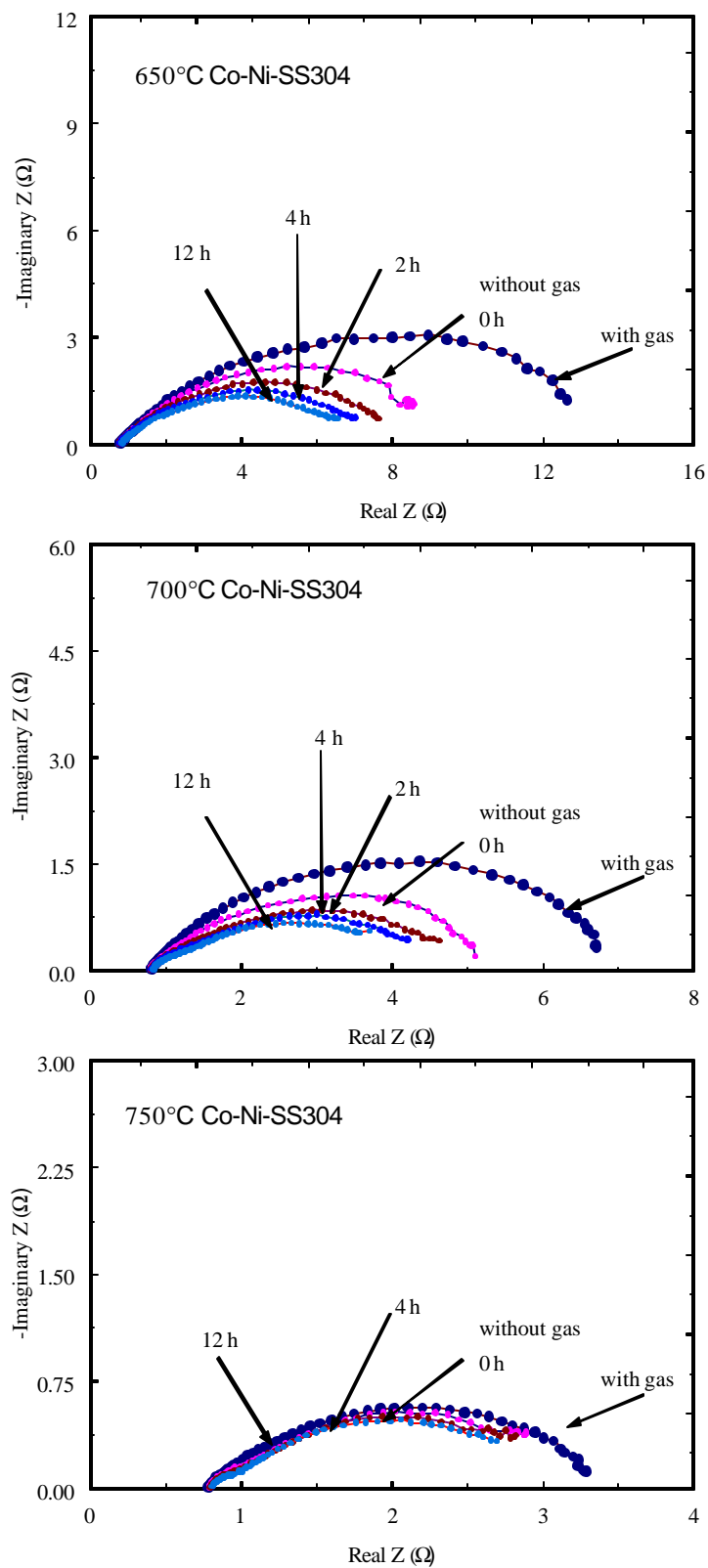
Figure 50. Nyquist plots of impedance response of Co-Ni-SS304 obtained as a function of different gas compositions and temperatures.
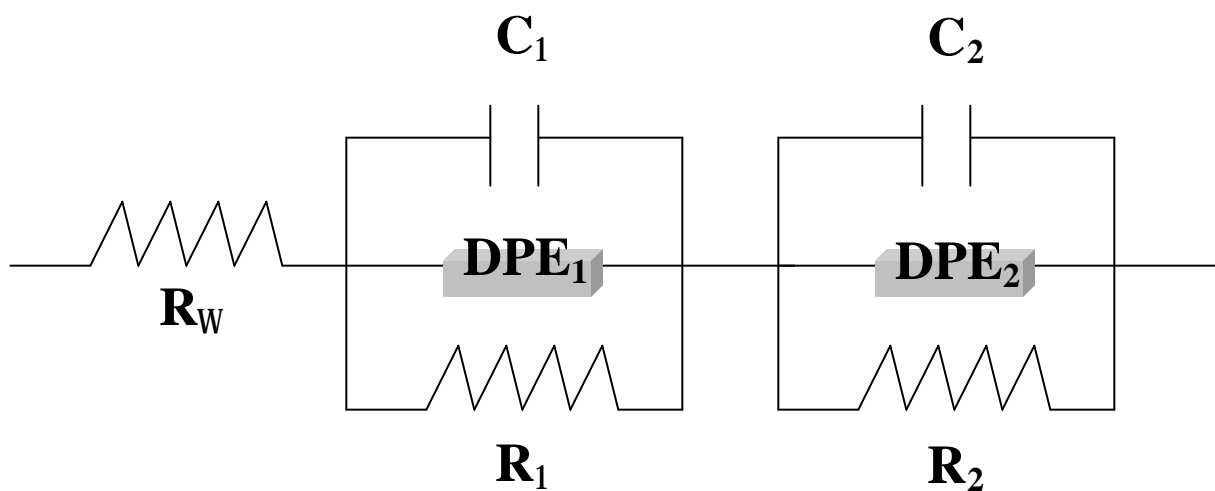
R_Ω – ohmic resistance

R$_1$ – Coating resistance   C$_1$ – Coating capacitance

R$_2$ – Polarization resistance   C$_2$ – Double layer capacitance

DPE$_1$, DPE$_2$ – Distributed Elements, *Zarc-Cole* type

Figure 51.   Schematic of the electrical equivalent circuit that was used to fit the experimental impedance response obtained for the cases of SS304 and Co-Ni-SS304.
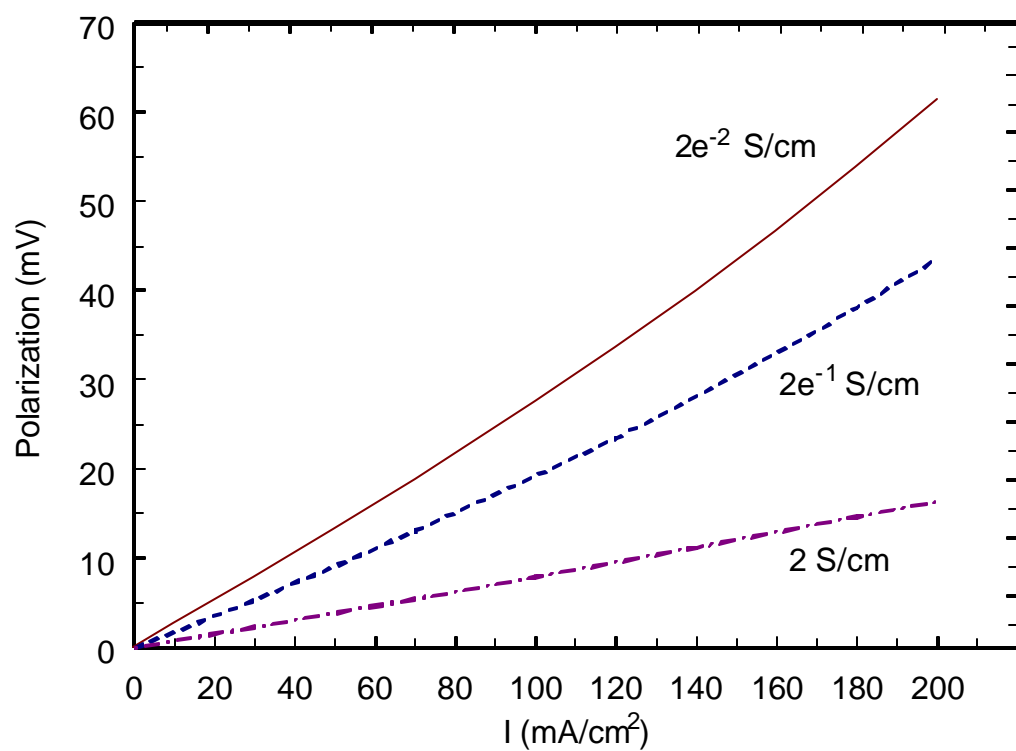
Figure 52. Effect of electrolyte conductivity on the polarization behavior of MCFC cathode.
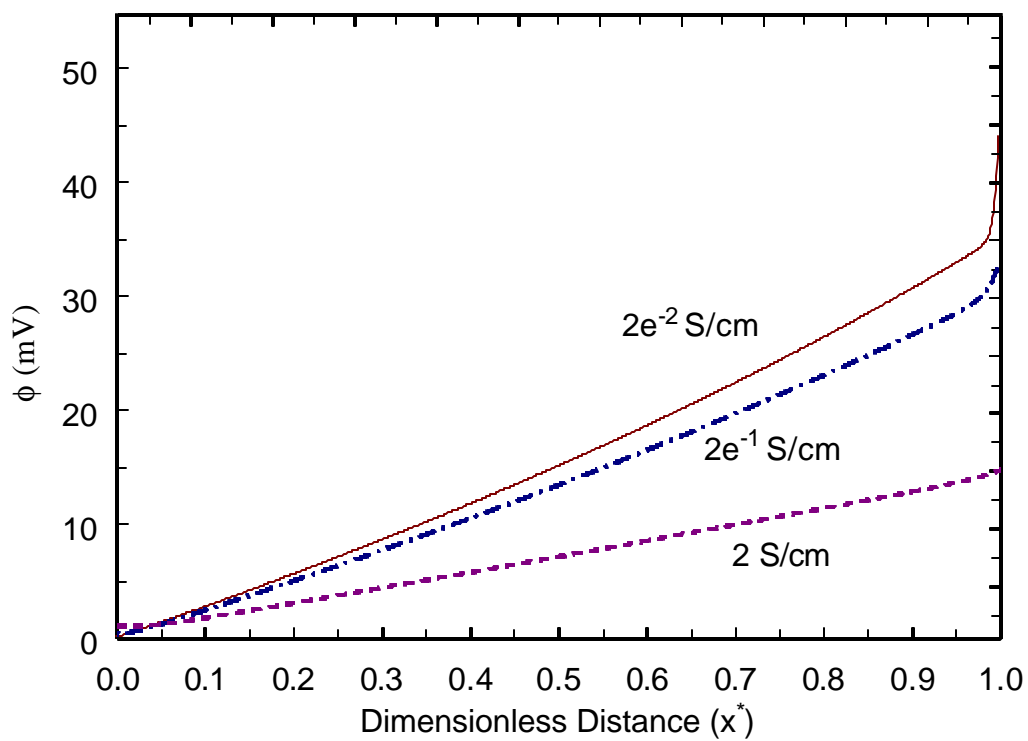
Figure 53. Comparison of overpotential profiles for different κ values. The overpotential is defined as $\langle f \rangle = \langle f \rangle^{(s)} - \langle f \rangle^{(l)}$. Insert shows the profiles closer to the electrolyte tile.
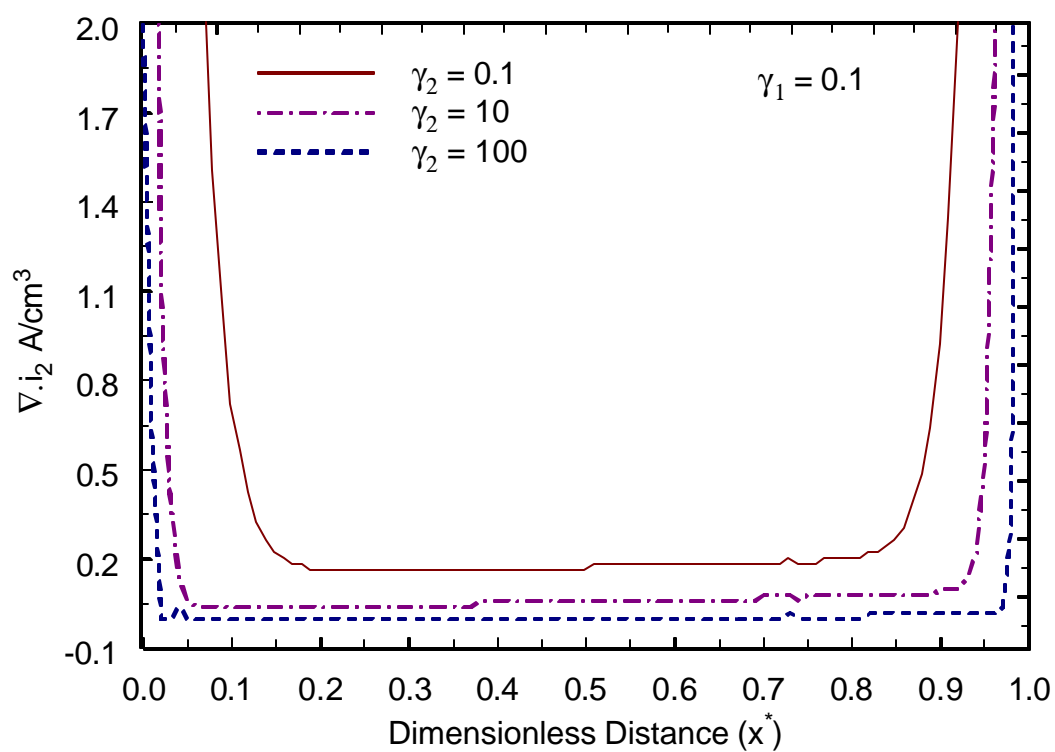
Figure 54. Changes in the electrode reaction rate for varying electrolyte conductivity. The parameters γ_1 and γ_2 are given by Eq. 45 and 46.
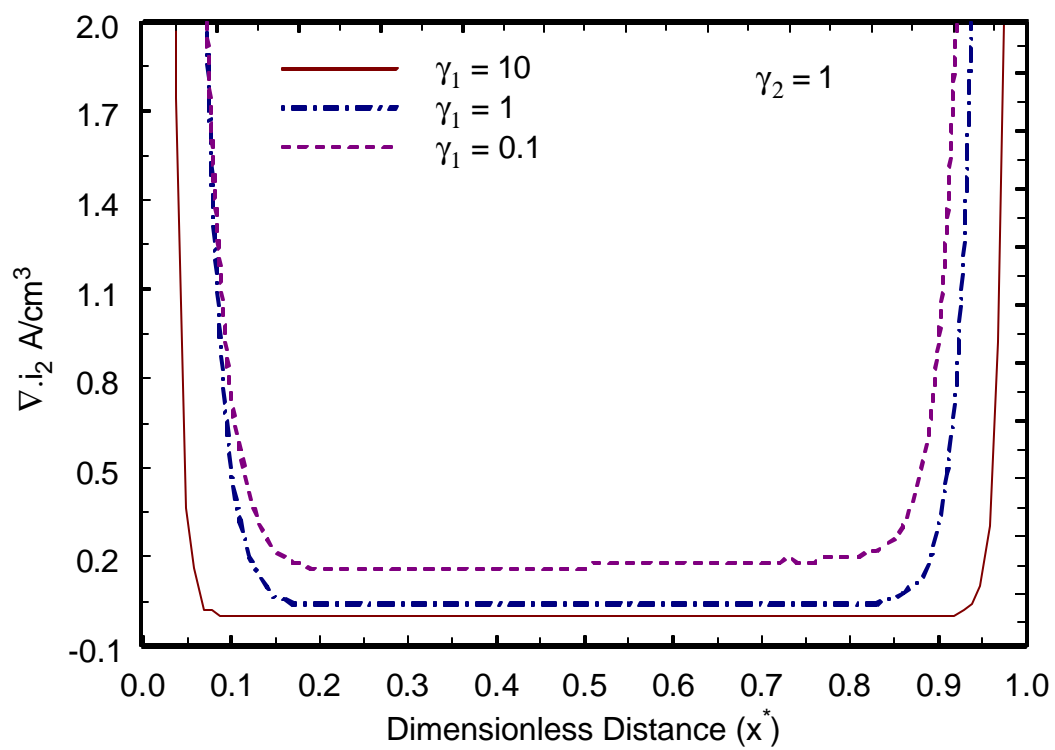
Figure 55. Comparison of the reaction rate for varying electrode conductivity.
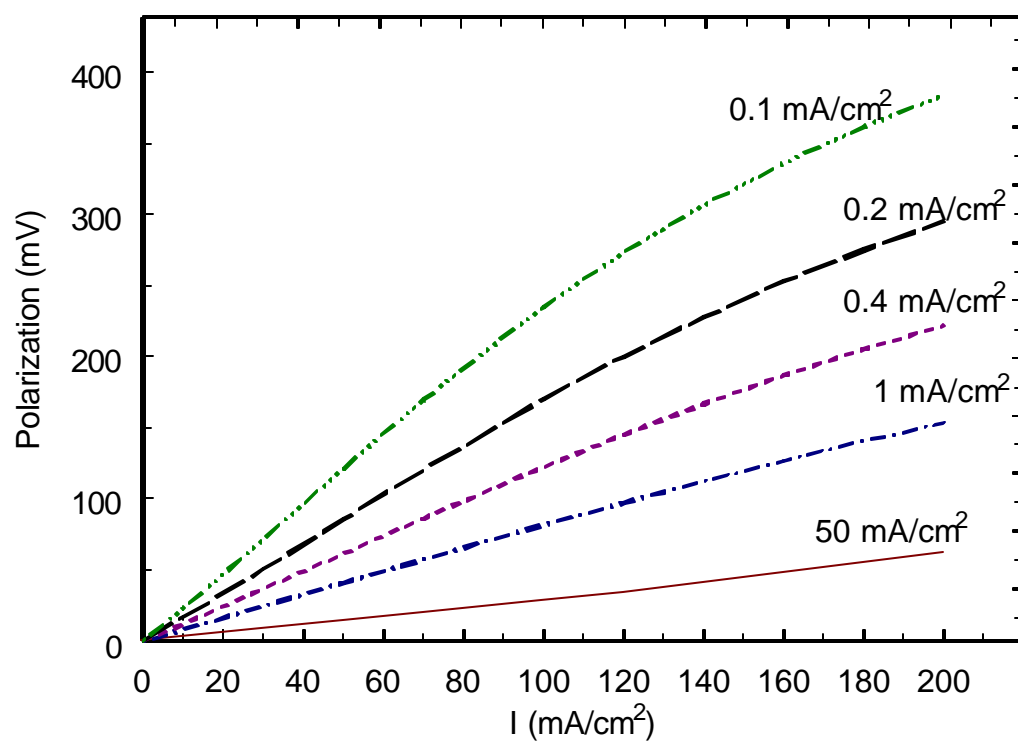
Figure 56. Effect of exchange current density on the polarization behavior of the MCFC cathode.
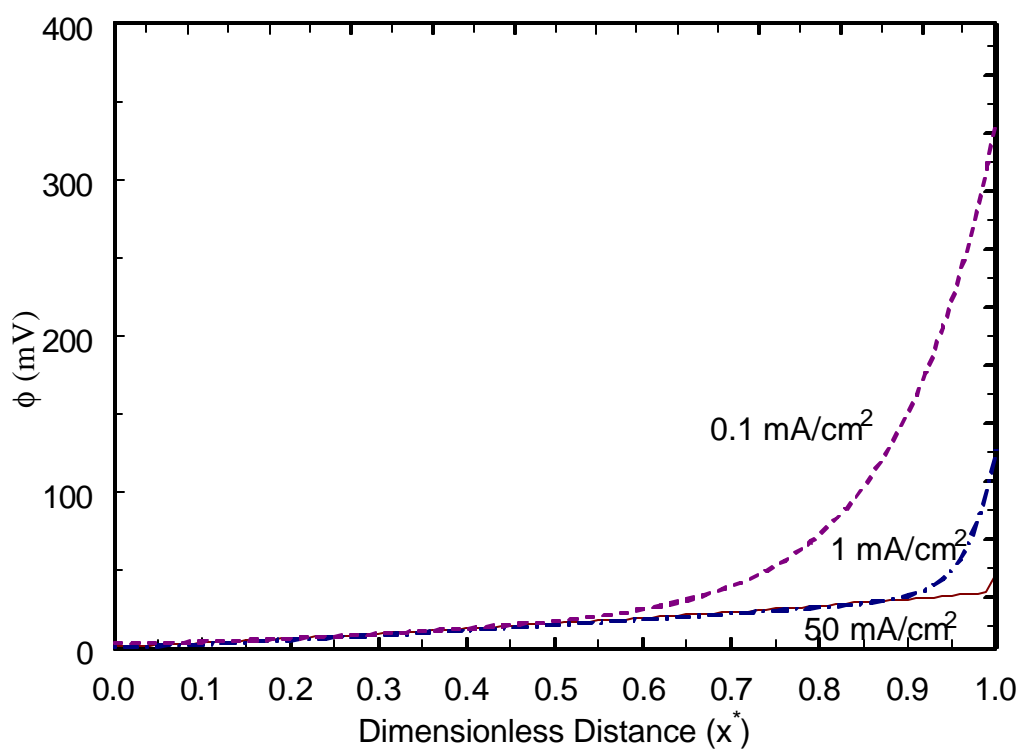
Figure 57. Change in local overpotential along the length of the electrode. Profiles are shown for different values of the exchange current density.
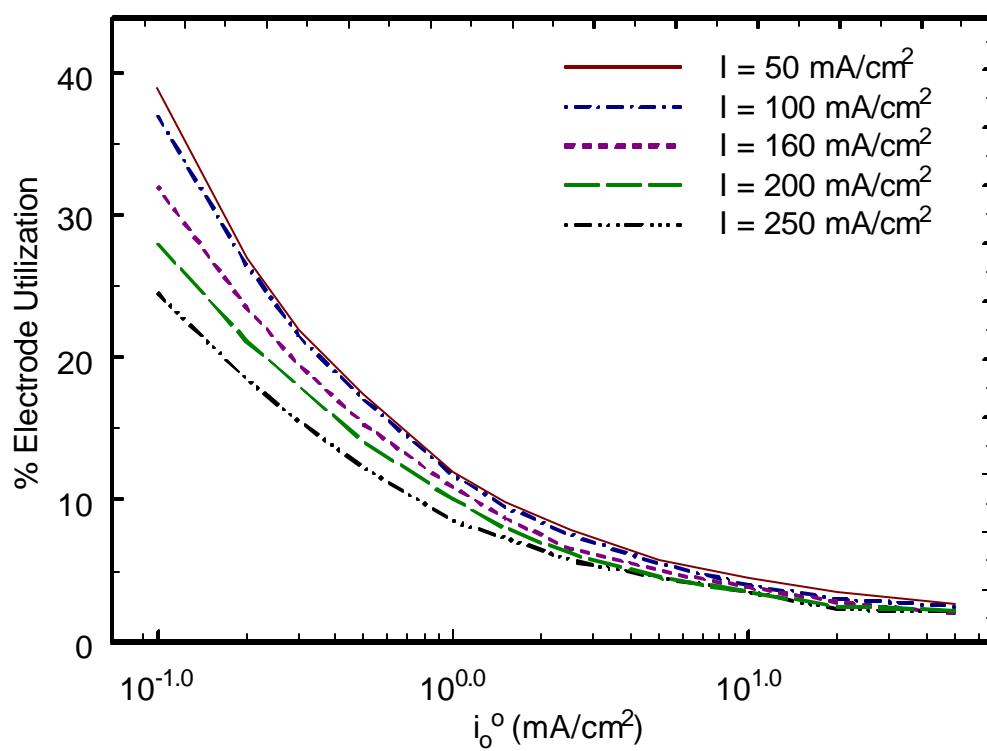
Figure 58. Change in the electrode utilization as a function of exchange current density. Profiles are shown for different applied currents.
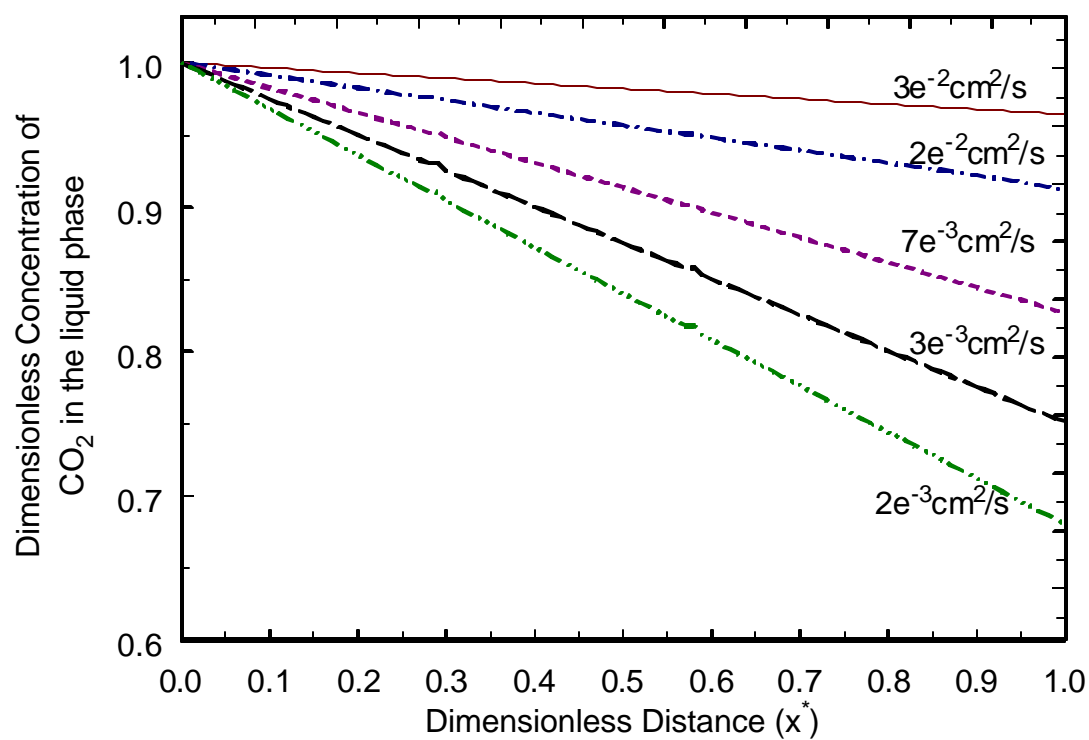
Figure 59. Steady state CO_2 liquid phase concentration profiles across the length of the MCFC cathode for different values of the liquid phase diffusion coefficient.
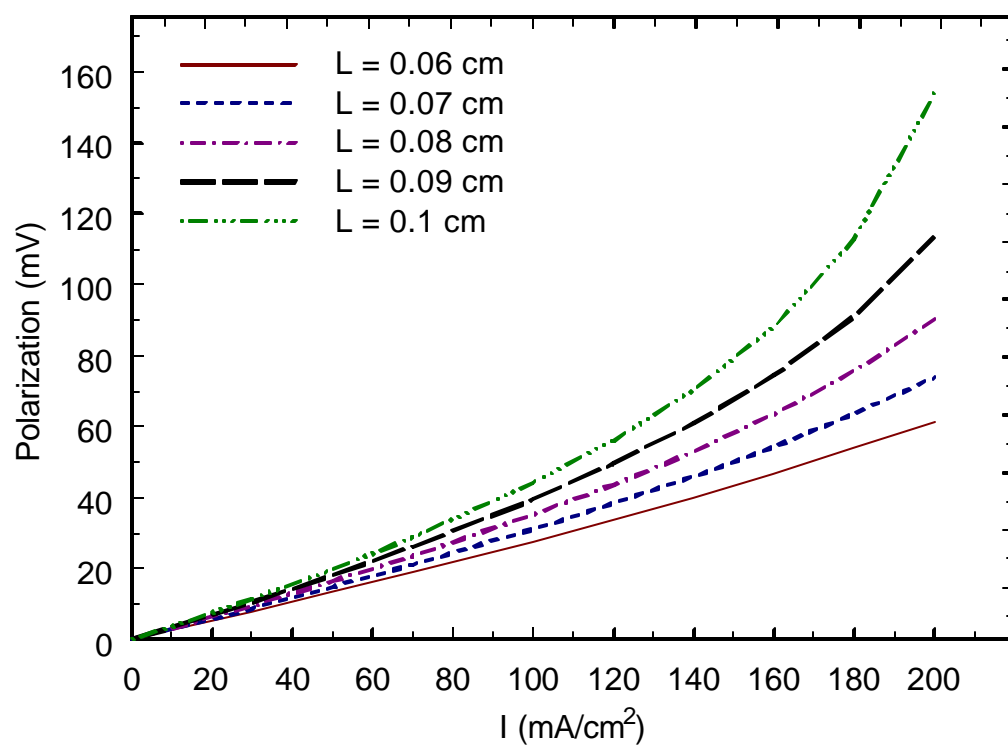
Figure 60. Effect of electrode thickness on the polarization loss at different applied loads.
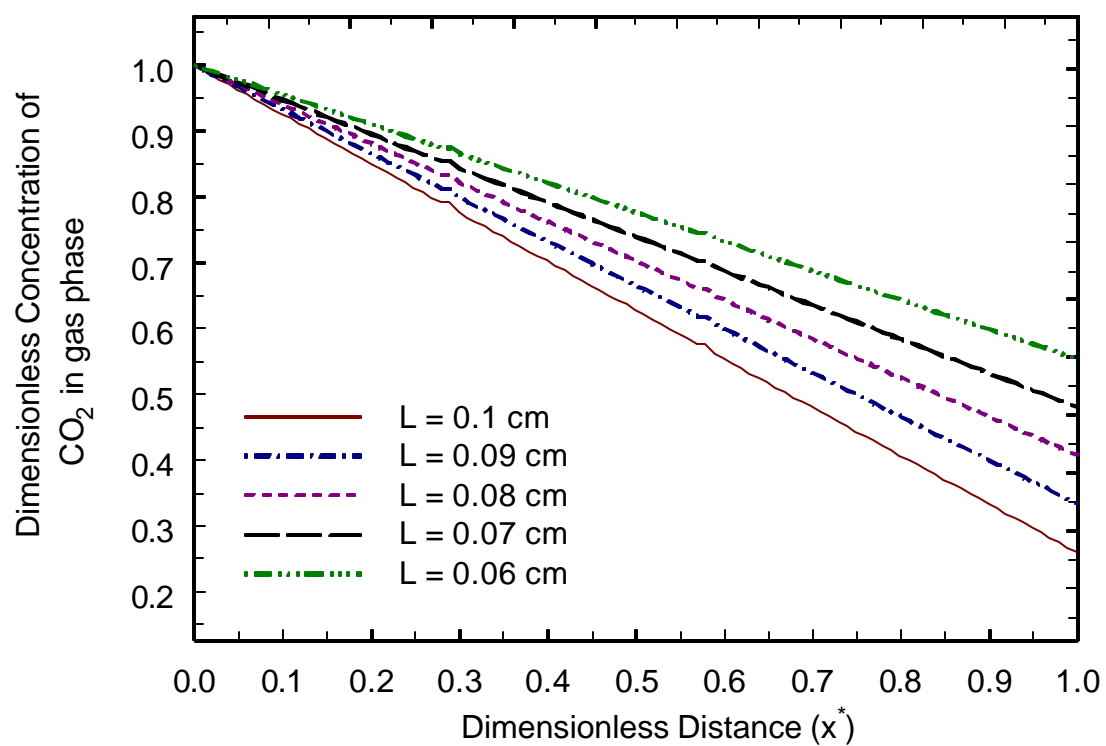
Figure 61. Change in the gas phase CO_2 concentration for varying electrode thickness.
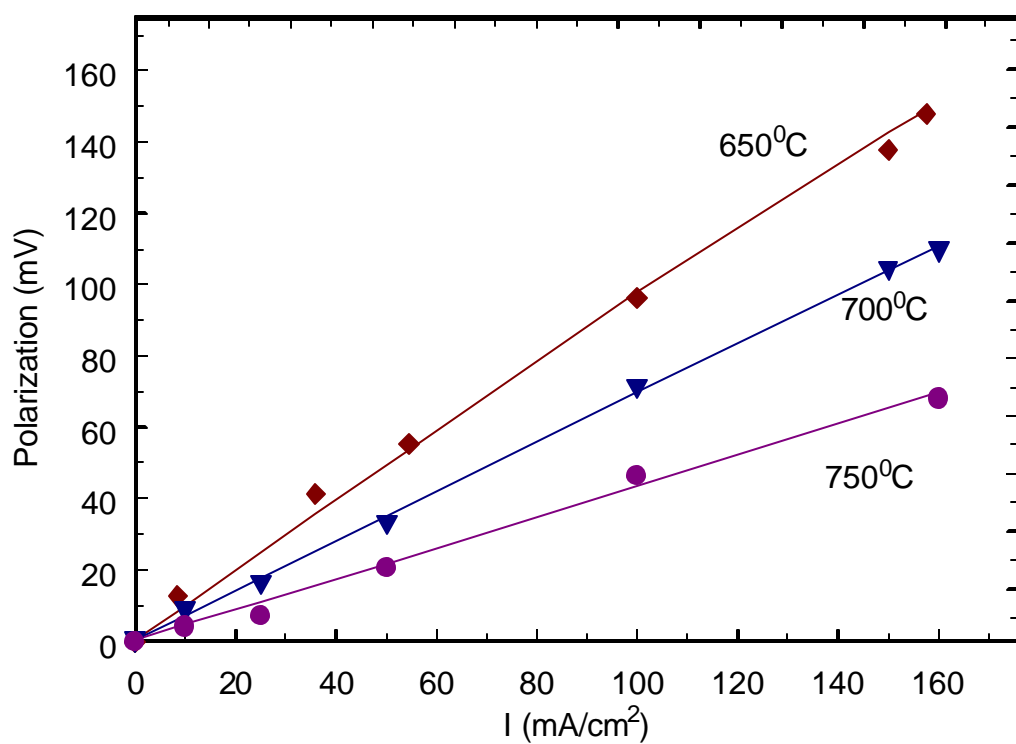
Figure 62. Change in LiNiCoO$_2$ electrode polarization with applied current density for different temperatures. Solid lines are model simulations and symbols represent the experimental data.
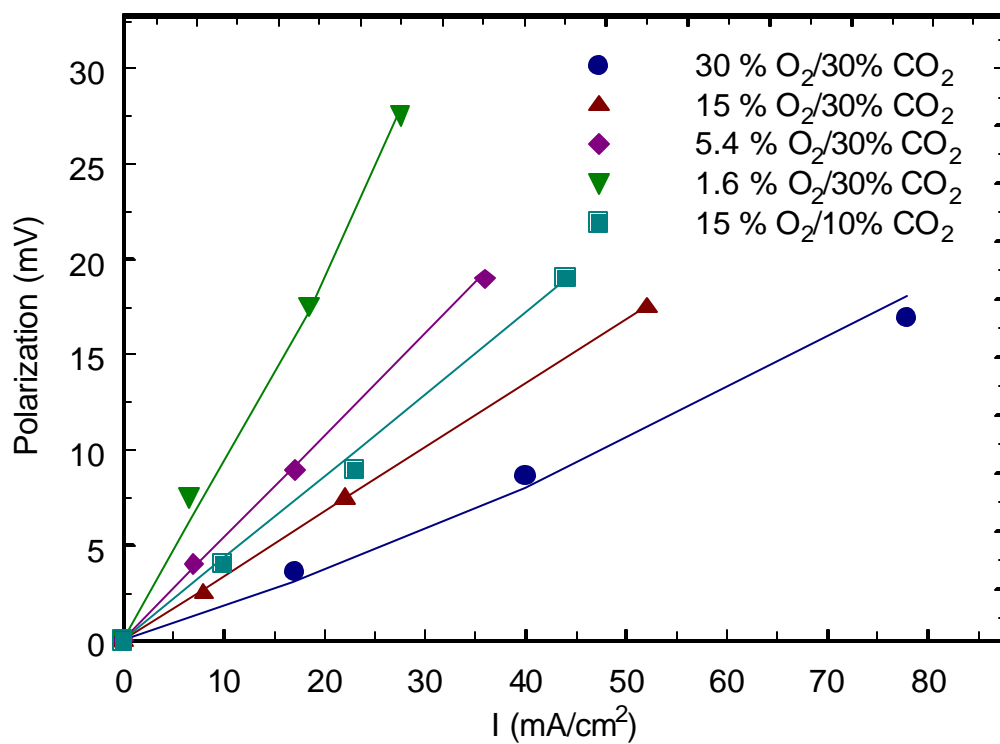
Figure 63. Comparison of model results and experimental data for different gas compositions. Experimental data were obtained from the polarization behavior for $LiCoO_2$ given by Lagergren and Simonsson (62).
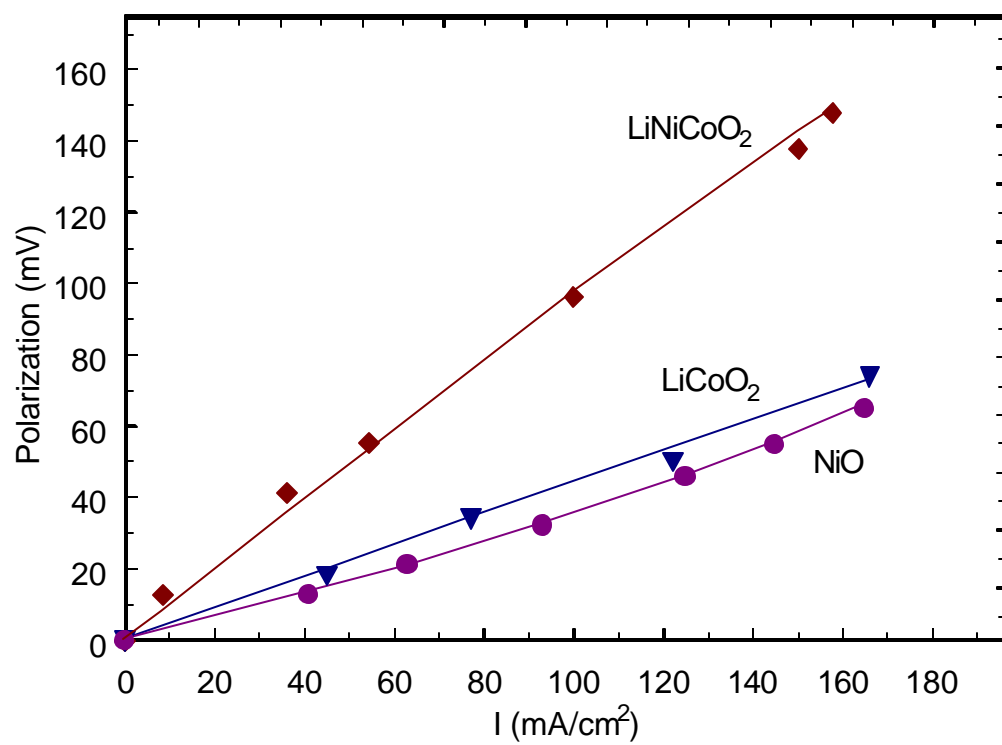
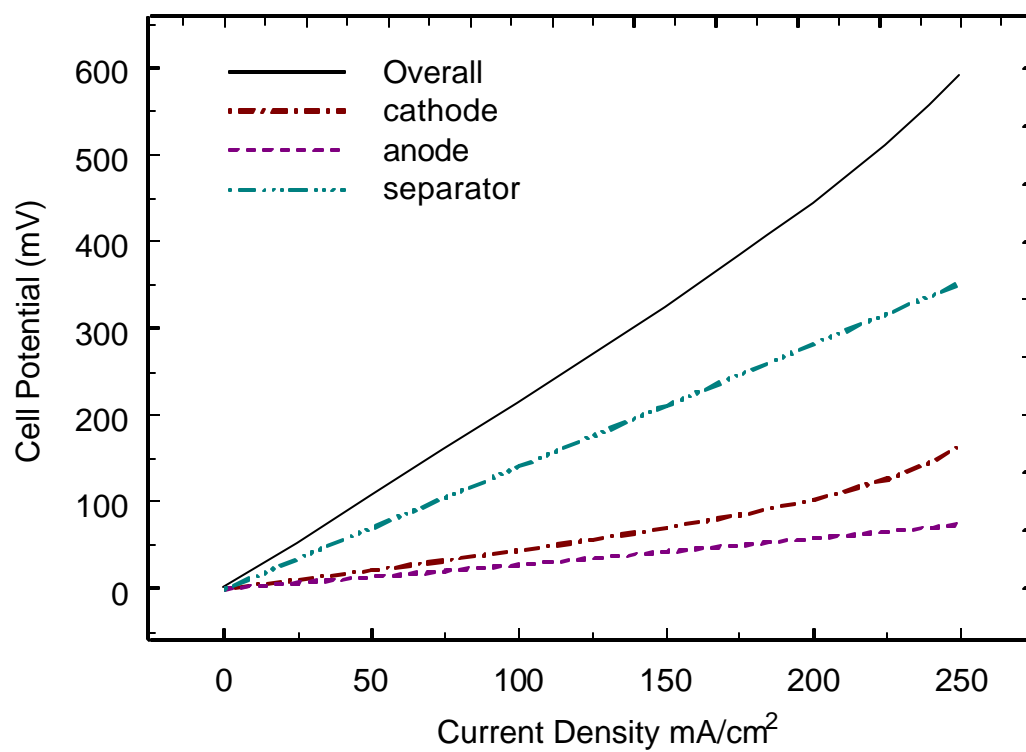**Figure 64.** Comparison of model to experimental polarization data for different cathode materials.

Figure 65. Comparison of overpotentials in the cathode and anode with the overall overpotential.
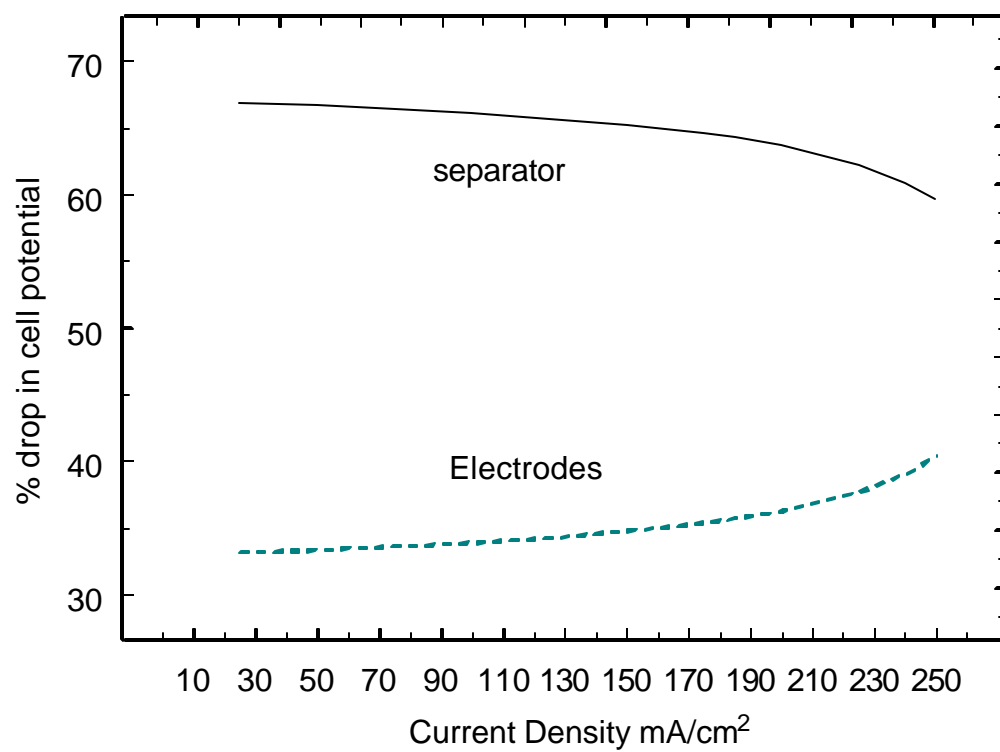
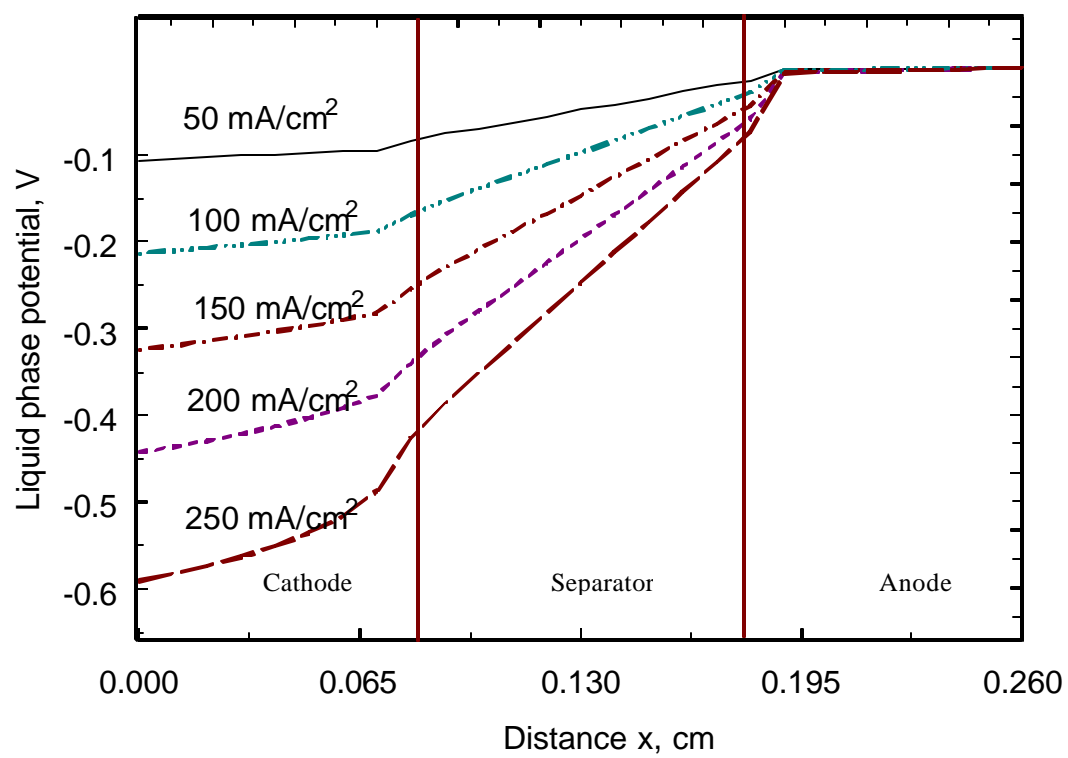**Figure 66.** Percentage drop in the matrix and the electrodes.

Figure 67. Liquid phase potential profiles at different current densities.
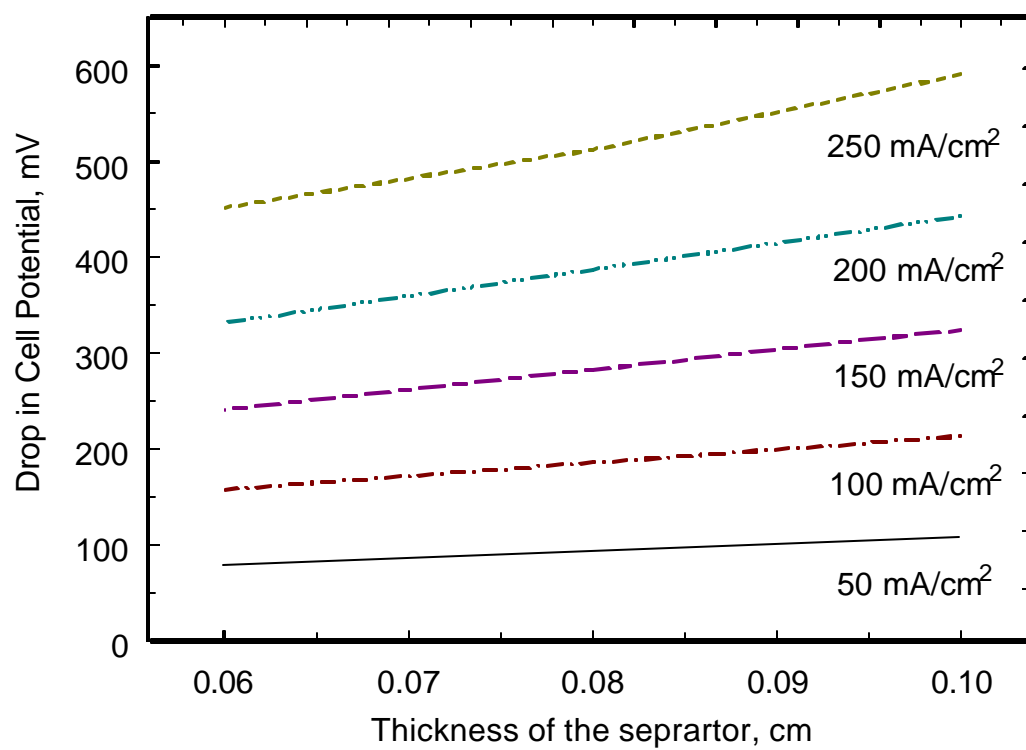
Figure 68. Potential drop as a function of matrix thickness for different current densities.
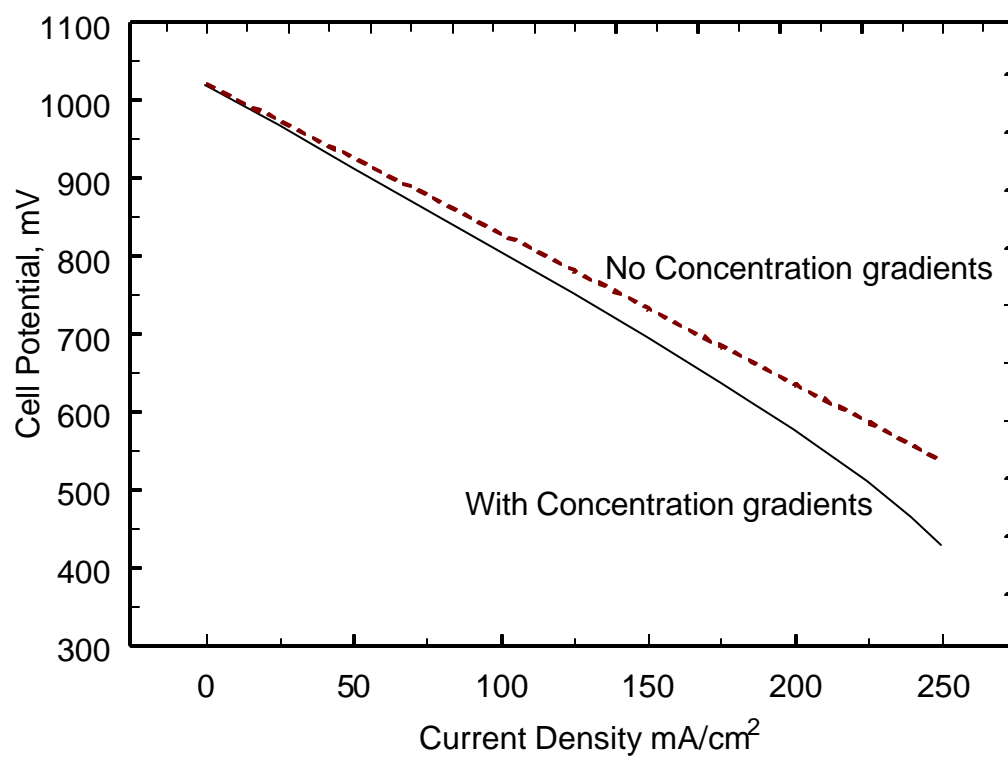
Figure 69. Comparison of the cell potentials obtained using the two models (with and without concentration gradients).

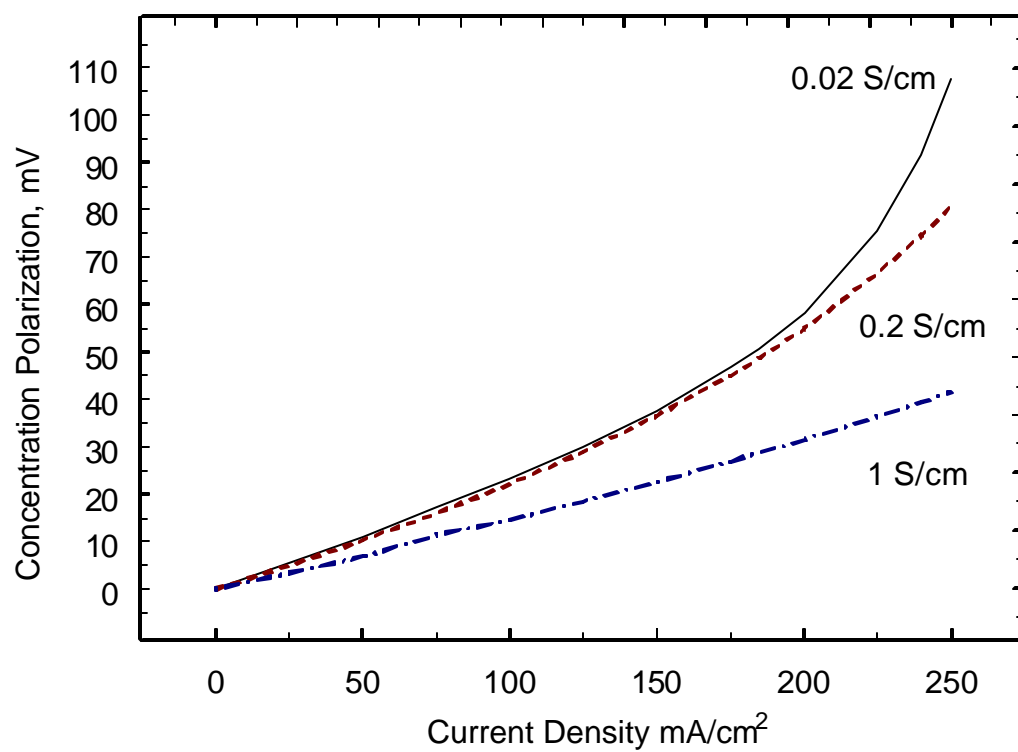**Figure 70.** Concentration Polarization for different ionic conductivities.
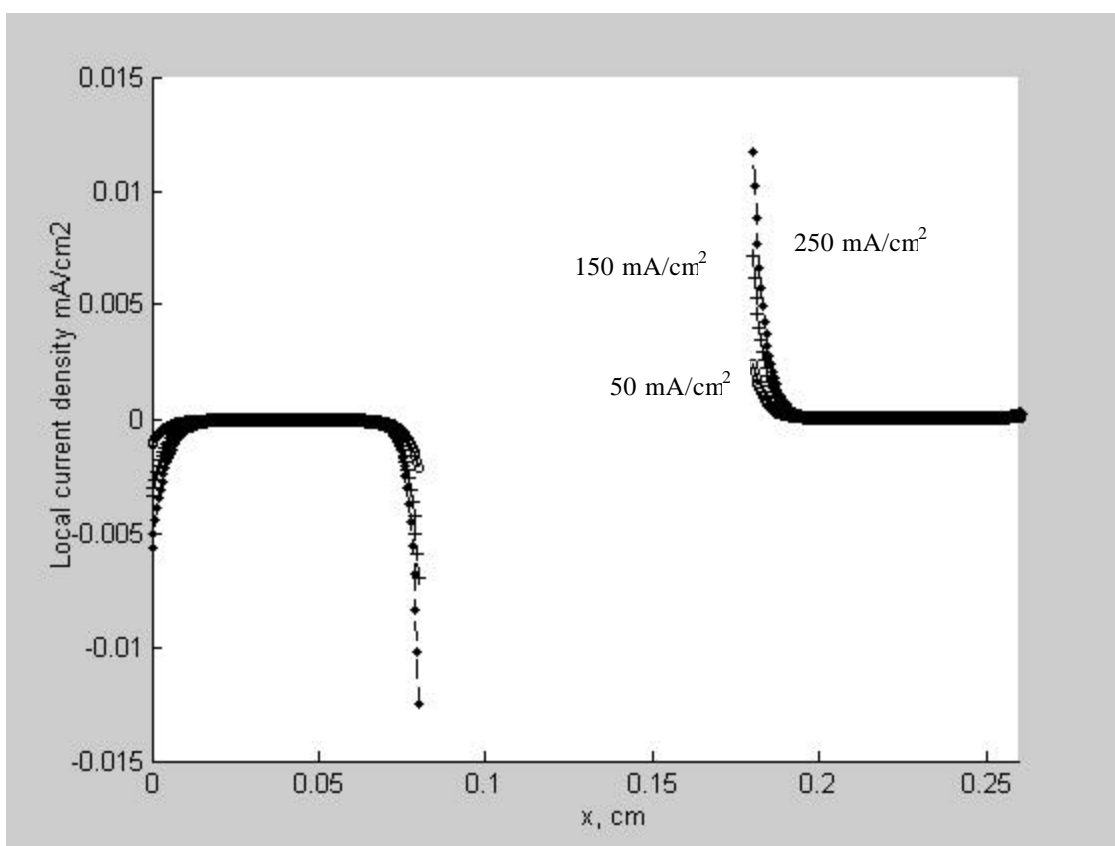
Figure 71. Local current density in the cathode and the anode for different applied current densities. Dashed lines with '+' markers represent 50 mA/cm^2; Dashed lines with no markers represent 150 mA/cm^2; Dashed lines with 'O' markers represent 250 mA/cm^2.
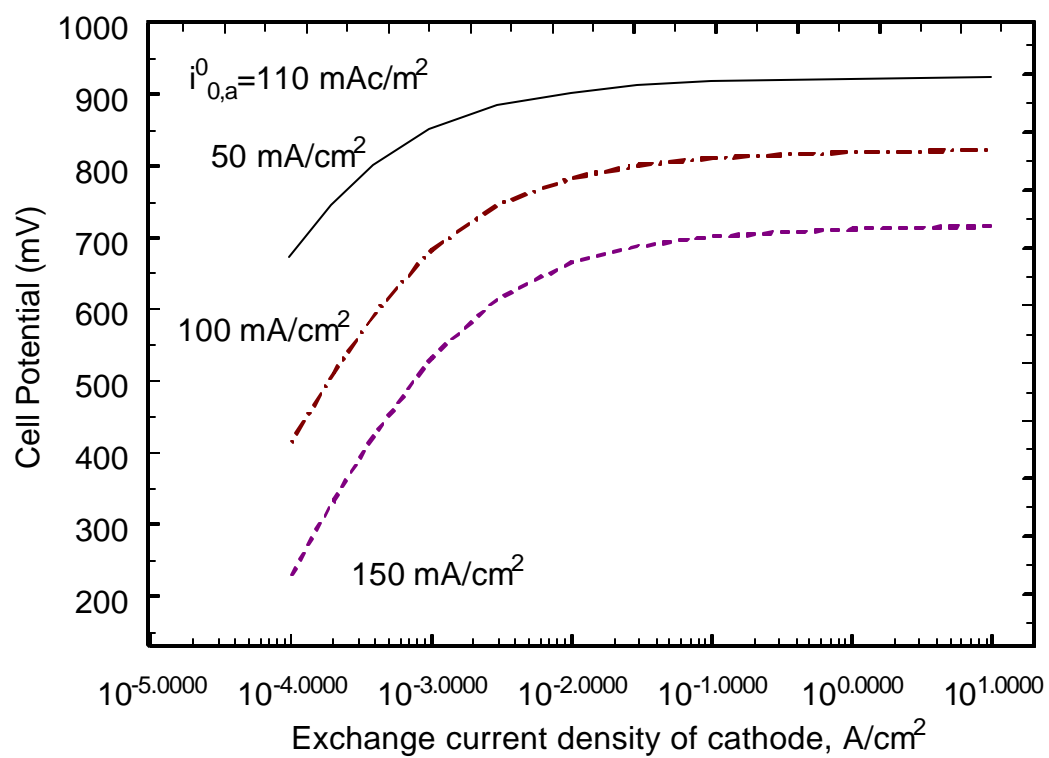
Figure 72. Cell Potential as a function of the cathodic exchange current density.

Figure 73. Cell Potential as a function of the anodic exchange current density.

Figure 74. Effect of cathode conductivity on cell potential.

Figure 75. Effect of electrolyte conductivity on cell potential.

Figure 76. Comparison of model to experimental data of Soler *et al.*[65]
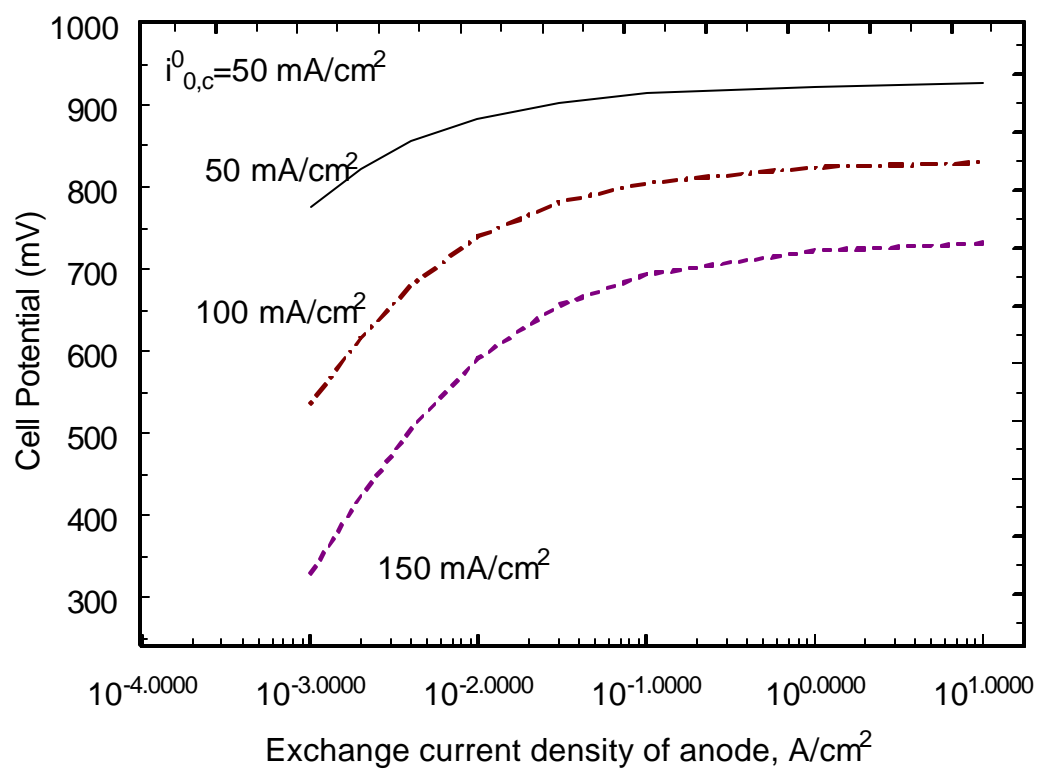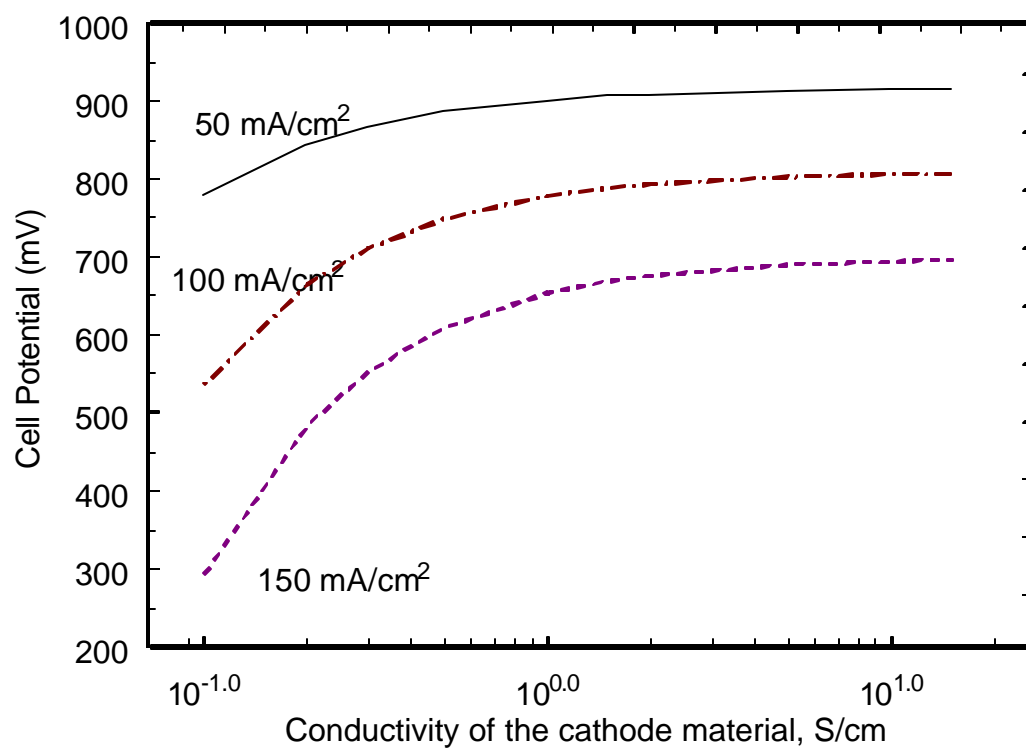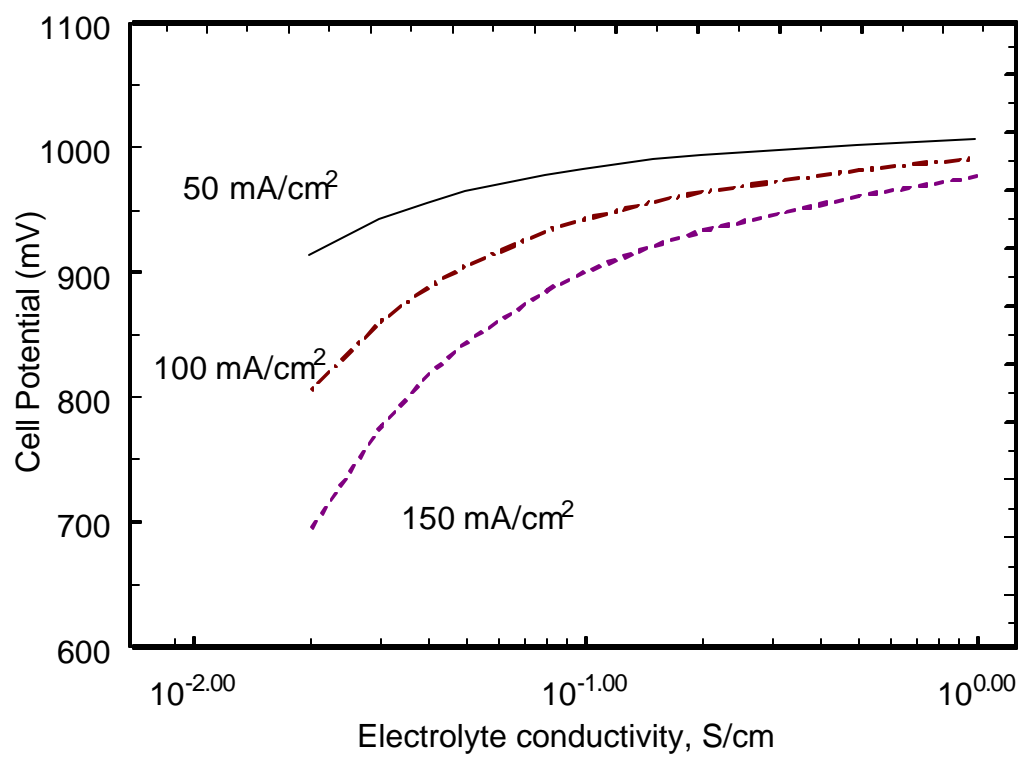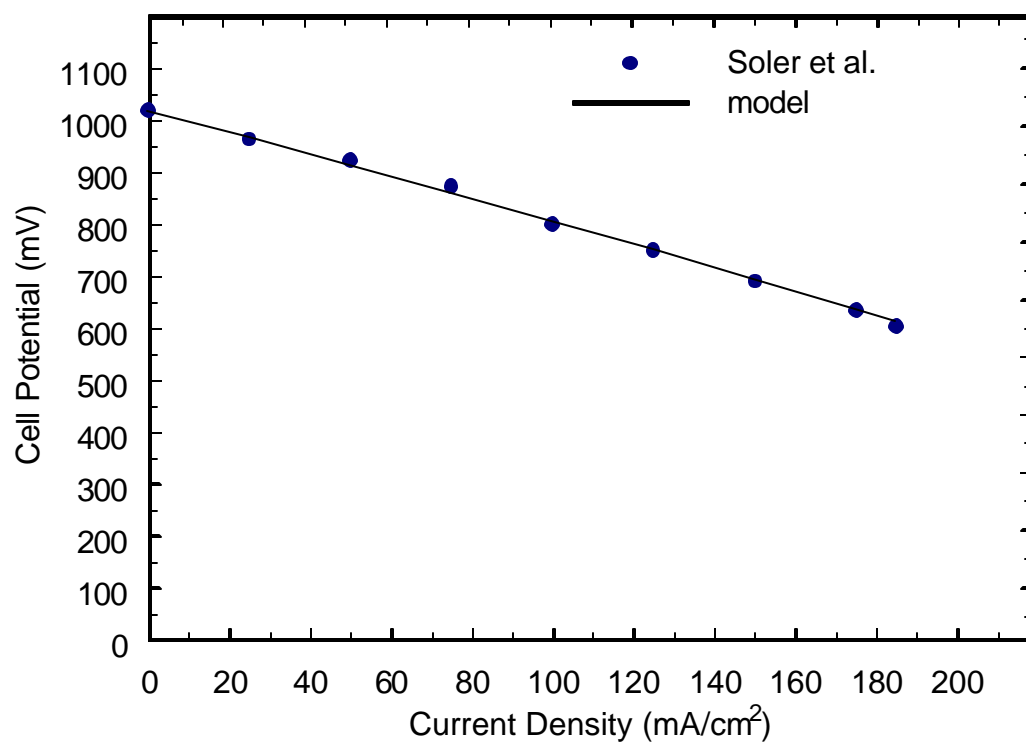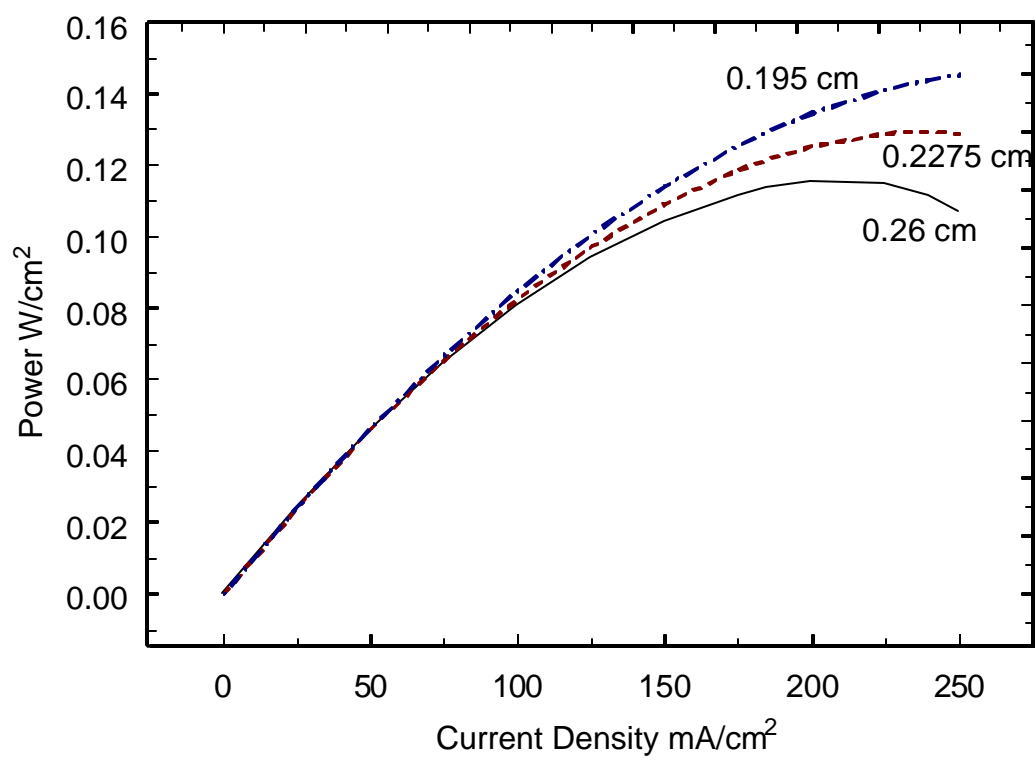
Figure 77. Power density vs. current density for varying cell thickness.

Table I. List of parameters used in cathode model simulations.

Parameter	Value	Reference
Diffusion coefficient of CO_2 in the liquid phase, $D_{CO_2}^{(l)}$	$1e^{-3}$ cm^2/s	**34**
Diffusion coefficient of O_2 in the liquid phase, $D_{O_2}^{(l)}$	$3e^{-3}$ cm^2/s	**34**
Diffusion coefficient of CO_2 in the gas phase, $D_{CO_2}^{(g)}$	1.16 cm^2/s	**46**
Diffusion coefficient of O_2 in the gas phase, $D_{O_2}^{(g)}$	1.16 cm^2/s	**46**
Electrode conductivity, s	13 S/cm	**35**
Electrolyte conductivity, k	$2.0e^{-2}$ S/cm	**34**
Correction for diffusion coefficient, b	1.5	**39**
Correction for conductivity, d	1.5	**39**
Rate constant of the molar flux of CO_2 between the liquid and gas phase, $k_{CO_2}^{(lg)}$	$3e^{-3}$ cm/s	**39**
Rate constant of the molar flux of O_2 between the liquid and gas phase, $k_{O_2}^{(lg)}$	$2e^{-3}$ cm/s	**39**
Thickness of the electrode, L	0.06 cm	**Measured**
Liquid porosity, $e^{(l)}$	0.3	**Measured**
Gas porosity, $e^{(g)}$	0.4	**Measured**
Solid porosity, $e^{(s)}$	0.3	**Measured**
Exchange current density, i_0^0	50 mA/cm^2	**67**
Cathodic transfer coefficient, a_c	0.5	**29,45**
Cathodic transfer coefficient, a_a	1.5	**29,45**
Reaction order based on CO_2, r_1	-1.25	**29,45**
Reaction order based on O_2, r_2	0.375	**29,45**

Table II. Temperature dependence of different electrode parameters for LiNiCoO₂ cathode.

Parameter	a	b (1/K)	R^2
κ	3.268 S/cm	4715.5	0.9915
$D^l_{CO_2}$	144.82 cm^2/s	10975	0.9994
$D^l_{O_2}$	0.352 cm^2/s	4417	0.9751
i^0_0	243.96 A/cm^2	11887	0.9842

Table III. Kinetic and conductivity properties for different cathode materials.

Cathode material	s (S/cm)	i_o (mA/cm^2)
NiO	13	50
LiCoO$_2$	1	5
LiNiCoO$_2$	5	0.65

Table IV. List of parameters used in full cell model simulations.

Parameter	Value	Reference
Diffusion coefficient of CO_2 in the liquid phase in cathode, $D_{CO_2,c}^{(l)}$	$1e^{-3}$ cm^2/s	**34**
Diffusion coefficient of O_2 in the liquid phase in cathode, $D_{O_2,c}^{(l)}$	$3e^{-3}$ cm^2/s	**34**
Diffusion coefficient of CO_2 in the liquid phase in anode, $D_{CO_2,a}^{(l)}$	$1e^{-3}$ cm^2/s	
Diffusion coefficient of H_2 in the liquid phase in anode, $D_{H_2,a}^{(l)}$	$1e^{-3}$ cm^2/s	
Diffusion coefficient of CO_2 in the gas phase in cathode, $D_{CO_2}^{(g)}$	1.16 cm^2/s	**46**
Diffusion coefficient of O_2 in the gas phase in cathode, $D_{O_2}^{(g)}$	1.16 cm^2/s	**46**
Diffusion coefficient of CO_2 in the gas phase in anode, $D_{CO_2}^{(g)}$	4.625 cm^2/s	**46**
Diffusion coefficient of O_2 in the gas phase in anode, $D_{H_2}^{(g)}$	4.625 cm^2/s	**46**
Cathode conductivity, $\boldsymbol{s}_c$	13 S/cm	**35**
Anode conductivity, $\boldsymbol{s}_a$	13 S/cm	
Electrode conductivity, $\boldsymbol{k}$	$2.0e^{-2}$ S/cm	**34**
Correction for diffusion coefficient, b	1.5	**39**
Correction for conductivity, d	1.5	**39**
Rate constant of the molar flux of CO_2 between the liquid and gas phase in the cathode, $k_{CO_2,c}^{(lg)}$	$3e^{-3}$ cm/s	**39**
Rate constant of the molar flux of O_2 between the liquid and gas phase in the cathode, $k_{O_2,c}^{(lg)}$	$2e^{-3}$ cm/s	**39**
Rate constant of the molar flux of CO_2 between the liquid and gas phase in the anode, $k_{CO_2,c}^{(lg)}$	$3e^{-3}$ cm/s	**39**
Rate constant of the molar flux of H_2 between the liquid and gas phase in the anode, $k_{H_2,a}^{(lg)}$	$2e^{-3}$ cm/s	**39**
Thickness of the fuel cell, L	0.23 cm	**Measured**
Thickness of the cathode, x_l	0.08 cm	**Measured**

Thickness of the matrix, $x_2 - x_1$	0.1 cm	**Measured**
Thickness of the anode, $L - x_2$	0.08 cm	**Measured**
Liquid porosity in the cathode, $e_c^{(l)}$	0.3	**Measured**
Gas porosity in the cathode, $e_c^{(g)}$	0.4	**Measured**
Solid porosity in the cathode, $e_c^{(s)}$	0.3	**Measured**
Liquid porosity in the anode, $e_a^{(l)}$	0.2	**Measured**
Gas porosity in the anode, $e_a^{(g)}$	0.45	**Measured**
Solid porosity in the anode, $e_a^{(s)}$	0.35	**Measured**
Cathodic transfer coefficient, $a_{c,c}$	0.5	**45**
Anodic transfer coefficient, $a_{a,c}$	1.5	**45**
Cathodic transfer coefficient, $a_{c,a}$	1.5	**28**
Anodic transfer coefficient, $a_{a,a}$	0.5	**28**
Reaction order based on CO_2 in the cathode, $r_{1,c}$	-1.25	**45**
Reaction order based on O_2 in the cathode, $r_{2,c}$	0.375	**45**
Reaction order based on CO_2 in the anode, $r_{1,a}$	0.25	**28**
Reaction order based on H_2 in the anode, $r_{2,a}$	0.25	**28**
Equilibrium potential of the cathodic reaction $E_{eq,c}$, V	0	**Measured**
Equilibrium potential of the anodic reaction $E_{eq,a}$, V	-1.02	**Measured**